# LEADING POINTS CONCEPTS IN TURBULENT PREMIXED COMBUSTION MODELING

A Dissertation
Presented to
The Academic Faculty

by

Alberto Amato

In Partial Fulfillment
of the Requirements for the Degree
Doctor of Philosophy in the
School of Mechanical Engineering

Georgia Institute of Technology
August 2014

# LEADING POINTS CONCEPTS IN TURBULENT PREMIXED COMBUSTION MODELING

Approved by:


Dr. Tim Lieuwen, Advisor
School of Aerospace Engineering
*Georgia Institute of Technology*

Dr. Yuri Bakhtin
School of Mathematics
*Georgia Institute of Technology*

Dr. Jerry Seitzman
School of Aerospace Engineering
*Georgia Institute of Technology*

Dr. P. K. Yeung
School of Aerospace Engineering
*Georgia Institute of Technology*

Dr. Caroline Genzale
School of Mechanical Engineering
*Georgia Institute of Technology*



Date Approved: May 8, 2014

*To my parents Carlo and Teresa*

# ACKNOWLEDGEMENTS

"[The discovery of the Higgs boson] *certainly shows to us the value of just imagining… and try to follow the leads that you get from simple ideas… that is worthwhile doing this and see where you come out.*"
Gerald Guralnik, co-discoverer of the Higgs boson
July 4, 2012, www.youtube.com/cerntv

This thesis would be incomplete without mentioning several people who assisted, supported and encouraged me during the course of my study. First and foremost, I would like to thank my advisor, Prof. Tim Lieuwen, for his guidance and continuous support during the long and challenging years spent at Georgia Tech. I am neither the first nor I will be the last person to acknowledge Tim's leadership: he truly has inspired our group to be better thinkers and persons. In a similar vein, I would like to thank Prof. Jerry Seitzman for many insightful comments on my work. His lucid mind and scientific curiosity are infectious and constantly challenge us students to be and do our best. I am also profoundly indebted to Dr. Marcus Day for providing me with many of the data utilized in this thesis and for patiently explaining the many subtleties involved in their analysis. Likewise, I am very appreciative of all the assistance that Prof. Yuri Bakhtin provided to help me understand many mathematical details of this thesis. I would also like to express my gratitude to my committee members, Prof. Caroline Genzale and Prof. P.K. Yeung, for agreeing to serve on my committee in spite of their extremely busy schedules, and for offering constructive and valuable critiques regarding my research work.

The Ben T. Zinn Combustion Laboratory provided me with the perferct home during all the years of my doctorate. Andrew Marshall and Prabhakar Venkateswaran, with the late

addition of Julia Lundrigan, were my companions in this research project. I shared with them many highs and lows, so frequent in turbulent combustion research, and this work would not have been possible without their help. I am very grateful to Vishal Acharya, Dong-Hyuk Shin, Shreekrishna and Jack Crawford for helping me understand many aspects of combustion theory and numerical computations. I will always cherish the memory of the time spend shoulder to shoulder in our office with also Jordan Blimbaum. Our "legacy" is in good hands with Nick Magina and Luke Humprey. The "experimentalists" (in no particular order) Jacqueline O'Connor ("Lab-mom"), Chris Foley, Ben Emerson, Ben Wilde, Bobby Noble, Brandon Sforzo, Ianko Chterev, Mike Aguilar, Michael Malanoski, Ryan Sullivan, Sai Kumar, Yash Kochar, Benjamin Knox and Gina Magnotti, were always kind to me and a true source of inspiration.

Here I would also like to acknowledge the many "slivers" of Italy that I befriended in Atlanta and helped me miss less my home. In August 2008 I arrived in the United States with Daniele Bertolotti and Paolo Manenti; for the first few months, before they moved back to Italy, they were my roomates and travelmates, without them I would have not enjoyed as much this experience. Matteo Senesi and Luca Airoldi shared with me the choice of staying longer in the US to pursue a PhD. Our summer trip to Savannah with Alice Sacchetti and Andrea Trimarco will always remain one of my funniest memories. Martina Baroncelli shared with me one year of life at the Combustion Lab. When she arrived at the lab from Florence, I immediately started to appreciate the pleasure of hearing a familiar "buongiorno" in a Tuscan accent first thing in the morning.

Finally, I would like to thank my family for its unfailing support during these years. To my parents Carlo and Teresa goes all my affection. My uncle Roberto with his wife Sara

and their children Antonio and Elisagiulia never failed to cheer me up with their Skype phonecall. My cousins Pierluigi and Silvia with my grandmother Elisabetta, my uncle Guido and aunts Manuela and Giovanna were always the first people that I wanted to see when traveling home for Christmas and have been always a source of strength for me. Unfortunately, my uncle Davide passed away at a very young age while I was in the middle of my graduate studies. He had been enthusiastic and encouraging about my studies since day one. To him goes my deepest graditude.

# TABLE OF CONTENTS

# LIST OF TABLES

# LIST OF FIGURES

# SYMBOLS AND ABBREVIATIONS

**Latin alphabet**

| | |
|---|---|
| $A_T$ , $A_{ref}$ | flame area |
| $A$ | shear flow amplitude |
| $c$ | progress variable |
| $c_p$ | specific heat at constant pressure |
| $D$ | mass diffusion coefficient [$m^2/s$] |
| $Da = \left(l_t/\delta_{T0}\right)/\left(u'/s_{L0}\right)$ | Damköhler number |
| $f$ , $F$ | arbitrary function |
| $g = d\xi/dx$ | spatial gradient of the flame position $\xi$ |
| $G$ | level set function (G-equation) |
| $H$ | Hamiltonian function |
| $K_C = -\nabla\cdot\vec{n}$ | mean curvature |
| $K_S = -\vec{n}\vec{n} : \nabla\vec{u} + \nabla\cdot\vec{u}$ $= -\vec{n}\cdot\underline{\underline{S}}\cdot\vec{n} + \nabla\cdot\vec{u}$ | strain rate |
| $Ka = \left(u'/s_{L0}\right)^{3/2}\left(l_t/\delta_{T0}\right)^{-1/2}$ | Karlovitz number (turbulent flows) |
| $Ka = \kappa\delta_{T0}/s_{L0}$ | Karlovitz number (laminar flows) |
| $L$ | length scale |
| $\mathcal{L}$ | Lagrangian function associate with the Hamiltonian $H$ |
| $l_t$ | turbulent integral length scale |
| $\ell$ | Markstein length |
| $Le = \lambda/\left(\rho c_p D\right)$ | Lewis number |
| $Ma = \ell/\delta_{F0}$ $(Ma_c, Ma_d)$ | Markstein number (based on consumption speed $s_{c,P}$, based on displacement speed $s_d$) |
| $\vec{n}, n$ | normal vector, normal direction (pointing toward the products) |
| $p$ | pressure |
| $Re = \left(u'/s_{L0}\right)\left(l_t/\delta_{T0}\right)$ | Reynolds number |
| $r$ | radial position |
| $R$ | radius |
| $\underline{\underline{S}} = \frac{1}{2}\left(\left(\nabla\vec{u}\right)^T + \nabla\vec{u}\right)$ | flow strain tensor |
| $s_c$ | consumption speed (Eq. (2.12)) |
| $s_{c,P}$ | consumption speed (Eq. (2.11)) |
| $s_d$ , $(s_{d,0})$ | displacement speed (unstretched) |
| $s_L$ | flame speed (generic) |

| | |
|---|---|
| $s_{L,max}$ | critically stretched laminar flame speed ( $Ma < 0$ ) |
| $s_{L0}$ | unstretched laminar flame speed |
| $s_T$ | turbulent burning speed / front overall displacement speed |
| $t$ | time |
| $T$ | temperature (Chapter 2 and 3) time period (Chapter 4) |
| $T^{b,0}$ | adiabatic flame temperature |
| $\vec{t}, t$ | tangential vector, tangential directions |
| $\vec{u} = (u_x, u_y, u_z)$ | flow velocity |
| $\vec{v}_F = \vec{u} - s_d \vec{n}$ | total flame velocity |
| $V$ | transverse flow velocity |
| $\vec{x} = (x, y, z)$ | position (Cartesian coordinates) |
| $Y$ | mass fraction |

**Greek alphabet**

| | |
|---|---|
| $\delta_F$ , ( $\delta_{F0}$ ) | flame thickness based on fuel concentration gradient (unstretched) |
| $\delta_T$ , ( $\delta_{T0}$ ) | thermal flame thickness (unstretched) |
| $\delta_{H2}$ , ( $\delta_{H2,0}$ ) | full width at half maximum of $H_2$ consumption rate (unstretched) |
| $\phi$ | equivalence ratio |
| $\varphi$ | generic function |
| $\gamma$ | characteristic curve |
| $\mu$ | weighted mean (Eq. (3.11)) |
| $\lambda$ | thermal conductivity [$W/(m^2K)$] |
| $\rho$ | mass density [$kg/m^3$] |
| $\kappa$ | stretch rate [$1/s$] |
| $\sigma$ | weighted standard deviation (Eq. (3.11)) |
| $\xi$ | flame position |
| $\theta$ | generic angle |
| $\tau$ | time |
| $\dot{\omega}$ | reaction rate [$kg/(m^3 s)$] |

**Subscripts**

| | |
|---|---|
| $F$ | fuel |
| $O$ | oxidizer |
| $ref$ | reference surface |
| $t$ | tangential direction |
| $n$ | normal direction |

**Superscripts**

| | |
|---|---|
| $u$ | unburned gasses |
| $b$ | burned gasses |

**Other symbols**

| | |
|---|---|
| $\overline{(\ )}$ | averaged quantity |
| $(\ )'$ | fluctuating quantity |
| $\widetilde{(\ )}$ | Favre' averaged quantity |
| $(\ )''$ | Favre' fluctuating quantity |

**Abbreviations**

| | |
|---|---|
| *ECF* | expanding cylindrical flame |
| *ESF* | expanding spherical flame |
| *PCF* | planar counterflow flame |
| *PDF* | propability density function |
| *TCF* | tubular counterflow flame |

# SUMMARY

The propagation of premixed flames in turbulent flows is a problem of wide physical and technological interest, with a significant literature on their propagation speed and front topology. While certain scalings and parametric dependencies are well understood, a variety of problems remain. One major challenge, and focus of this thesis, is to model the influence of fuel/oxidizer composition on turbulent burning rates. This effect is due to local imbalances between molecular transport of species and heat caused by flow velocity gradients and flame front curvature which are generally referred to as “flame stretch”. The study of this type of phenomena is particularly crucial for understanding the propagation characteristics and structure of hydrogen turbulent premixed flames which are important for the development of several future combustion technologies.

In most turbulent premixed flames of practical interest, chemical reactions that control heat release are confined to thin, wrinkled, convoluted and stretched reacting fronts that separate unburned reactants from burned products. Classical explanations for augmentation of turbulent burning rates by turbulent velocity fluctuations rely on *global* arguments - i.e., the turbulent burning velocity increase is directly proportional to the increase in flame surface area and mean local burning rate along the flame. However, the development of such global approaches is complicated by the abundance of phenomena influencing the propagation of turbulent premixed flames, such as unsteadiness and nonlinearity in the flame response to flow perturbations, turbulence generation due to gas expansion across the flame, and the fact that zones of intense burning are often accompanied by zones of extinction in high stretch sensitivity flames, making it difficult to clearly define a flame area. Emphasizing key governing processes and cutting-off

interesting but marginal phenomena appears to be necessary to make further progress in understanding the subject.

An alternative approach to understand turbulent augmentation of burning rates is based upon so-called “leading points”, which are intrinsically *local* properties of the turbulent flame. Leading point concepts suggest that the key physical mechanism controlling turbulent burning velocities of premixed flames is the velocity of the points on the flame that propagate farthest out into the reactants. It is postulated that modifications in the overall turbulent combustion speed depend solely on modifications of the burning rate at the leading points since an increase (decrease) in the average propagation speed of these points causes more (less) flame area to be produced behind them. In this framework, modeling of turbulent burning rates can be thought as consisting of two sub-problems: the modeling of (1) burning rates at the leading points and of (2) the dynamics/statistics of the leading points in the turbulent flame. The main objective of this thesis is to critically address both aspects, providing validation and development of the physical description put forward by leading point concepts.

To address the first sub-problem, a comparison between numerical simulations of one-dimensional laminar flames in different geometrical configurations and statistics from a database of direct numerical simulations (DNS) is detailed. In this thesis, it is shown that the leading portions of the turbulent flame front display a structure that on average can be reproduced reasonably well by results obtained from model geometries with the same curvature. However, the comparison between model laminar flame computations and highly curved flamelets is complicated by the presence negative (i.e., compressive) strain rates due to of gas expansion across the flame. For the highest turbulent intensity

investigated, local consumption speed, curvatures and flame thicknesses approach the maximum values obtained by the laminar model geometries, while other cases display substantially lower values.

To address the second sub-problem, the dynamics of flame propagation in simplified flow geometries is studied theoretically. Utilizing results for Hamilton-Jacobi equations from the Aubry-Mather theory, it is shown how the overall flame front progation under certain conditions is controlled only by discrete points on the flame. Based on these results, definitions of leading points are proposed and their dynamics is studied. These results validate some basic ideas from leading points arguments, but also modify them appreciably. For the simple case of a front propagating in a one-dimensional shear flow, these results clearly show that the front displacement speed is controlled by velocity field characteristics at discrete points on the flame only when the amplitude of the shear flow is sufficiently large and does not vary too rapidly in time. However, these points do not generally lie on the farthest forward point of the front. On the contrary, for sufficiently weak or unsteady flow perturbations, the front displacement speed is not controlled by discrete points, but rather by the entire spatial distribution of the velocity field. For these conditions, the leading points do not have any dynamical significance in controlling the front displacement speed. Finally, these results clearly show that the effects of flame curvature sensitivity in modifying the front displacement speed can be successfully interpreted in term of leading point concepts.

# CHAPTER 1
# INTRODUCTION

## 1.1 Motivation

Combustion of fossil fuels currently supplies roughly 82% of the world's total energy needs and most projections forecast that the expected increase in power production by other sources (renewables, nuclear, etc.) will cause this percentage to decrease only to about 75% by 2035 [1]. However, increasingly stringent emission requirements, concerns about the effect of carbon dioxide on climate change and ensuring the security/stability of the energy supply chain have created new technological challenges and opportunities.

Most new combustion technologies tend to utilize turbulent lean premixed flames, especially for ground based power production, such as in gas turbine engines. Premixed flames occur when fuel and oxidizer are mixed homogenously before ignition while turbulent flows are common at the high flow rates needed to design combustion devices with sufficient power density. In appropriate circumstances, lean flames emit very low level of pollutants and thus provide an ideal candidate for environmentally friendly engines.

The interaction of turbulence and premixed flames is characterized by a large range of length scales and timescales [2]. First of all, nonreacting constant-density turbulence is in itself a multiscale nonlinear phenomenon, which involves eddies of very different scales, ranging from the scales of the entire flow to much smaller Kolmogorov scales. Secondly, even a laminar flame is a multiscale nonlinear phenomenon because the rates of different reactions within the flame may differ by several orders of magnitudes and depend

exponentially on temperature. Thirdly, chemical reactions interact with molecular transport processes (mass diffusion and heat transfer), with each characterized by its own length and time scales. The richness and complexity of these physical phenomena explain why premixed turbulent flame theory is still an open problem despite the long history of industrial use, the knowledge of the underlying physical laws and balance equations, and the advancements in laser diagnostic techniques and computer hardware/software [3]. With the exception of the simplest cases, such multiscale nonlinear problems are not tractable either analytically or numerically even using the most powerful computers available today. Accordingly, simplified methods are required to evaluate the basic characteristics of a premixed turbulent flame.

Problems related to the modeling of the multiscale nature of turbulent premixed flames are exacerbated for fuel/oxidizer mixtures characterized by high reactivity and widely different heat and species diffusivities, such as lean hydrogen/air flames. In fact, it is well known that the propagation of turbulent premixed flames is substantially affected not only by turbulence characteristics and laminar flame speed, $s_{L0}$ (defined in detail in the next chapter), but also by the differences between the molecular diffusion coefficients of the fuel, $D_F$, the oxidant, $D_O$, and molecular thermal diffusivity, $\lambda/(\rho c_p)$, of the mixture. Moverover, these effects are of importance not only at weak, but also at moderate and high turbulence intensities [4].

The study of these phenomena has a renewed urgency since hydrogen combustion plays a substantial role in several future applications. The most obvious advantages of hydrogen as a fuel over hydrocarbons are its potential to be produced from water or renewable resources (e.g. biomass) and zero emissions of carbon dioxide from its combustion.

Furthermore, hydrogen combustion is characterized by high burning velocities at equivalence ratios far below the lean flammability limits of hydrocarbon-air mixtures [4]. This implies a relatively low flame temperature and, as a consequence, a drastic reduction in pollutant emissions (such as nitrogen oxides). These same features make $H_2$ a very promising additive able to substantially improve the lean burning performance of conventional hydrocarbon. Finally, hydrogen combustion also plays a role in the development of "clean coal" technologies that rely on combustion of gasified coal, commonly referred to as "synthesis gas" or "syngas" [5].

With these motivations in mind, this thesis studies some of the mechanisms behind the propagation and structure of turbulent premixed flames. In particular, the so called "leading point concept" approach is examined in detail; this approach was specifically devised in order to propose a description of the interaction of turbulence and premixed flames characterized by large differences between mass and heat transport coefficients, which is the focus of this thesis.

The subsequent section of this chapter reviews relevant experimental data that exemplify the influence of molecular transport coefficients on turbulent premixed flames propagation and structure to further motivate this thesis work. This chapter then concludes outlining the scope and organization of this thesis.

## 1.2 Molecular transport effects on turbulent premixed flame propagation and structure: experimental evidence

This section reviews a few experimental studies that illustrate the influence of molecular transport coefficients on turbulent flame propagation and structure. For simplicity, two categories of experiments are distinguished: turbulent flame speed measurements and investigations of the small scale structure of turbulent flames.

Turbulent flame speed $s_T$ can be defined as the average rate of propagation of a turbulent premixed flame. More precise and physically meaningful definitions of turbulent flame speed depend on the geometrical configuration of the experiment [6, 7], but, since the following discussion is restricted only to qualitative trends in the behavior of $s_T$, these issues are not described here. The effects of differences between molecular transport coefficients on $s_T$ have been known for a long time, since the mid-1950s [8], and in the literature there are several databases that clearly show these effects. It is possible to distinguish two different types of experimental $s_T$ measurements that show the effect of molecular transport.

The first type consists in measuring turbulent flame speeds of selected fuel/oxidizer mixtures characterized by equal laminar flame speeds $s_{L0}$, but with different molecular transport properties. For example, Venkateswaran et al. [9-11] measured turbulent flame speeds, shown in Figure 1-1, in a turbulent Bunsen burner for different $H_2$/CO/air mixtures, where equivalence ratios $\phi$ and percentages of $H_2$ and CO were controlled independently to obtain mixtures characterized by the same laminar flame speed, $s_{L0} = 34 cm/s$. Since hydrogen is much more diffusive than carbon monoxide, varying the

concentration of $H_2$ in the fuel substantially alters its molecular diffusivity $D_F$. Figure 1-1 shows that this substantially affects measured turbulent flame speeds. In particular, turbulent flame speeds rise monotonically with increasing $H_2$ concentration in the fuel, and this effect persists even at the highest measured turbulence intensities $u'$. Another example of this typology of measurements is represented by the data collected by Kido and Nakahara [12-15] in spherical bomb experiments. In Figure 1-2, $s_T$ values are shown for $H_2/CH_4/O_2/N_2$ mixtures, where different blends with the same laminar flame speed, $s_{L0} = 15 cm/s$, are obtained by adjusting the $O_2/N_2$ ratio in the oxidizer and the $H_2/CH_4$ ratio in the fuel at constant equivalence ratio $\phi = 0.8$. Similarly to Figure 1-1, these data show that turbulent flame speeds rise monotonically with increasing concentration of $H_2$ in the fuel, since methane, like carbon monoxide, is less diffusive than hydrogen. Other examples of these typology of measurements can be found in Ref. [4].

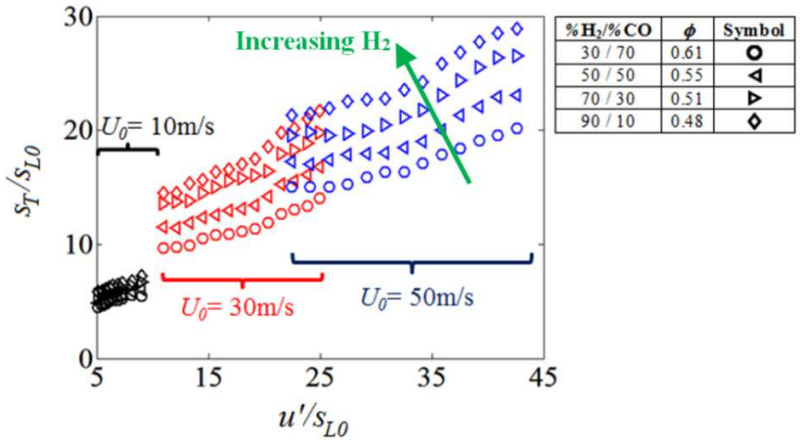


**Figure 1-1. Dependence of turbulent flame speed $s_T$ on turbulence intensity $u'$ measured in the turbulent Bunsen burner facility of Venkateswaran et al. [11]. Different symbols refer to different $H_2$/CO/Air mixtures with equal laminar flame speed $s_{L0}$ = 34*cm/s*: molar concentrations (by percentage) of hydrogen/carbon monoxide in the fuel and equivalence ratios $\phi$ of the different mixtures are listed in the legend on the right. Different colors refer to different mean flow exit jet velocities $U_0$ in the Bunsen burner.**

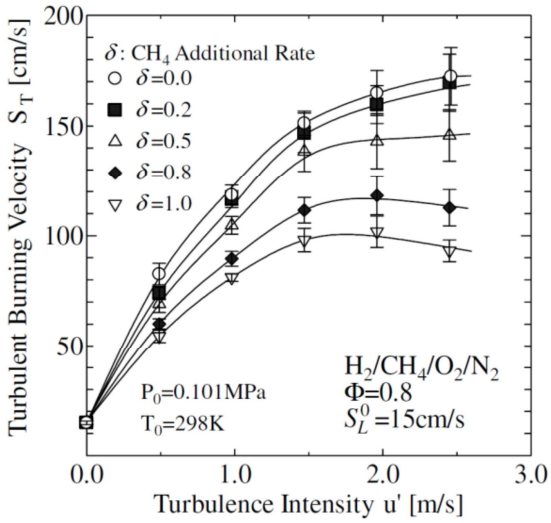


**Figure 1-2. $s_T$ as a function of the turbulent intensity *u'* for $CH_4/H_2/O_2/N_2$ mixtures measured in spherical bombs experiments. Laminar flame speed $s_{L0}$ is kept equal to 15*cm/s* across the different mixtures with constant equivalence ratio $\phi$ = 0.8 by varying the $O_2/N_2$ ratio in the oxidizer [15]. Different symbols refer to different $CH_4/H_2$ fuel blends: molar concentration of hydrogen and methane in the fuel are equal to 1-$\delta$ and $\delta$, respectively.**

The second type of experimental $s_T$ measurements that show the effect of molecular transport compare the equivalence ratio associated with the maximum laminar flame speed, $\phi_{\max(s_{L0})}$ , and the equivalence ratio associated with the maximum turbulent flame speed, $\phi_{\max(s_T)}$, for mixtures characterized by large differences among $D_F$, $D_O$ and $\lambda/(\rho c_p)$. As an example, Figure 1-3 shows experimentally measured values of laminar flame speeds and turbulent flame speeds (measured in spherical bomb experiments at constant turbulence intensity $u' = 2.5\,m/s$ ) at different equivalence ratios for propane/air mixtures (Figure 1-3a) and hydrogen/air mixtures (Figure 1-3b), with data taken from Ref. [4]. For propane/air, the maximum turbulent flame speed is reached at a richer equivalence ratio than the maximum laminar flame speed, and vice versa for hydrogen/air. In general, experimental data show that all mixtures characterized by

$D_F < D_O$ display a behavior similar to $C_3H_8$/air, with $\phi_{\max(s_{L0})} < \phi_{\max(s_T)}$, while mixtures characterized by $D_F > D_O$ display a behavior similar to $H_2$/air, with $\phi_{\max(s_{L0})} > \phi_{\max(s_T)}$.

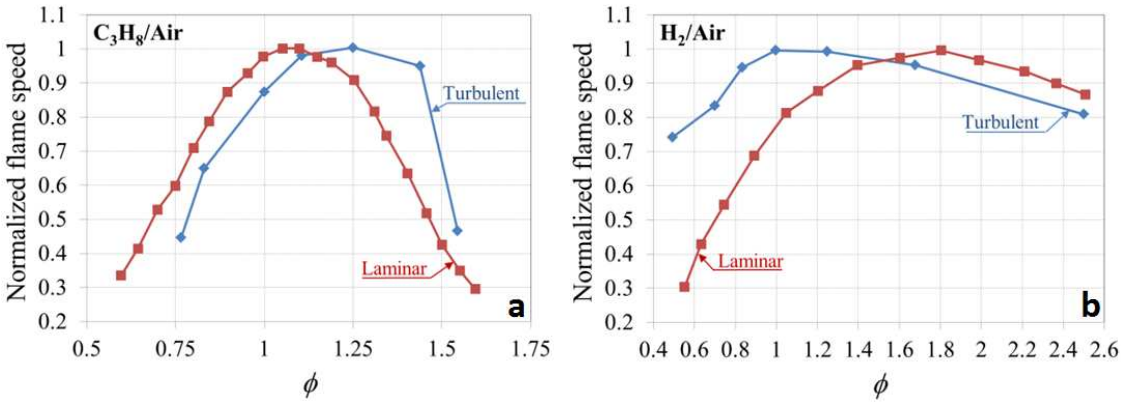


**Figure 1-3. Experimentally measured values of laminar and turbulent flame speeds vs equivalence ratio $\phi$ for $C_3H_8$/Air (a) and $H_2$/Air (b). Turbulent flame speeds are measured at constant turbulent intensity *u'* = 2.5*m/s* in spherical bomb experiments. Flame speed data are normalized by the maximum value. Data adapted from Ref. [4].**

Finally, experimental investigations of molecular diffusion effects on the small scale structure of turbulent premixed flames are generally more recent than turbulent flame speed measurements, since in this type of study it is necessary to employ modern laser diagnostics. Here only a few relevant examples are mentioned. Figure 1-4 shows a set of planar laser induced OH fluorescence (OH PLIF) images [16] taken in the low swirl burner (LSB) of Bedat and Cheng [17], for propane/air, methane/air and hydrogen/air turbulent premixed flames propagating in similar turbulent flow fields. The three flames have markedly different appearance, especially the $H_2$/air flame. Taking the intensity of the OH PLIF signal as an approximate measure of the local burning rate, it is clear that the hydrogen/air flame tends to burn very intensely at positions where the flame front is convex toward the reactants while the flame is effectively extinguished where the flame

front is convex toward the products. On the contrary the methane/air flame tends to burn uniformly along the flame front and the propane/air flame displays somewhat enhanced burning rates along flame front elements that are convex toward the products.

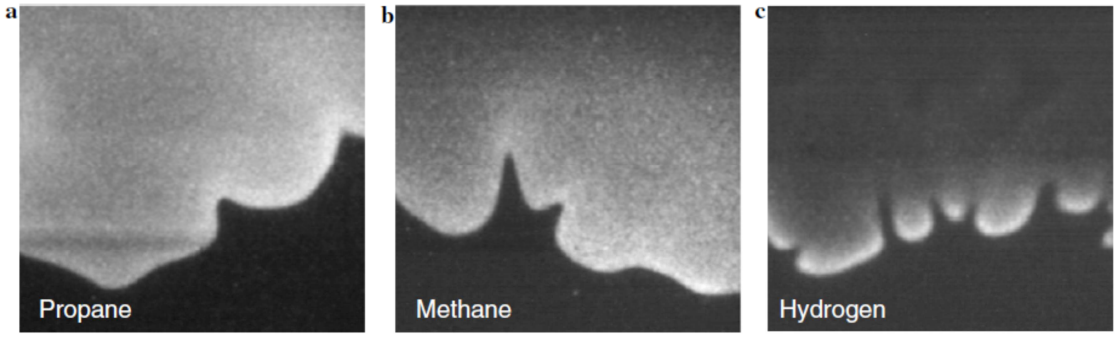


**Figure 1-4. OH PLIF images of $C_3H_8$/Air at $\phi$ = 0.7 (a), $CH_4$/Air at $\phi$ = 0.8 (b) and $H_2$/Air at $\phi$ = 0.27 (c) turbulent premixed flames taken in a LSB burner at turbulent intensity $u'$=18.5*cm/s* and integral length scale $l_t$ =3.0*mm* (corresponding to $u'/s_{L0}$~1 and $l_t/\delta_{T0}$~5) [16]. Fresh reactants are flowing upward from below. The image width corresponds to 3*cm* in physical dimensions.**

To illustrate in more detail the structure of turbulent lean hydrogen/air flames, Figure 1-5 shows iso-contours of temperature based progress variable $C_T = \left(T - T^u\right) \Big/ \left(T_{ad} - T^u\right)$ and of OH mole fraction $X_{OH}$ measured in the turbulent Bunsen burner of Chen and Bilger [18] utilizing two-sheet Rayleigh scattering and OH PLIF. From these data it can be seen that at bulges convex toward the reactants, $C_T$ and $X_{OH}$ iso-contours remain close to each other, indicating a strong local heat release rate and intense chemical reactions. At points convex toward the products, instead, $C_T$ and $X_{OH}$ iso-contours are contorted by turbulence and display distorted features, indicating a low local heat release rate.

The simplest explanation of these different flame appearances is as follows: for lean mixtures, if $D_F > D_O$ ($H_2$/air), the local composition at flame front elements that are

curved toward the reactants tends to stoichiometric and the local burning rate increases, and vice versa if $D_F < D_O$ ($C_3H_8$/air). These different local behaviors are a manifestation of so called "preferential diffusion" and "Lewis number" effects, which are responsible for the $s_T$ trends shown at the beginning of this paragraph and are described in detail in Chapter 2.

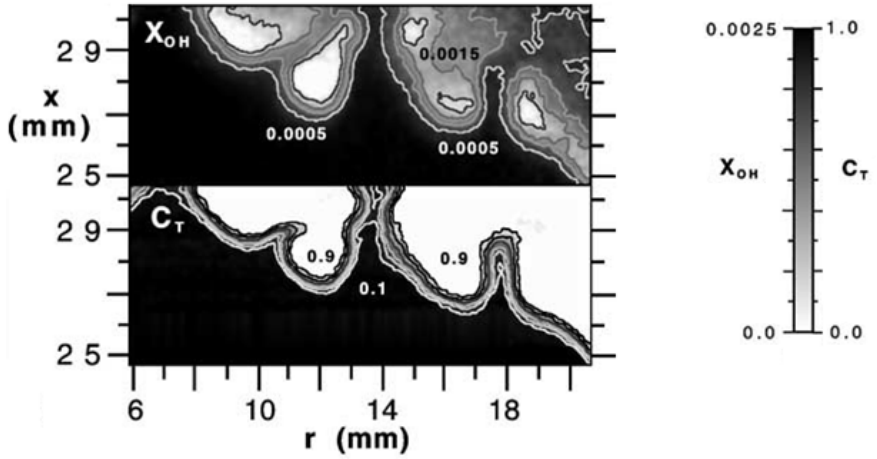


**Figure 1-5. Instantaneous grayscale images of the temperature-based combustion progress variable, $C_T = (T-T^u)/(T^{b,0}-T^u)$, and the mole fraction, $X_{OH}$, of OH radicals in a lean ($\phi$ = 0.325) hydrogen–air turbulent Bunsen flame [18]. The $C_T$ image is overlaid with isocontours of $C_T$ = 0.1, 0.2, 0.3, 0.5, 0.7, and 0.9. The $X_{OH}$ image is overlaid with isocontours of $X_{OH}$ = 0.0005, 0.0010, 0.0015, and 0.0020.**

## 1.3 Scope and organization of the thesis

To summarize the previous sections, it is quite apparent that although the propagation characteristics and structure of turbulent premixed flames have been studied for many years, there are still a number of unresolved issues. In particular, modeling the influence of fuel/oxidizer composition on turbulent flame propagation and structure represents a

major challenge. This issue has received increasing attention in the last few years because of new technologies related to hydrogen combustion.

The main objective of this thesis is to critically investigate and develop ideas put forward by so called “leading point concepts”. As described in detail in Section 2.4, this concept stresses the importance of particular structures (leading points) in determining the overall rate of propagation of turbulent premixed flames. Two sub-problems are fundamental for understanding this concept:

1) What is the burning rate and structure of leading points?
2) What is the role of these structures in determining the turbulent flame speed?

This thesis describes a theoretical and numerical study exploring the answers to these two main questions. Chapter 2 provides background on literature relevant to this thesis work. Chapter 3 investigates the burning rate and structure of leading points detailing a numerical study in which statistics obtained from a DNS database of turbulent premixed flames are compared to a series of model laminar flame computations. Chapter 4 investigates the role of these structures in determining the turbulent flame speed detailing a theoretical study based on the so called G-equation. Chapter 5 presents conclusions and recommendations for future work.

# CHAPTER 2
# BACKGROUND

This chapter provides background on literature relevant to this thesis work. Section 2.1 briefly reviews preferential diffusion and Lewis number effects in laminar premixed flames as a starting point to understand their influence in turbulent flames. Section 2.2 provides a general overview of turbulent premixed modeling with a focus on the "flamelet" paradigm. Section 2.3 reviews past direct numerical simulations (DNS) studies that investigated the role played by preferential diffusion and Lewis number effects in turbulent premixed flames. Finally Section 2.4 describes in detail the leading points concept.

## 2.1 Preferential diffusion and Lewis number effects

Laminar premixed flames are deflagration waves (i.e. with little change in pressure between unburnt and burnt side) propagating in homogeneous mixtures of fuel and oxidizer. Put simply, the physical mechanism of premixed flame propagation consists of the following steps: chemical reactions produce heat and new chemical species; a part of the produced energy diffuses toward the fresh mixture due to molecular diffusion of heat and species; local temperature and radical concentrations increase and trigger new chemical reactions which then move more toward the fresh mixture. Therefore, the flame propagation is controlled by molecular transport processes and chemical reactions.

The first level of idealization of laminar, premixed flames is one where the flame and flow are one-dimensional and steady. This is known as the "unstretched laminar flame",

and the associated burning rate is called the "unstretched laminar flame speed", $s_{L0}$. As an example, the typical structure of a one-dimensional unstretched laminar methane/air flame is shown in Figure 2-1 [19]. Its structure consists of three layers: (1) the upstream chemically inert preheat zone, (2) a thin, fuel consumption layer, also called the reaction zone or inner layer and (3) another thin, oxidation layer. Downstream of the oxidation layer is the equilibrium, fully reacted state of the mixture.

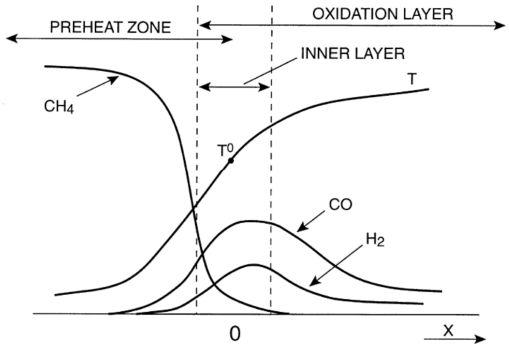


**Figure 2-1. Schematic illustrating the typical structure of a methane/air laminar premixed flame. Adapted from Ref. [19]**

When premixed flames propagate in non-uniform flow fields or are curved, this one-dimensional flame structure can change substantially. Theoretical studies of perturbed laminar premixed flames have shown that a useful quantity to parametrize modifications in flame structure is the so called stretch rate $\kappa$. In the following, a brief overview of stretched premixed flames is presented with a focus on phenomena relevant for this thesis and mostly drawn from Clavin's review of early asymptotic studies [20], Law and Sung's review of integral methods [21] and the flamelet formalism of de Goey et al. [22].

In the limit of an infinitesimally thin flame, the local stretch rate is defined as the fractional rate of increase in surface area $A_T$:

$$\kappa = \frac{1}{A_T}\frac{dA_T}{dt} \tag{2.1}$$

This quantity is also important in turbulent non-reacting diffusion processes since in isotropic homogeneous turbulence the mean stretch rate controls the rate of area increase of material surfaces [23]. Through the use of vector geometry (see for example Ref. [24, 25]), an expression for stretch rate can be written as

$$\kappa = \nabla_{\not t} \cdot \vec{u}_{\not t} + \left(-s_L + \vec{u} \cdot \vec{n}\right)\left(\nabla \cdot \vec{n}\right) \tag{2.2}$$

where (see Figure 2-2) $\vec{u}$ represents the flow velocity, $s_L$ is the flame self-propagation speed, $\vec{n}$ represents a unit vector normal to the flame surface pointing toward the product side, $K_C = -\nabla \cdot \vec{n}$ represents the flame sheet mean curvature (the sum of the inverses of the principal radii of curvature of the surface) and

$$\nabla_{\not t} \cdot \vec{u}_{\not t} = -\vec{n} \cdot \nabla \times (\vec{u} \times \vec{n}) \tag{2.3}$$

By convention, the sign of $K_C$ is defined as positive when the center of curvature of the flame surface is situated in the product side (flame element convex toward the reactants). For cylindrical and spherical flame surfaces, the absolute value of $K_C$ is equal to $1/R$ and $2/R$, respectively, where $R$ represents the radius of curvature. The first term in equation (2.2) is known as "hydrodynamic stretch" and represents the stretching of the

flame sheet by the tangential flow velocity component $\vec{u}_t$. The second term, instead, represents stretch rate due flame curvature $K_C$ in combination with flame motion.

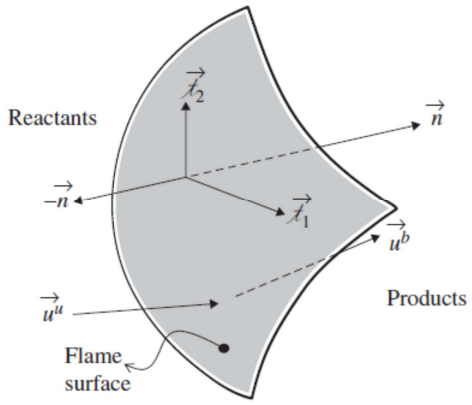


**Figure 2-2. Schematic showing flame coordinate system used to derive flame stretch expressions. Adapted from Ref. [26].**

Equation (2.2) can also be rearranged into other terms that more explicitly illustrate the role of flow non-uniformity and flame curvature:

$$\kappa = -\vec{n}\vec{n} : \nabla\vec{u} + \nabla\cdot\vec{u} - s_L \nabla\cdot\vec{n} = -\frac{\partial u_n}{\partial n} + \nabla\cdot\vec{u} + s_L K_C \tag{2.4}$$

where $\partial u_n / \partial n$ is the derivative of the flow velocity normal component $u_n$ in the direction normal to the flame surface $n$. The term

$$K_S = -\vec{n}\vec{n} : \nabla\vec{u} + \nabla\cdot\vec{u} \tag{2.5}$$

is known as “tangential strain” and represents the contribution of flow velocity spatial gradients to flame stretch. In particular, the first term $-\vec{n}\vec{n}:\nabla\vec{u}$ represents the effect of flow velocity gradients normal to the flame surface, while the second term $\nabla\cdot\vec{u}$ is zero for isodensity flows, but inside the flame is non-zero due to heat release which brings about gas expansion. Equation (2.5) can also be rewritten as

$$K_S = \nabla_{/\!/}\cdot\vec{u}_{/\!/} + (\vec{u}\cdot\vec{n})(\nabla\cdot\vec{n}) = \nabla_{/\!/}\cdot\vec{u}_{/\!/} - (\vec{u}\cdot\vec{n})K_C \tag{2.6}$$

This expression stresses the fact that $K_S$ is not independent from curvature $K_C$.

To understand the physical process through which the hydrodynamic stretch rate affects the structure of premixed flames, let us consider a flat flame in a divergent flow field, depicted in Figure 2-3. This geometry can be realized experimentally by stagnating a premixed reactant stream against a wall. The resulting flame is flat ($K_C = -\nabla\cdot\vec{n} = 0$) and, thus, it is only subject to hydrodynamic stretch since $\vec{u}_{/\!/} \neq 0$. In Figure 2-3, convective transport, depicted by streamlines, and diffusive transport of heat and mass are clearly indicated; a control volume can be drawn as shown, where the sides are bound by streamlines across which diffusive transfer can occur but not convective transfer. The physical manifestations of hydrodynamic stretch, which are described below, are a result of the misalignment between the convective and diffusive directions. Since the flame is a source of heat and a sink for reactants, heat diffuses normal to the flame out of the control volume, while reactants diffuse into the control volume towards the flame from exterior streamtubes.

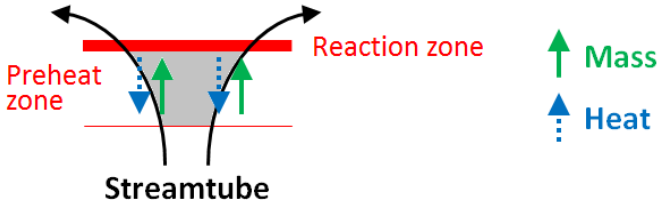


**Figure 2-3. Illustration of the internal structure of a hydrodynamically stretched flame showing misalignment of convective and diffusive fluxes. Grey region denotes the control volume.**

The relative importance of these two processes can be assessed by considering the Lewis number defined as $Le = \lambda/\left(\rho c_p D\right)$, where $\lambda/\left(\rho c_p\right)$ is the mixture thermal diffusivity and $D$ is a reference mass diffusivity, often taken as that of the deficient reactant. Lewis number effects can be understood by considering the energy balance in the control volume illustrated in Figure 2-3, which can be written as

$$\rho\vec{u}\cdot\nabla h_T = -\nabla\cdot\vec{q} \tag{2.7}$$

where $h_T$ is the total enthalpy per unit mass, $\rho$ represents the density and $\vec{q}$ is the local heat flux. This equation describes the balance between convective (left side) and diffusive (right side) fluxes. Neglecting radiative heat transfer and the DuFour effect, and assuming Fickian diffusion, the heat flux vector is given by

$$\vec{q} = -\lambda\nabla T - \rho\sum_{i=1}^{N} h_i D_i \nabla Y_i \tag{2.8}$$

where $T$ is the temperature, $c_p$ represents the specific heat capacity and $Y_i$, $D_i$, $h_i$ are the mass fraction, mass diffusivity and enthalpy of the *i*-th species, respectively. Equation (2.8) shows that energy flux occurs through both heat and mass diffusion. Thus, for the flame of Figure 2-3, energy flows in through the sides of the control volume through heat transfer, but also flows out through the sides through mass transfer of chemical energy associated with the reactants. If the heat and mass diffusion coefficients are the same, i.e., $Le = 1$, then these effects cancel for weakly curved flames and the energy balance in the control volume is not disturbed by these diffusive fluxes. These effects do not balance, however, if $Le \neq 1$ leading to an increase or decrease in thermal energy in the control volume.

Another diffusion-based phenomenon associated with stretch, known as preferential diffusion, occurs when the reactant constituents have large variations in mass diffusivities. To illustrate, consider Figure 2-3 for a lean $H_2$/air mixture. Both $H_2$ and air will diffuse into the control volume, but since $H_2$ is lighter than air, it will diffuse faster. Consequently, this causes the local equivalence ratio to increase towards stoichiometric, resulting in a higher flame temperature and flame speed. For a rich $H_2$/air mixture, similar arguments can be made to show that the local equivalence ratio will become even richer resulting in a lower flame temperature and flame speed. Similar lines of reasoning can also be employed for $C_3H_8$/air flames, which experience opposite effects since $C_3H_8$ is now heavier than air.

The physical mechanism through which curvature modifies the structure of premixed flames can be explained in a way analogous to hydrodynamic stretch. Figure 2-4 shows the mass and heat diffusive fluxes of a curved flame and, for comparison, of a planar

flame. From these two figures it is clear that in curved flames heat and mass fluxes are focused/defocused depending on the sign of the mean curvature $K_C$. If there is an imbalance due to non-unity Lewis number or preferential diffusion effects, then the energy balance at the reaction zone can be affected in ways similar to the energy balance of the control volume depicted in Figure 2-3.

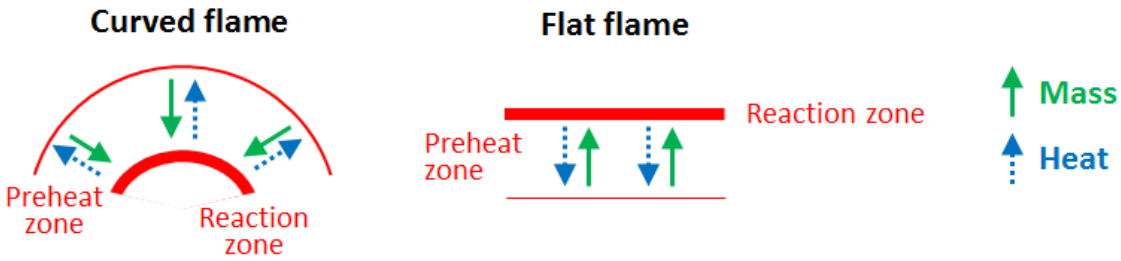


**Figure 2-4. . Illustration of the internal structure of a curved flame and a planar flame showing focusing/defocusing of diffusive fluxes in curved flames.**

Early studies which analyzed the effects of stretch on flames utilizing irreversible, one-step chemistry and asymptotic analysis methods, found the following linear relation for the flame speed of stretched flames in the limit of weak stretch [20]:

$$s_L = s_{L0} - \ell \kappa \tag{2.9}$$

where $\ell$ is the Markstein length, which can take on both positive and negative values. Equation (2.9) can be non-dimensionalized using the un-stretched laminar flame speed, $s_{L0}$, and the associated flame thickness, $\delta_{F0}$, to obtain:

$$s_L / s_{L0} = 1 - Ma\, Ka \tag{2.10}$$

where $Ma$ is the Markstein number, defined as $Ma = \ell / \delta_{F0}$, and $Ka$ represents the Karlovitz number, defined as $Ka = \kappa \delta_{F0} / s_{L0}$. The previous discussion on Lewis number and preferential diffusion effects suggests that $Ma$ should be a function of Lewis number, relative diffusivities of fuel and oxidizer, and fuel/air ratio. For example, the differential diffusion arguments described in this section suggest that lean mixtures of lighter than air fuels, such as methane or hydrogen, should have enhanced flame speeds for positively stretched flames (i.e., that $Ma < 0$). These arguments also suggest that $Ma > 0$ for rich fuel/air blends with these fuels, and that these trends should be inverted for fuels that are heavier than air, such as propane.

Linear expressions, such as equations (2.9) and (2.10), have limited applicability and more quantitative discussions about the influence of Lewis number and preferential diffusion effects on premixed flames structure require a more detailed discussion of flame speed definitions, nonlinear effects and unsteady effects, which are discussed next.

### 2.1.1 Flame speed definitions

The "speed" of premixed flames is a central element in combustion theory: there are multiple definitions and multiple ways to measure them. The main difficulty in defining a flame speed arises from the fact that a real flame has a finite thickness, yet a propagation velocity asserts the presence of a combustion *front*. Generally, a contour $c_F$ of a reaction-progress indicator $c$ (like a temperature isosurface or a mass fraction isosurface of either the fuel or the oxidizer) is chosen to represent the flame front.

Arguably, the most natural physical definition should be tied closely to the rate of reactants mass consumption (or, conversion to combustion products). Unfortunately, reaction rates are difficult to measure experimentally and this type of definition is mostly applied in computational studies. Poinsot et al. [27] defined the consumption speed $s_{c,P}$ as the speed corresponding to the mass flow rate of fresh gases consumed through the flame front and is defined by

$$s_{c,P} = \frac{1}{\rho^u Y_F^u} \int_{-\infty}^{+\infty} \dot{\omega}_F dn \tag{2.11}$$

where $\dot{\omega}_F$ is the mass of fuel consumed per unit volume and unit time, $\rho^u$ is the density of the unburnt gases and $Y_F^u$ is the mass fraction of fuel in the reactants. The integration in (2.11) is performed along the normal $n$ to the flame front defined by the isosurface $c = c_F$.

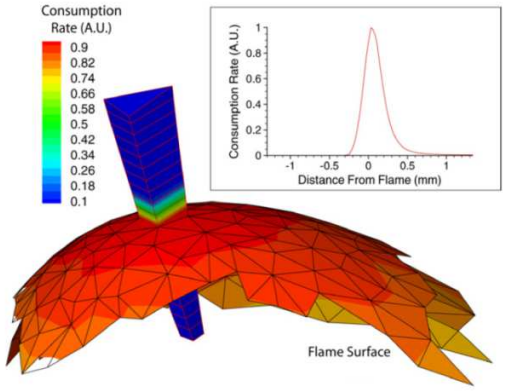


**Figure 2-5. Prism shaped volume, $\Omega$, constructed using curves locally normal to the temperature isotherms. The inset plot shows a typical variation of $\dot{\omega}_F$ normal to the flame surface. Reproduced from Day and Bell [28].**

An alternative definition of consumption speed, more numerically robust and less sensitive to the particular choice of $c_F$, was proposed by Day *et al.* [28]. This definition starts with the tessellation of the flame front $c_F$, and the construction of normal vectors by extending them along integral curves of temperature gradient. A prism, Ω, can then be built as shown in Figure 2-5. The consumption speed $s_c$ is calculated integrating the fuel mass consumption rate $\dot{\omega}_F$ over the Ω volume and normalizing by the area $A_{ref}$, intersection between Ω and the flame surface, multiplied by the initial fuel density contained in the reactants $\rho^u Y_F^u$:

$$s_c = \frac{\int_\Omega \dot{\omega}_F d\Omega}{\rho^u Y_F^u A_{ref}} \tag{2.12}$$

Another definition for flame propagation speed is the "displacement speed" $s_d$ of a contour of a reaction-progress indicator $c_F$. An expression for the displacement speed of an isoscalar surface relative to the flow field was developed by Poinsot et al. [29, 30] and Echekki et al. [31]. The analysis is based on tracking a surface on which the mass fraction, $Y$, of the deficient reactant is fixed to a value. The governing transport equation for $Y$ is:

$$\frac{\partial Y}{\partial t} + \vec{u} \cdot \nabla Y = \frac{1}{\rho} \nabla \cdot \left( \rho D \nabla Y \right) + \frac{\dot{\omega}}{\rho} \tag{2.13}$$

The left-hand side of the equation is the convective derivative where $\vec{u}$ is the gas velocity at the surface. This term balances the sum of diffusion and reaction terms on the right-hand side of the equation. The velocity of $Y$ isocontours, $\vec{v}_F$, is the sum of both the convective component, $\vec{u}$, and its propagation relative to the gas, $-s_d\vec{n}$:

$$\vec{v}_F = \vec{u} - s_d\vec{n} \tag{2.14}$$

In this expression, $s_d$ is the magnitude of the propagation velocity of the isocontour normal to itself and $\vec{n}$ is the unit normal vector of the isocontour of $Y$ directed toward the burnt gas which may be expressed in terms of the normalized local gradient vector of $Y$:

$$\vec{n} = -\frac{\nabla Y}{\|\nabla Y\|} \tag{2.15}$$

Equation (2.14) also forms the basis for experimental measures of flame speeds from particle image velocimetry (PIV) data, such as in the study of Sinibaldi et al. [32, 33], who studied displacement speed of premixed laminar flames encountering toroidal vortex rings, and Renou et al. [34, 35], who studied weakly turbulent premixed flames. By fixing the value of $Y$ at the surface, the following expression is obtained:

$$\frac{\partial Y}{\partial t} + \vec{v}_F \cdot \nabla Y = 0 \tag{2.16}$$

By substitution of Eq. (2.13) into (2.16), an expression for the displacement speed, $s_d$, is obtained:

$$s_d = -\frac{\nabla\cdot(\rho D\nabla Y)}{\rho\|\nabla Y\|} - \frac{\dot{\omega}}{\rho\|\nabla Y\|} \tag{2.17}$$

This expression shows that the value of the displacement speed is a result of the balance between reaction and diffusion, and is modulated by the value of the gradient of the scalar at the location where it is measured. Many analyses [36] have also shown that it is convenient to split the diffusive term into a normal and a tangential component as

$$s_d = \underbrace{-\frac{\dot{\omega}}{\rho\|\nabla Y\|}}_{s_r} \underbrace{-\frac{\frac{\partial}{\partial n}\left(\rho D\frac{\partial Y}{\partial n}\right)}{\rho\|\nabla Y\|}}_{s_n} \underbrace{-DK_C}_{s_t} \tag{2.18}$$

where $n$ is the normal coordinate across the flame and $K_C$ is the mean curvature defined as in Eq. (2.2). This expression shows that $s_d$ is determined by the contributions of three terms: (i) reaction $s_r$, (ii) normal diffusion $s_n$, and (iii) curvature (tangential diffusion) $s_t$. Both reaction and normal diffusion are essential components of any normal flame propagation, while the third term, curvature, is only present when the flame is curved. Equation (2.18) also shows that the explicit contribution of curvature is linear, with the slope corresponding to the local molecular diffusion coefficient. However, there is

curvature dependence in the remaining terms, and especially reaction, through the coupling of differential and preferential diffusion effects with curvature.

Because of gas expansion through the flame, the displacement speed with respect to the unburned, $s_d^u$, and burned, $s_d^b$, flow is different. These definitions can be generalized to refer to the speed of the flow with respect to any chosen temperature or concentration iso-surface in the flame. This dependence of flame speed upon chosen flame iso-surface is not too problematic for weakly stretched flames since the approach flow velocity varies weakly upstream of the flame and these effects may be largely eliminated by using the density-weighted displacement speed, $s_d^*$

$$s_d^* = \frac{\rho s_d}{\rho^u} \tag{2.19}$$

In fact in a flat, unstretched flame, the mass burning rate is constant $\rho^u s_{d,0}^u = \rho^b s_{d,0}^b$ and represents a well defined quantity, invariant for any choice of reference surfaces through the flame. Instead in highly stretched flames, the mass flux through the flame itself varies significantly through the flame and the definition of displacement speed becomes ambiguous. In highly stretched flames, the flow velocity gradients occur over length scales that are on the order of the flame thickness. Therefore, slight changes in choice of iso-surface can yield very different values of flame speed. An example of this phenomenon is provided in Figure 2-6, where the mass burning rate $m = \rho s_d$ is plotted for a series of numerical computations of stationary spherical $CH_4$/air flames ($\phi$ = 1.0, $T^u = 300K$ and $p = 1atm$) at different radii, in which burnt gases are present in the

center [37]. This figure shows the mass burning rate calculated at several isotherms, where the one corresponding to ~1640 *K* (inner layer) is the one closest to the reaction zone. The mass burning rate varies with the radius of the flame at all isotherms except at the inner layer where hardly any influence of the radius is observed. At the other isotherms, almost no reactions take place, while convective and diffusive processes play the most important role. Since the flames are curved, the surface area through which the gases flow changes and, as a consequence, the burning velocities change. From this notion, it can be concluded that the mass burning rate of curved flames is best defined at the inner layer instead of defined at the other positions in the flame. For this reason in most numerical analyses, like the direct numerical simulations described in Section 2.3, isosurfaces (of temperature or mass fraction) close the reaction zone are chosen to represent the flame front position. This choice is also motivated by the fact that turbulent eddies penetrate in the reaction zone with more difficulty than in the preheat zone (see "thin reaction zone regime" described in the Section 2.2).

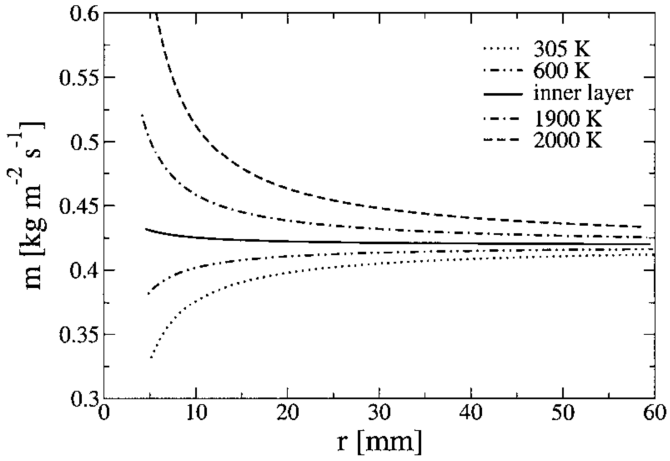


**Figure 2-6. The mass burning rate $m = \rho s_L$ for stationary spherical flames of different radii *r*, with burnt gasses at the center. $CH_4$/Air, $T^u$ = 300*K*, *p*=1*atm*: temperature at the inner layer is 1640K. Reproduced from Ref. [37]**

Moreover, the displacement speed definition for flame speed can lead to counterintuitive results such as local negative displacement speeds, $s_d < 0$, in highly strained flows [36]. This situation occurs in flames with very high concentration gradients where the flame is supplied with reactants by diffusive fluxes strong enough to counteract the bulk flow convection in the opposite direction. This situation can be simulated with a counterflow burner, by stagnating premixed reactants against hot products/inert. At very high strain rates the flame moves across the stagnation surface into the products/inert side and is supplied fuel/oxidizer by diffusive fluxes; then, the displacement speed $s_d$ becomes negative as shown experimentally by Sohrab et al. [38] (see also Section 2.3).

In general, consumption velocity and displacement speed have different values and also depend differently on stretch rate. For this reason it is important to always specify the exact definition utilized to study flame speed. For instance, for weakly stretched flames ( $Ka \ll 1$ ), asymptotic theories predict a linear dependence of $s_{c,P}$ and $s_d$ on the stretch rates, but with different Markstein numbers as shown by the following expressions (see Ref. [4, 39] for the specific assumptions),

$$\frac{s_{c,P}}{s_{L0}} = 1 - Ma_c Ka \tag{2.20}$$

$$Ma_c = \frac{Ze\left(1-1/Le\right)}{2\left(\vartheta-1\right)} \int_1^{\vartheta} \frac{\ln\left(x\right)}{x-1} dx \tag{2.21}$$

$$\frac{s_d}{s_{L0}} = 1 - Ma_d Ka \tag{2.22}$$

$$Ma_d = Ma_c + \frac{\ln \vartheta}{\vartheta - 1} \tag{2.23}$$

where $Ze$ is the Zeldovich number, $\vartheta = \rho^u / \rho^b$ is the density ratio between unburnt and burnt gasses, and $s_d$ is evaluated at the reaction zone. Comparing equation (2.22) and (2.23) it can be observed that in this linear limit displacement and consumption speed respond differently to stretch and may also have opposite signs.

### 2.1.2 Nonlinear and unsteady effects

The response of premixed flames to finite stretch rate values is generally nonlinear. The study of nonlinear effects represents a very active field of research in the combustion community since a comprehensive theory of these effects is still lacking. The non-linear dependencies of premixed flame speed and structure on perturbation magnitude have been documented experimentally [29, 40, 41], numerically [29, 42-45], and predicted theoretically [43, 46-48], just to cite a few examples. For instance, Figure 2-7 plots several theoretical expressions for the dependence of flame speed on Karlovitz number, obtained by asymptotic analysis of single-step chemistry expanding spherical flames in Ref. [41, 48]. In this figure the "LM" curves refer to the linear model of equation (2.23), while "DM" and "SM" are obtained from more detailed models taking into account nonlinearities in the flame response. The curves collapse onto each other only at very low stretch rates (low Karlovitz number) and the effect of nonlinearities is stronger for $Le \neq 1$ (i.e. the linear model LM diverge more quickly from the detailed model DM with increasing Karlovitz number).

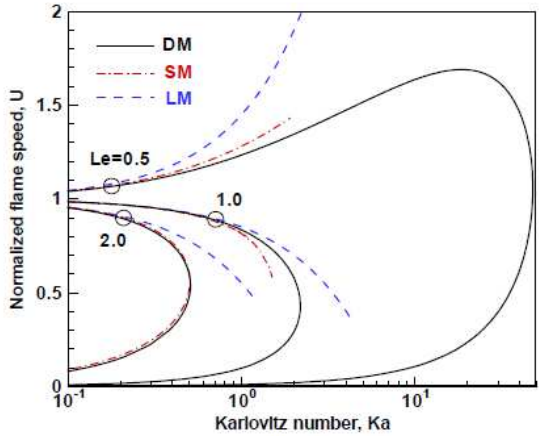


**Figure 2-7. Theoretical dependence of normalized flame speed $U = s_d^b / s_{d,0}^b$ on Karlovitz number $Ka = 2U/R$ for expanding spherical flames (of radius $R$) with different Lewis number, obtained by asymptotic analysis in Ref. [41]. "LM" refers to the linear model of equation (2.10), "DM" is a more detailed model taking into account nonlinearities and "SM" refers to a simplified version of "DM".**

There are several nonlinear effects that are not captured by expressions like equation (2.20)-(2.23) and that are of interest in this thesis:

- different response of premixed flames to curvature and hydrodynamic stretch;
- response to unsteady stretch;
- "critical" stretch rates.

The different response of curved and hydrodynamically stretched flames has been documented numerically [49] and theoretically [50, 51]. Figure 2-8b shows the numerically computed dependence of flame temperature on stretch rate for tubular and planar counterflow flames (shown in Figure 2-8a) of a very lean $H_2$/air mixture, reproduced from Ref. [52]. As it can be observed, for the same value of stretch rate $\kappa$ the two geometrical configurations display a very different flame temperature and, as a consequence, burning rate (not shown here). For the very lean hydrogen air mixture considered in this figure, the flame responds more strongly to curvature rather than

hydrodynamic stretch and for the same value of $\kappa$ the tubular flame display a much higher flame temperature.

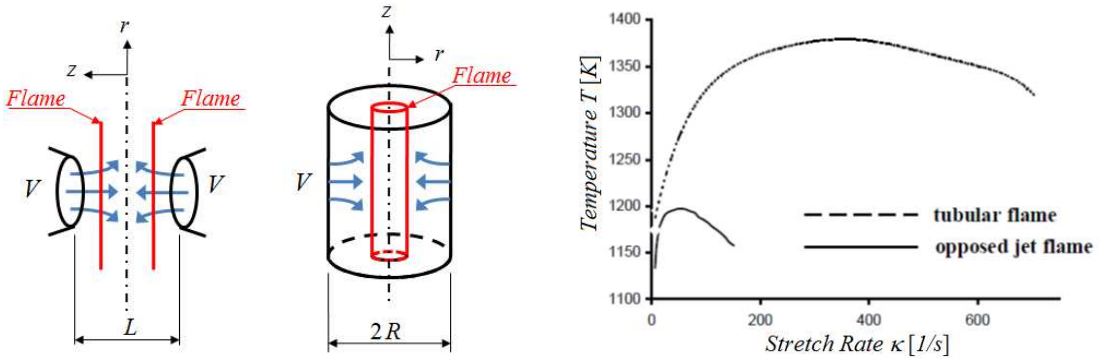


(a) (b)

**Figure 2-8. (a) Sketch of a planar counterflow premixed flame (left) and tubular counterflow premixed flame (right), where *V* is the inflow velocity of the incoming reactants. (b) Numerical computations [52] of flame temperature (temperature calculated at the axis of symmetry) dependence on stretch rate ($\kappa = 2V/R$ and $\kappa = 2V/L$ for planar and tubular counterflow flame, respectively [53]) for $H_2$/Air flames, $\phi = 0.175$, $T^u = 298K$, $p = 1atm$, $L = 1.26cm$, $R = 1.5cm$.**

The different response of premixed flames to curvature and hydrodynamic stretch is also particularly important for the study of premixed flames response to unsteady stretch [54, 55]. As pointed out at the beginning of this chapter, hydrodynamic stretch (Figure 2-3) and curvature (Figure 2-4) depend on two distinct phenomena that are characterized by different time scales: competition between convection and diffusive fluxes for hydrodynamic stretch and focusing/defocusing of diffusive mass and heat fluxes for curvature. The time scale associated with hydrodynamic strain is roughly equal to the time necessary for a fluid particle in the reactants to move from the beginning of the preheat zone to the reaction zone $\tau = \delta_{F0}/s_{L0}$. Premixed flames respond as low-pass filters and phase shifters to unsteady hydrodynamic stretch perturbation at frequencies

higher than $1/\tau$, since the internal flame structure cannot adjust fast enough to external perturbations. To illustrate, Figure 2-9 plots the numerically computed dependence of the instantaneous consumption speed $s_{c,P}$ on instantaneous stretch rate $\kappa$ for a planar counterflow flame where the reactants flow at the inlet is forced harmonically at different frequencies. Note that at low frequencies, the flame behaves much like the steady-state case. However, as the frequency of oscillation is increased, the flame's stretch response decreases, due to the inability of the diffusive processes to keep up with the time-varying strain rate. In fact it is evident that at a frequency of 1000 Hz, the flame is essentially insensitive to the stretch rate.

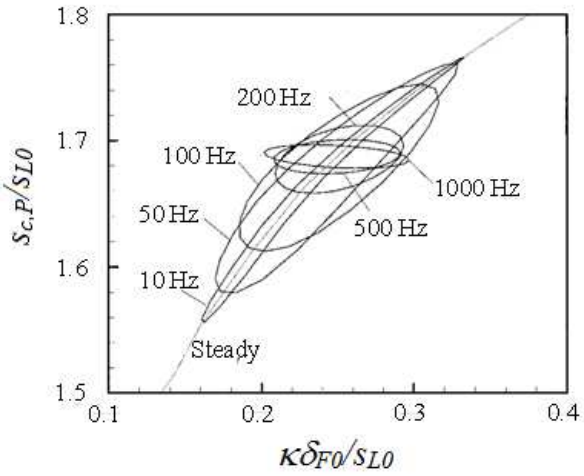


**Figure 2-9. Dependence of instantaneous flame consumption speed, $s_{c,P}$, on the instantaneous stretch rate, $\kappa$, at several frequencies of oscillation from 0Hz (Steady curve) to 1000Hz. Here $\delta_{F0}$ = 0.1*mm* and $s_{L0}$ = 22.15*cm/s* Image reproduced from Ref. [56] ($H_2$/Air flame $\phi$ = 0.4 with reactants at standard temperature and pressure)**

The sensitivity of premixed flames to unsteadiness in flame curvature is quite different. The theoretical study of Clavin and Joulin [54, 55] based on high activation energy asymptotics and single-step chemistry suggests that the frequency response of the

displacement speed $s_d$ to unsteady curvature (1) remains invariant even at high frequencies and (2) becomes independent of preferential diffusion of species and heat as frequency increases (i.e. Lewis number effects tend to disappear at high frequencies). These two effects have been observed in direct numerical simulations of turbulent premixed flames [57, 58] but in the literature these results have not been studied in a manner as detailed as the response of premixed flames to unsteady hydrodynamic stretch, mainly because an experimental configuration as simple as the counterflow flame to study hydrodynamically stretched flames is not available for curved flames. In particular, it is not clear whether analogous considerations are valid also for flame speed definitions based on consumption ($s_{c,P}$ and $s_c$), since direct numerical simulations of turbulent premixed flames show that $s_{c,P}$ generally correlates better with local flame front curvature $K_C$ rather than strain rate $K_S$ [59, 60].

Finally, in many situations there is an upper limit to the response of premixed flames to external perturbations: depending on the geometry and time scale of flame stretching, there might be a maximum or minimum burning rate, depending on the Markstein number, that a premixed flame can sustain before transitioning to a non-burning state (extinction). In this thesis, this condition is loosely referred to as “critical” stretch, following Ref. [4, 61]. Here we mention only the cases of counterflow flames and curved expanding flames as they will be utilized later in Chapter 3; possibly related limit phenomena, which are not described here, are premixed flame quenching by vortices [27, 62, 63], premixed flames propagating along vortex tubes [4, 64] and stationary flame balls [4, 65].

The classical example of a critically stretched premixed flame is represented by planar counterflow twin premixed flames (see sketch in Figure 2-8a) close to extinction. In this geometrical configuration, for low flow velocities the flame is far from the stagnation surface. If the stretch rate is increased, the movement of the flame is unrestrained. In this condition, the flame responds to stretch rate as described at the beginning of this chapter, i.e., the reaction rate and the flame temperature will either decrease or increase, depending on whether $Ma_c > 0$ or $Ma_c < 0$, as shown in Figure 2-10. For $Ma_c > 0$, it is apparent that there exists a critical stretch rate $\kappa_{ext}$ at which the flame temperature will be reduced to such an extent that burning is not possible and a minimum burning rate is achieved. On the other hand, since increasing stretch elevates the flame temperature for the $Ma_c < 0$ flame, extinction cannot occur until the downstream boundary of the reaction zone is pushed onto the stagnation surface and the flame movement becomes restrained. With further stretching, chemical reactions cannot be completed because of the reduced residence time. Only then will the reaction rate and, hence, the flame temperature start to decrease as shown in Figure 2-10. This creates an absolute maximum in the burning rate (a critically stretched flame) at a stretch rate close to $\kappa_{ext}$.

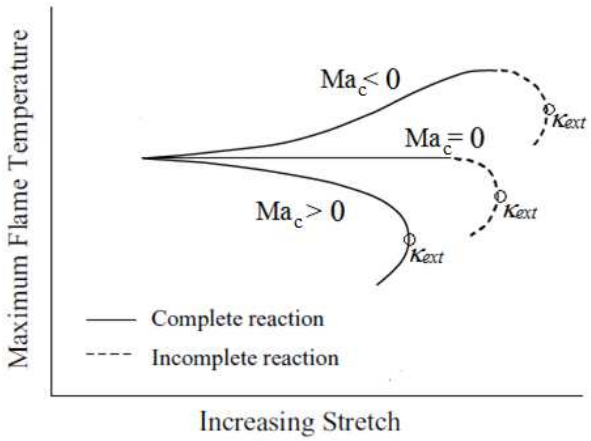


**Figure 2-10. Effect of stretch and reaction incompleteness on the extinction mechanism for flames characterized by different Markstein numbers [66]. Small circles indicate extinction strain rate $\kappa_{ext}$ which is turning point in the flame temperature profile.**

However, if the stagnation surface is permeable as in the case of impinging the combustible mixture against a hot product gas stream of temperature $T^b$, then the reaction zone can actually migrate across the stagnation surface in the product side of the counterflow. In this situation, the flame speed assumes a negative value, as pointed out in Section 2.1.1. Combustion is now supported by diffusion of the reactants across the stagnation surface against convection from the product stream and since there is no loss mechanism involved in such a situation, for sufficiently high temperature of the hot product gas stream extinction is not possible and no critical stretch rate exists. Figure 2-11 delineates this phenomenon showing results from numerical computations of counterflow flames for impinging lean $C_3H_8$/air ($Ma_c > 0$) at standard temperature and pressure against combustion products at temperature $T^b$ [67]. For $T^b > 1530K$, the total heat release rate of the flame display a monotonic behavior with increasing stretch rate and there is no turning point in the flame response; in this case the burning rate gradually decreases to zero with increasing stretch, and there is no critical stretch rate.

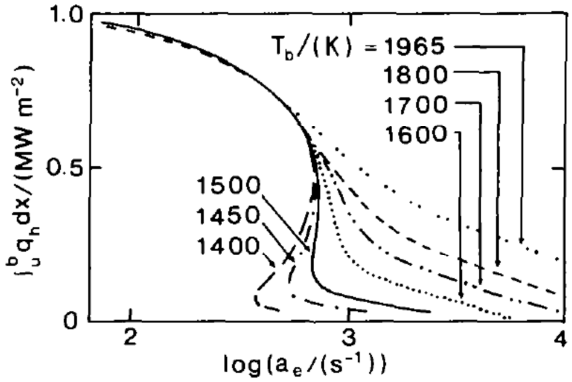


**Figure 2-11. Total heat release rates $\int_u^b q_h dx$ plotted as a function of "applied stress" $a_e$ (a quantity similar to stretch rate) for counterflow flames formed impinging $C_3H_8$/Air, $\phi = 0.75$ at standard temperature and pressure against combustion products at temperature $T_b$. Curves are monotonic when $T_b$>1530K, S-shaped below this value: for $T_b$>1530$K$ no sudden extinction occurs with increasing stretch rate and no critical stretch exists. Reproduced from Ref. [67].**

For curved expanding premixed flames, a critical stretch rate can also be identified but in this case the mechanism that causes the presence of a maximum/minimum burning rate depends on the competition between ignition transients and stretch by curvature. To illustrate, Figure 2-12 shows results from single-step chemistry numerical computations [3, 42] of a lean $H_2$/air mixture ignited by equilibrium adiabatic products. In these simulations, a spherical kernel of small radius $r_i$ filled with equilibrium adiabatic combustion products is set at $t = 0$ to simulate ignition and, subsequently, the time history of the consumption velocity $s_{c,P}$ is calculated. For this $Ma < 0$ flame, the maximum in consumption speed that is observed for each curve plotted in Figure 2-12 is generated by the competition between the initial quick rise of the burning rate from zero immediately after ignition and the decrease brought about by the reduction of flame curvature as the flame expand to larger radii. These numerical results also show that the

maximum consumption velocity is obtained when the ignition radius is equal to its critical value, $r_{cr}$, such that the initial kernel shrink if $r_i < r_{cr}$.

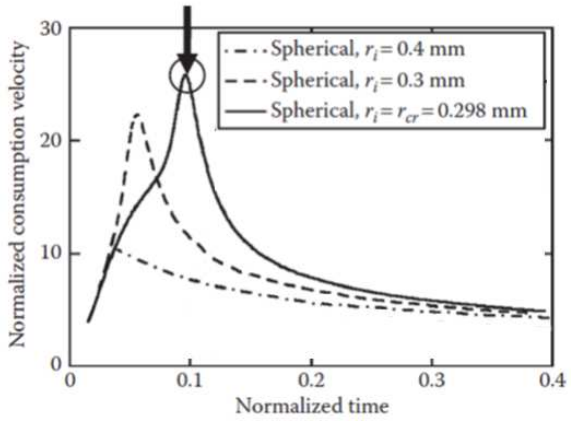


**Figure 2-12. Single step chemistry numerical simulation of normalized consumption speed $s_{c,P}/s_{L0}$ versus normalized time $ts_{L0}/\delta_{F0}$ for spherical expanding $H_2$/Air flames (with $\phi$ = 0.26, and reactants at standard temperature and pressure) ignited by pockets of adiabatic product gasses with initial radius $r_i$ [3, 42]. The maximum consumption speed for the spherical flame is indicated by an arrow and represents the critically stretched value.**

## 2.2 Turbulent premixed combustion modeling

As stated in Chapter 1, premixed turbulent combustion is characterized by the interaction of flames and turbulent flows over a wide range of length and time scales. A useful diagram to classify various burning modes resulting from the interaction of these different scales was first presented by Borghi in terms of the turbulence intensity normalized by unstretched laminar flame speed $u'/s_{L0}$, and the ratio of the integral length scale to the flame thickness $l_t/\delta_{T0}$ [68]. A slightly modified version of this diagram known as the Peters-Borghi diagram [57] is given in Figure 2-13. The boundaries between different regimes indicated in this figure should not be interpreted as

sharp and precise transitions between flame burning modes, but as an order of magnitude estimate of complex transitions which are likely to depend on a larger set of parameters.

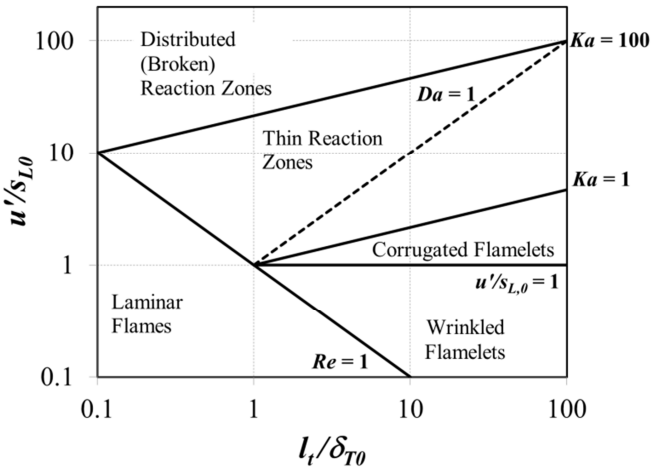


**Figure 2-13. Peters-Borghi diagram.** $Da = (l_t/\delta_{T0})/(u'/s_{L0})$ **is the Damköhler number,** $Re = (u'/s_{L0})(l_t/\delta_{T0})$ **is the Reynolds number and** $Ka = Re^{1/2}Da^{-1}$ **is the Karlovitz number.**

For this thesis, the primary region of interest is the "thin reaction zone", which is representative of the conditions at which many combustion system of practical interest operate [69] and most of the experiments described in Chapter 1 were performed. In this region the turbulent Kolmogorov eddy is smaller than the thickness of the preheat zone allowing it to enter the preheat zone and alter the diffusive processes while the laminar structure of the reaction zone tends to be preserved. This has been speculated to lead to flame thickening: this is yet to have been experimentally demonstrated conclusively [7], although some recent studies seem to indicate that this is actually possible [70-72]. In fact, the structure of the reaction zone is rather resistant to turbulent perturbations mostly because as the reactant gases get heated by chemical reactions (1) the viscosity increases (typically the dynamic viscosity of a gas is proportional to the square root of the

temperature) causing smaller eddies to be dissipated more quickly and (2) the size of turbulent eddies increases due to gas expansion. Furthermore, the high stretch rates associated with this regime cause the local flame structure response to flow perturbations to be highly nonlinear and can also lead to localized extinction events.

By contrast, in the region labeled as “wrinkled flamelets” and “corrugated flamelets” all the turbulent length scales of the flow are larger than the laminar flame thickness; as a result, the turbulence serves to wrinkle the flame front, while locally the flame preserves its laminar structure. In the “distributed reaction zone”, all the turbulent length scales are smaller than the laminar flame thickness and a propagating front is no longer recognizable.

The fact that in most situations of interest turbulent premixed flames are characterized by the presence of a front and that the length and time scales of turbulent flows are, to a certain extent, larger than those at which reactions occur is the basis of the so called “flamelet” concept [73]. This concept represents the classical paradigm utilized in turbulent premixed combustion modeling [74] and may be briefly characterized as follows. In premixed turbulent flames, chemical reactions that control heat release are confined to thin, wrinkled, convoluted and stretched reacting fronts that separate unburned reactants from burned products. Such fronts, commonly called “flamelets”, are typically assumed to have the same local structure as perturbed laminar flames. Then, the basic physical mechanisms of the influence of turbulence on combustion consist of

1. flame surface area production by turbulent stretching and wrinkling (an effect first highlighted by Damköhler [75]);

2. modification of local burning rates per unit front surface brought about by Lewis number/preferential diffusion effects and by small-scale turbulent eddies.

In particular, the latter mechanism has been utilized to explain the dependence of turbulent flame speed $s_T$ on fuel/oxidizer compositions as described in Chapter 1. This interpretation is justified by the fact that $s_T$ trend can generally be scaled with the stretch sensitivity of the mixture (e.g., the Markstein length) as verified by several investigators [76-78]. A key goal of modeling approaches based on this paradigm has been to scale the dependence of the surface area weighted burning rate upon turbulence intensity and scale size [79].

For example, the "flamelet library" method models these variations (1) by simulating the response of laminar flames to simple, well-defined stretching such as in planar counterflow flames (results of these simulations constitute the so-called 'flamelet library'), and (2) by averaging the library with a PDF (presumed or modeled by an additional transport equation) for the perturbations in a turbulent flow, as for example in recent RANS [80, 81] and LES [82, 83] studies.

Instead, other methods, such as "G-equation" [84] and "Flame Speed Closure" models [85], track the propagation of the average position of the turbulent flame front and capture the combined effects of flame wrinkling and local burning rates modifications using correlations for the turbulent flame speed $s_T$. An equation widely utilized in the combustion literature that relates the turbulent burning velocity to the flamelet structure is one that has been discussed by Bray and Cant [86]

$$s_T = s_{L0} I_0 A_T / A_L \tag{2.24}$$

where $A_T$ is the total area of the turbulent flame, $A_L$ is the area of the "unwrinkled" flame (usually taken as the area of the $\overline{c} = 0.5$ isocontour, see Figure 2-14) and $I_0$ is the so called "stretch factor", which is defined as the ratio between the averaged consumption speed along the turbulent flame $\overline{s_c}$ and unstretched laminar flame speed $s_{L0}$ ($I_0 = \overline{s_c} / s_{L0}$).

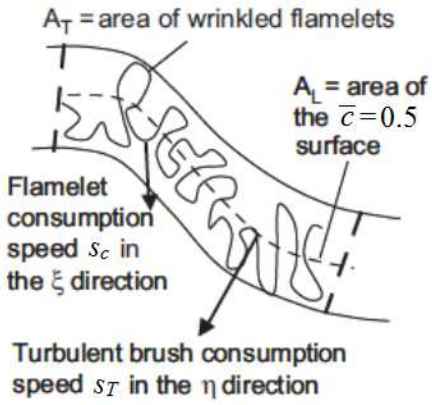


**Figure 2-14. Schematic illustrating the various terms in equation (2.24), adapted from Ref. [7]. $A_T$ represents the wrinkled area, while $A_L$ is the area of the $\overline{c} = 0.5$ contour. Also labeled are the flamelet consumption speed $s_c$ and the turbulent brush local consumption speed $s_T$.**

Finally, a transport equation for the flame surface or scalar dissipation rate [87] may be employed to model turbulent premixed flame propagation, but it is only very recently that studies on how to include the effect of preferential diffusion and non-unity Lewis number in this type of models have been undertaken.

The development of scaling laws describing stretch effects for the turbulent combustion modeling approaches described in this section is complicated by several factors. First, the nonlinear and unsteady phenomena described in Section 2.1.2 as well as the inherent complexity of turbulent flows make it difficult to parametrize the burning rates of the

large variety of structures present in a turbulent flame. In particular, the use of Markstein lengths, which describe the linearized flame response to small and steady flow perturbations, to correlate turbulent flame speed data does not seem entirely justified [4]. The abundance of phenomena occurring in a turbulent premixed flame substantially hampers the identifications of key physical factors for estimating the influence of fuel/oxidizer composition on flame propagation and structure. Second, Lewis number and preferential diffusion effects can create alternating zones of intense burning followed by extinction, making it difficult to clearly define a flame surface area: this is evident simply observing Figure 1-4 and Figure 1-5 or Figure 2-16 in the next section. Third, interaction between local burning rates and flame area wrinkling and stretching processes makes it difficult to study separately between these two effects i.e. $A_T$ and $I_0$ in equation (2.24) may be correlated and depend on each other [11].

Finally, it is worth mentioning that other modeling approaches not directly related to the "flamelet" paradigm have been proposed to model Lewis number and preferential diffusion effects in turbulent premixed flames, such as the "Conditional Moment Closure" (CMC) [88]. This approach, which is perhaps more useful to model flames close to the distributed reaction zone [74], is derived by methods utilized in turbulent non-premixed combustion modeling and focuses on modeling mixing rates rather than area production. The accuracy of this type of methods relies strongly on the quality of the micro-mixing model used, and the analysis of differential diffusion remains an open research question [89].

## 2.3 Lewis number and preferential diffusion effects: direct numerical simulations of turbulent premixed flames

Since part of this thesis work deals with analyses of a DNS database, in this section direct numerical simulations (DNS) studies of turbulent premixed flames are briefly reviewed. The focus of this review is on those studies that investigated Lewis number and preferential diffusion effects in turbulent flames; a list of the works that meet this criterion is provided in Table 1 at the end of this section. For this reason, in the discussion below we do not explicitly mention results from laminar flame-vortex interaction computational studies [62] and DNS of turbulent flames that focus on single-step chemistry with $Le = 1$ (like the recent DNS of Poludnenko and Oran [72, 90]) or complex chemistry but at equivalence ratios for which Lewis number and preferential diffusion are not leading order effects or are not discussed (like the recent DNS of a slot burner of Bell et al. [91] and of a low swirl burner of Day et al. [92]).

In general, DNS data of turbulent premixed flames in the thin reaction zone regime confirm that there exist correlations between local flame speed and flame strain/curvature consistent with the laminar flame theory presented in Section 2.1, but data in the literature are rather scattered (see section 5.2 in Ref. [4]). As an example, Figure 2-15 plots the local consumption speed $s_{c,P}$ computed from the 2D DNS of Chen and Im [93] against either flame curvature $K_C$, flame strain rate $K_S$ or stretch rate $\kappa$: in Figure 2-16 the isocontours of $H_2$ consumption rate utilized to calculate $s_{c,P}$ are shown to better understand the trends in Figure 2-15. As it can be observed from these figures, $s_{c,P}$ is positively correlated with $K_C$, $K_S$ and $\kappa$ as it is expected for a lean hydrogen/air flame

(for which $Ma_c < 0$). The correlation between $s_{c,P}$ and $K_C$ is also evident in Figure 2-16, where it is clearly shown that positively curved portions of the flame (convex toward the reactants) are characterized by higher consumption rates of hydrogen than negatively curved portions of the flame (convex toward the reactants). However, data in Figure 2-15 are rather scattered presumably because of nonlinear and unsteady effects described in Section 2.1.2, and a direct application of the results obtained from laminar flame theory is difficult.

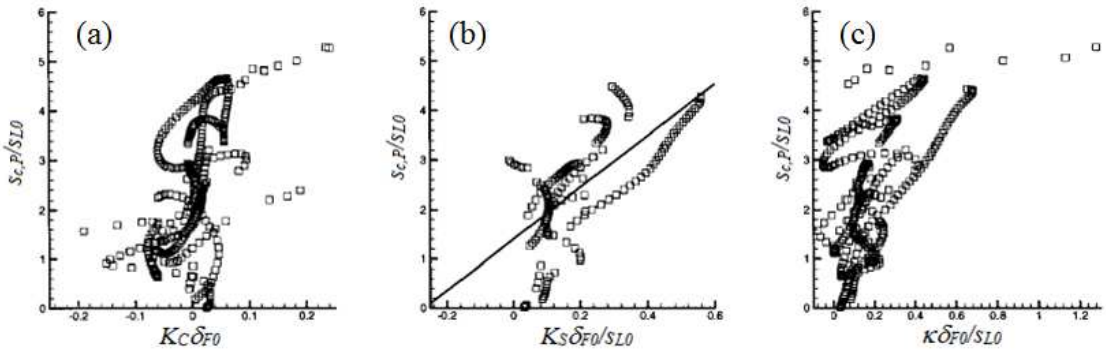


**Figure 2-15. Scatter plot of local consumption speed $s_{c,P}$ dependence on flame curvature $K_C$ (a) strain rate $K_S$ (conditioned on $K_C$ being smaller than 10% of its maximum value) (b) and stretch rate $\kappa$ (c) from the 2D DNS of Chen and Im [93] ($H_2$/air, $\phi$ = 0.4, $T^u$=300*K*, *p*=1*atm*, $s_{L0}$=22.4*cm/s*, $\delta_{T0}$ = 0.61*mm*, $\delta_{F0} = D_{O2}/s_{L0}$ = 0.1*mm*, $u'/s_{L0}$ = 5.0, $l_t/\delta_{T0}$ = 3.18).**

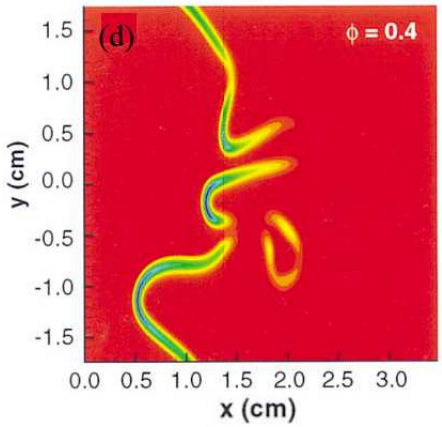


**Figure 2-16. Isocontours of $H_2$ consumption rate (red corresponds to zero consumption rate, blue corresponds to the maximum calculated consumption rate) from the DNS of Chen and Im [93], corresponding to the data shown in Figure 2-15. Reactants are on the left, products on the right.**

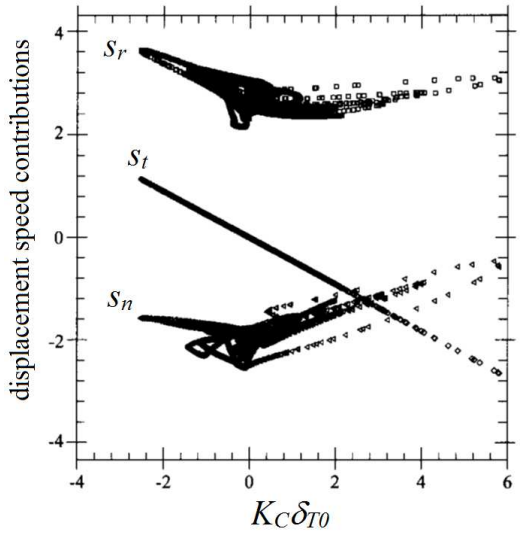


**Figure 2-17. Scatter plot of the three contributions (see equation (2.18)) to the displacement speed $s_d$ as a function of the curvature normalized by flame thickness $K_C\delta_{T0}$ for the lean $CH_4$/air flame of Ref. [94] ($\phi$ = 0.7, $T^u$ = 800$K$, $p$ = 1$atm$, $u'/s_{L0}$ = 10, $l_t/\delta_{T0}$ = 2.77, $\delta_{T0}$ = 0.31$mm$).**

Also trends in displacement speed $s_d$ obtained from DNS are qualitatively consistent with the theory of laminar flames but are generally even more difficult to reconcile

quantitatively with it [95], mostly because of the complications that arise in the definition of $s_d$ described in Section 2.1.1. Besides, DNS data show that $s_d$ trends are dominated by curvature effects, represented by the $s_t$ term in equation (2.18), especially in flames strongly wrinkled by turbulence [58]. To illustrate, Figure 2-17 presents a scatter plot of the different contributions to $s_d$ as a function of flame curvature $K_C$ for the lean methane/air flame of Ref. [94]: clearly the $s_t$ contribution displays the largest sensitivity to flame curvature and partially hides possible Lewis number and preferential diffusion effects influencing the reaction rate $s_r$ and normal gradient $s_n$ contributions to $s_d$. However, correlation between curvature and $s_r$ or $s_n$ is responsible for the different propagation characteristics of turbulent flames with different Lewis numbers [96].

More quantitatively, a few studies have also attempted to compare local flame speeds calculated in DNS of turbulent flames with laminar flame calculations. For example, Baum et al. [97] compared local heat release rates calculated in their $H_2$/Air flames database to calculations obtained from laminar planar counterflow twin flames at the same strain rate $K_S$: they reported that the laminar flame calculations did a poor job in predicting the structure of the turbulent flame, as shown in Figure 2-18a for one of the highest turbulence intensities they investigated. Hawkes and Chen [98, 99], instead, reported that for $CH_4$/air and $CH_4$/$H_2$/air flames the average displacement speed $s_d$ of flame elements with the same strain rate $K_S$ is well predicted by computations of laminar planar counterflow flames formed stagnating reactants against hot products. Finally, Sankaran et al. [100] showed that in their DNS of a $CH_4$/air slot burner the average structure of the reaction zone can be well represented by laminar planar counterflow twin

flames computations. A subset of their results is shown in Figure 2-18b, which compares averaged profiles of methane and hydroxyl radical production rate $\dot{\omega}$ (computed at different heights in the flame) to laminar computations at different strain rates.

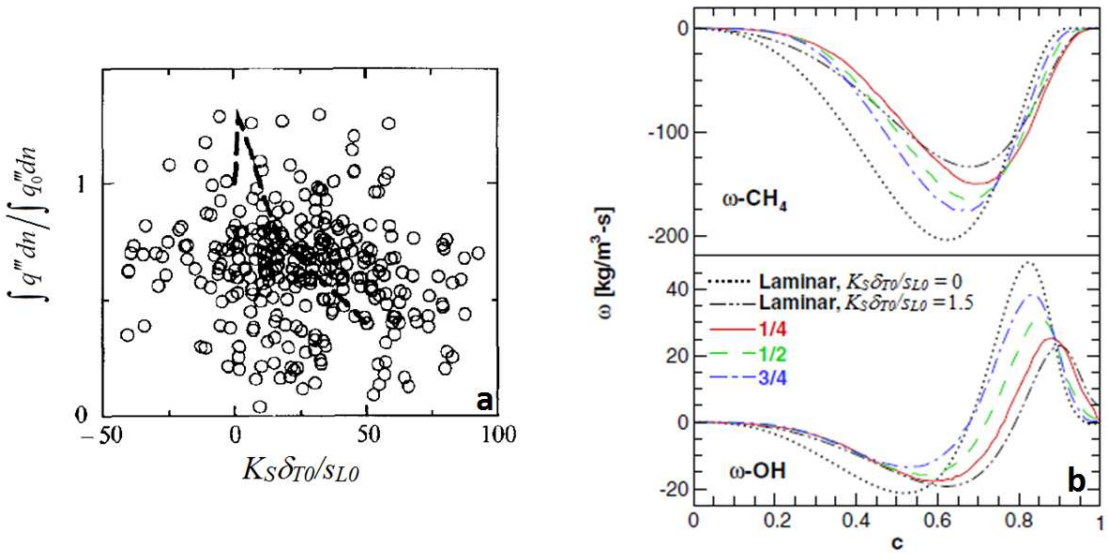


**Figure 2-18.**

**(a) Scatter plot of integrated heat release rate $q'''$ along vectors normal to the flame surface and strain rate $K_S$ for $H_2$/air, $\phi$= 0.5, $T^u$=300K, p=1atm,u'/$s_{L0}$=30.6, $l_t/\delta_{T0}$=1.26 [97]. Integrated heat release is normalized by the same quantity calculated for an unstretched planar flame $q_0'''$. The dashed line superimposed to the scatterplot represent values calculated in a laminar planar counterflow twin flame**

**(b) Rate of production of $CH_4$ and OH plotted against progress variable $c = \left(Y_{O_2} - Y_{O_2}^u\right)/\left(Y_{O_2}^b - Y_{O_2}^u\right)$ for $CH_4$/air flames at $\phi$= 0.7, $T^u$=800K, p=1atm. Colored lines refer to average profiles calculated in the turbulent slot burner of Sankaran et al. [100] at different heights (¼, ½ and ¾ of the total flame length).Dotted and dotted-dashed lines refer to values calculated in a laminar planar counterflow twin flame at two different strain rates $K_S$.**

To compare laminar and DNS results, flame strain rather than curvature has traditionally been utilized to parametrize burning rate variations. In fact, it is well known that the curvature PDFs of turbulent premixed flames are roughly symmetrical with respect to zero, while strain rate PDFs have non-zero positive mean [101]. Based on this

observation, it has been often assumed that zones of enhanced and diminished burning rate due to flame curvature cancel out in the mean, leaving only the influence of strain rates to explain Lewis number and preferential diffusion effects on the global consumption rate of turbulent flames [60, 99]. Neglecting curvature effects may have some justification for weakly wrinkled flames (such as in the wrinkled/corrugated flamelets regime) with $Le \sim 1$ and negligible preferential diffusion of species, but otherwise it does not seem an appropriate assumption [4]. First of all, nonlinearity and unsteadiness in the flame response (see Section 2.1.2) may prevent the effect of positively and negatively curved flames from canceling out, even in the mean.

Secondly, the mentioned PDFs of flame curvature and strain have been obtained for the whole turbulent flame brush, but different portion of the flame brush are characterized by different mechanisms of flame propagation [30, 96]. For example, at the leading edge of the turbulent flame brush more positively curved flame elements are present than at the trailing edge, by geometric necessity, and this implies that Lewis number and preferential diffusion effects act differently in different portion of the turbulent flame brush. This aspect is especially important for the leading point concept discussed in the next section.

Thirdly, inside the flame front $K_S$ and $K_C$ are not independent from each other, as pointed out while discussing equation (2.5). DNS studies [102-106] as well as experiments [35] show that near the reaction zone their correlation is negative, especially at low and moderate Damköhler numbers, and their correlation coefficient tend to become more negative with decreasing Lewis number. To illustrate, Figure 2-19 shows the joint PDFs of tangential strain rate $K_S$ and mean curvature $K_C$ for three turbulent

premixed flames with different Lewis number but propagating in the same turbulent flow field, as obtained from the single-step chemistry DNS of Ref. [105, 106].

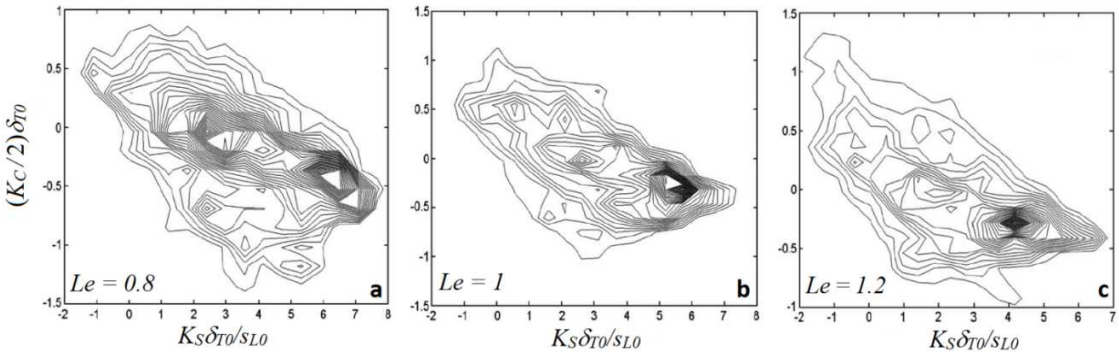


**Figure 2-19. Joint PDFs of tangential strain rate $K_S$ and mean curvature $K_C$ on the $c=\left(Y_D^u-Y_D\right)/\left(Y_D^u-Y_D^b\right)=0.8$ isosurface, where $Y_D$ is the mass fraction of the deficient reactant: (a) Le = 0.8; (b) Le = 1.0; (c) Le = 1.2. Single-step chemistry $u'/s_{L0}$=7.19, $l_t/\delta_{T0}$=1.92. Adapted from Ref. [105, 106].**

The explanation for this behavior is primarily due to defocusing (focusing) of heat in the positively (negatively) curved regions of the flame which gives rise to a lower (higher) value of dilatation $\nabla\cdot\vec{u}$ leading to smaller (larger) values of tangential strain rate $K_S=-\vec{n}\vec{n}:\nabla\vec{u}+\nabla\cdot\vec{u}$. This trend is demonstrated in Figure 2-20, which plots joint PDFs of dilation $\nabla\cdot\vec{u}$ and mean curvature $K_C$ for the same data shown in Figure 2-19. Note that the negative values of dilatation rate shown in Figure 2-20 at high values of $K_C$ are not a compressibility effect since all this flows are at low Mach number, but represent the effect of relative motions between fluid and *c*-isosurface [107]. In fact, according to the continuity equation the dilatation is equal to density change following the fluid element

$$\nabla\cdot\vec{u}=-\frac{1}{\rho}\frac{D\rho}{Dt}=\frac{1}{\rho}\left(\frac{\partial\rho}{\partial t}+\vec{u}\cdot\nabla\rho\right) \tag{2.25}$$

but this equation can also be expressed following a *c*-isosurface as

$$\nabla \cdot \vec{u} = -\frac{1}{\rho}\frac{D\rho}{Dt} = -\frac{1}{\rho}\left(\left(\frac{\partial \rho}{\partial t} + \underbrace{\left(\vec{u} - s_d \vec{n}\right)}_{=\vec{v}_F} \cdot \nabla \rho\right) + s_d \vec{n} \cdot \nabla \rho\right) = -\frac{1}{\rho}\left(\frac{D_c \rho}{Dt} + s_d \vec{n} \cdot \nabla \rho\right) \qquad (2.26)$$

where $s_d$ is the displacement speed of the *c*-isosurface (defined as in equation (2.17)) and $\vec{v}_F$ is the total speed at which the *c*-isosurface moves (defined as in equation (2.14)). For low Mach number flows and unity Lewis number flames $D_c\rho/Dt$ is equal to zero while the term $\vec{n} \cdot \nabla \rho$ is negative, since, generally, the density decreases moving toward the products. Then, the dilation can become negative in highly positively curved or highly strained portions of the flame where the displacement speed $s_d$ is negative (see Section 2.1.1). Lewis number and preferential diffusion of species can either hinder (if $Le < 1$ i.e. $Ma_c < 0$) or promote (if $Le > 1$ i.e. $Ma_c > 0$) the defocusing (focusing) of heat at positively (negatively) curved portions of the flame front. Thus, for $Le < 1$ the correlation between $\nabla \cdot \vec{u}$ and $K_C$ is weakened, while it is strengthened for $Le > 1$. This trend is recognizable in Figure 2-20, where for the same value of positive (negative) mean curvature, the $Le = 1.2$ flame achieves higher (lower) values of dilatation $\nabla \cdot \vec{u}$ than the $Le = 0.8$ flame.

Comparing Figure 2-20 and Figure 2-19 it can also be noticed that the joint PDF $K_S - K_C$ is more scattered than the joint PDF $\nabla \cdot \vec{u} - K_C$ especially at negative curvatures. This can be explained by investigating the term $-\vec{n}\vec{n} : \nabla \vec{u}$ which can be rewritten as:

$$-\vec{n}\vec{n}:\nabla\vec{u} = -\vec{n}\cdot\underline{\underline{S}}\cdot\vec{n} = -\left(\alpha_1\psi_1^2 + \alpha_2\psi_2^2 + \alpha_3\psi_3^2\right) \tag{2.27}$$

where $\underline{\underline{S}} = 1/2\left(\nabla\vec{u} + (\nabla\vec{u})^T\right)$ is the strain rate tensor, $\alpha_1 \geq \alpha_2 \geq \alpha_3$ are its eigenvalues and $\psi_i = \vec{n}\cdot\vec{e}_i$ is equal to the cosine of the angle formed by the normal to the flame surface and the eigenvector $\vec{e}_i$ associated to the eigenvalue $\alpha_i$. Equation (2.27) shows that the term $-\vec{n}\vec{n}:\nabla\vec{u}$ depends on the alignment between the strain rate tensor and the flame surface. Turbulent fluctuations of this alignment are responsible for weakening the correlation $K_S - K_C$ relative to the correlation $\nabla\cdot\vec{u} - K_C$. Besides, in regions where the dilation $\nabla\cdot\vec{u}$ is high (such as at negative $K_C$) it has been shown [108] that the flame normal tends to align with the most extensive strain rate (i.e. $\psi_1^2 \sim 1$) thereby decreasing $K_S$ contrary to the increasing trend brought about by $\nabla\cdot\vec{u}$.

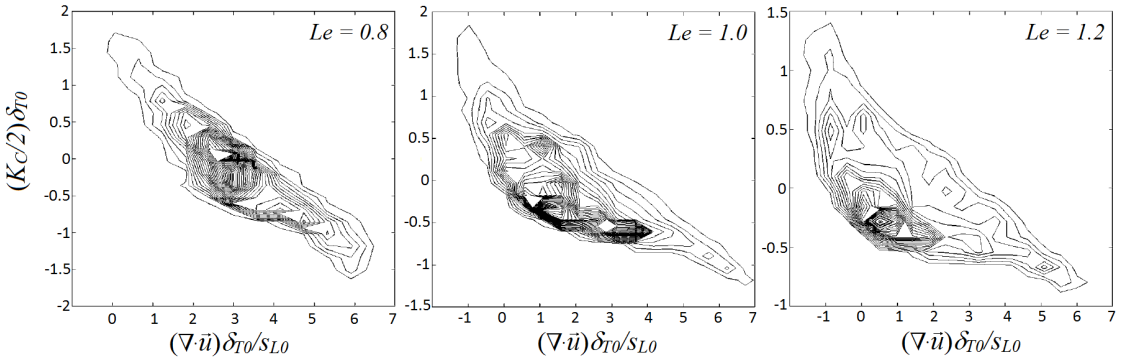


**Figure 2-20. Joint PDFs of dilation $\nabla\cdot\vec{u}$ and mean curvature $K_C$ on the same isosurface as Figure 2-19 for different Lewis numbers. Adapted from Ref. [105].**

Finally, contrary to the trends shown in Figure 2-19 and Figure 2-20, it should be noted that DNS studies of turbulent premixed flames without heat release did not find any

correlation between tangential strain rate and curvature [109] while DNS studies of surfaces propagating at constant speed in constant density turbulent flows found that highly curved shapes (both negatively and positively curved) are probable only in regions of almost zero strain rate [110]. The relative importance of the effects brought about by dilatation relative to turbulence straining can be scaled as [108]:

$$\frac{\nabla \cdot \vec{u}}{K_S} \sim \left( \frac{\rho^u}{\rho^b} \right) f\left(Le\right) \frac{l_t s_{L0}}{u' \delta_{T0}} = \left( \frac{\rho^u}{\rho^b} \right) f\left(Le\right) Da \tag{2.28}$$

where $f\left(Le\right)$ is a function which increases with decreasing $Le$. Equation (2.28) shows that the contribution of heat release effects to strain rates cannot be neglected for flames with high gas expansion ratio $\rho^u / \rho^b$, high Damköhler numbers and low Lewis numbers. The negative correlation of strain and curvature implies that $K_S$ and $K_C$ affect the local flame front structure in two opposite directions [4]. A noticeable consequence of these conflicting effects is that in the thin reaction zone regime the local flame thickness does not depend monotonically on curvature and both negatively and positively curved flamelets tend to be thicker than unstrained laminar flamelets [100, 107]. This phenomenon is illustrated in Figure 2-21, which shows the joint PDFs of progress variable gradient $\left|\nabla c\right|$ and mean curvature $K_C$ for the same flames of Figure 2-19 and Figure 2-20. The progress variable gradient $\left|\nabla c\right|$ is inversely proportional to the local flame thickness i.e. an high value of $\left|\nabla c\right|$ implies a thin flame ($\delta \sim 1/\left|\nabla c\right|$). For $Le = 1$ two branches in the joint PDF can be observed: low values of $\left|\nabla c\right|$ (i.e. thick flames) are

associated with high values of $K_C$, both positive and negative. For non-unity Lewis number the non-monotonic dependence of $|\nabla c|$ on $K_C$ is somewhat suppressed since for $Le = 0.8$, the flamelet thickening for $K_C > 0$ and vice versa for $Le = 1.2$.

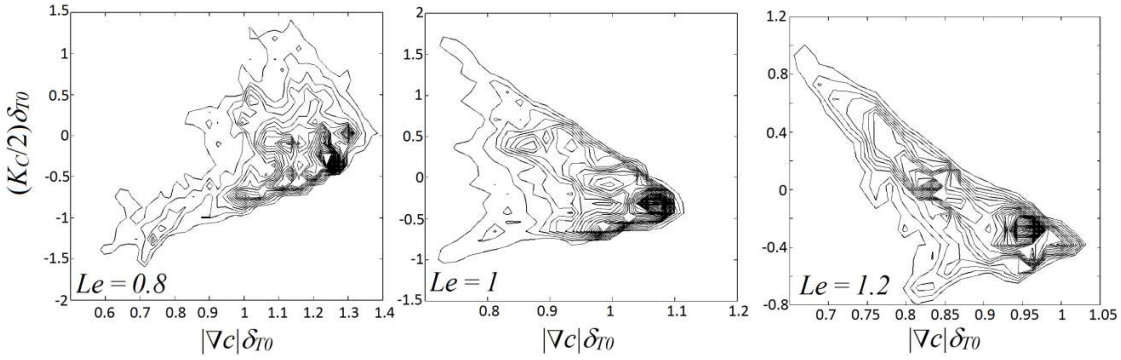


**Figure 2-21. Joint PDFs of mean curvature $K_C$ and magnitude of the progress variable *c* gradient $|\nabla c|$ on the same isosurface as Figure 2-19 for different Lewis numbers. Adapted from Ref. [106].**

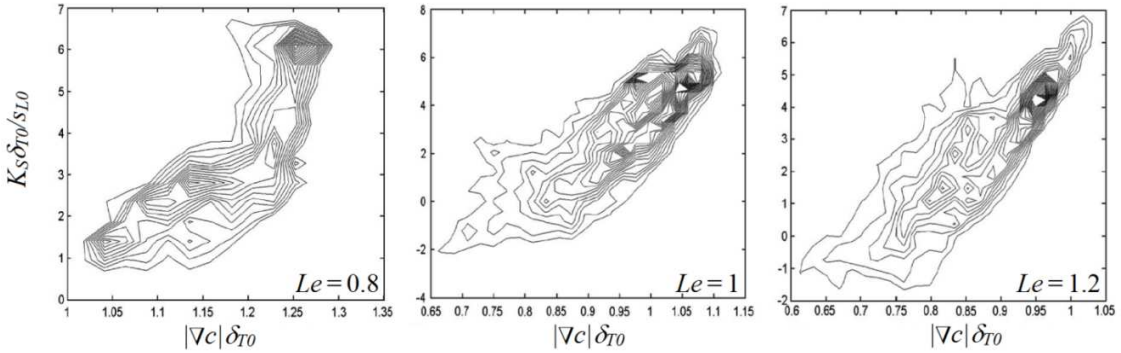


**Figure 2-22. Joint PDFs of tangential strain rate $K_S$ and magnitude of the progress variable *c* gradient $|\nabla c|$ on the same isosurface as Figure 2-19 for different Lewis numbers. Adapted from Ref. [106].**

This non-monothonic dependence of flame thickness on curvature is also to the fact that $|\nabla c|$ tend to correlate strongly with strain rate $K_S$ as shown in Figure 2-22 [106]. A more

precise explanations of these trends, requires the study of a transport equation for the progress variable gradient $|\nabla c|$, as described in Ref. [107].

Finally, DNS studies indicate that the most probable local flame geometry is cylindrical and the most highly curved regions on the flame surface correspond to cylindrical shapes, while the probability of finding spherically curved flame fronts is low especially at high turbulent intensities [28, 59]. This indicates that a two-dimensional description of turbulent flame fronts geometry is acceptable in first approximation and partially justifies the use of 2D direct numerical simulations to study turbulent flames (see Table 1). In Chapter 3 this observation is utilized to justify a comparison between cylindrical laminar flames and statistics obtained from DNS of turbulent flames.

In summary, nonlinearity and unsteadiness in the flame response, the different response of the flame to strain and curvature as well as the different behavior of the flame at different positions in the turbulent flame bush make it difficult to apply the quasi-steady flamelet paradigm described in Section 2.2. This consideration is especially valid for lean hydrogen turbulent flames for which these effects are particularly important as will shown in Chapter 3.

**Table 1. Methods and conditions of DNS of turbulent premixed flames associated with Lewis number and preferential diffusion effects.**

| Reference | Dimension | Chemistry | Mixture | Density | Transport Properties | Turbulence |
|---|---|---|---|---|---|---|
| Ashurst et al. [111] | 2D | Single-step | Le = 0.5, 2.0 | Constant | Constant | Random flow field, $l_t/\delta_{T0}$=10 |
| Haworth and Poinsot [102] | 2D | Single-step | Le = 0.8, 1.0, 1.2 | Variable | Temperature dependent | Decaying, $u'/s_{L0}$ = 5.8-6.6, $l_t/\delta_{T0}$=3.6-4.3 |
| Rutland and Trouve' [59] | 3D | Single-step | Le = 0.8, 1.0, 1.2 | Constant | Constant | Decaying, $u'/s_{L0}$ = 3-5, $l_t/\delta_{T0}$~1 |
| Baum et al. [97]; Swaminathan and Bilger [88, 112] | 2D | Complex | $H_2/O_2/N_2$,$T^u$ =298K or 700K, $\phi$ = 0.35-1.3 | Variable | Mixture averaged [113] | Decaying, $u'/s_{L0}$ = 1.2-3.2 and 31, $l_t/\delta_{T0}$~1.26-4.34 |
| Trouve' and Poinsot [30] | 3D | Single-step | Le = 0.3, 0.8, 1.0, 1.2 | Variable | Temperature dependent | Decaying, $u'/s_{L0}$ = 10, $l_t/\delta_{T0}$~1 |
| Echekki and Chen et al. [31, 94, 114-117] | 2D | Complex | $CH_4$/Air, $\phi$= 0.7 and 1, $T^u$ =800K | Variable | Temperature dependent | Decaying, $u'/s_{L0}$ = 4-10, $l_t/\delta_{T0}$~2.7-10 |
| Chen and Im [93, 118] | 2D | Complex | $H_2$/Air, $\phi$ = 0.4, 0.6, 2.0 and 6.5, $T^u$ = 300K | Variable | Temperature dependent | Decaying, $u'/s_{L0}$=5 and 10, $l_t/\delta_{T0}$~2.3-4.1 |
| Hawkes and Chen [98, 99], Chakraborty et al. [119] | 2D | Complex | $H_2$/Air, $\phi$ = 0.6, $CH_4$/Air, $\phi$ = 0.52 and $CH_4/H_2$ mixtures, $T^u$ = 300K | Variable | Temperature dependent | Decaying, $u'/s_{L0}$=9.5-28.5 ($CH_4$/air) $u'/s_{L0}$=3-30 ($H_2$/air) $l_t/\delta_{T0}$~0.28-10 |
| de Charentenay and Ern [120] | 2D | Complex | $H_2$/Air, $\phi$ = 0.5, 1.0 and 5.0, $T^u$ = 300K and 800K | Variable | Multicomponent and thermal diffusion | Decaying, $u'/s_{L0}$=1-10 $l_t/\delta_{T0}$~2-9 |
| Tanhashi et al. [121, 122] | 3D | Complex | $H_2$/Air, $\phi$ = 1.0, $T^u$ = 700K | Variable | Mixture averaged [113] | Decaying, $u'/s_{L0}$=0.85-3.41 $l_t/\delta_{T0}$~0.85-3.38 |
| Shim et al. [123, 124] | 3D | Complex | $H_2$/Air, $\phi$ = 0.6 and 1.0, $T^u$ = 700K | Variable | Mixture averaged [113] | Decaying, $u'/s_{L0}$=0.85-7 $l_t/\delta_{T0}$~20-170 |
| Chakraborty and Cant [96, 105, 106, 108, 125-127] | 3D | Single-step | Le = 0.34, 0.6, 0.8, 1.0, 1.2 | Variable | Constant | Decaying, $u'/s_{L0}$=7.5 $l_t/\delta_{T0}$~2.45 |
| Han and Huh [128] | 3D | Single-step | Le = 0.6, 0.8, 1.0, 1.2 | Variable | Temperature dependent | Decaying, $u'/s_{L0}$=6-10 $l_t/\delta_{T0}$~2.5-3.2 |
| Bell, Day et al. [16, 129] | 2D | Complex | $C_3H_8$/Air at $\phi$ = 0.7, $CH_4$/Air at $\phi$ = 0.8 and $H_2$/Air at $\phi$ = 0.37, $CH_4/H_2$ mixtures $T^u$ = 300K | Variable | Mixture averaged [113] | Decaying, $u'/s_{L0}$~1 $l_t/\delta_{T0}$~5 |
| Day et al. [28] | 3D | Complex | $H_2$/Air at $\phi$ = 0.37, $T^u$ = 298K | Variable | Mixture averaged [113] | Decaying, $u'/s_{L0}$~0-2.8 $l_t/\delta_{T0}$~3.75 |
| Aspden, Day and Bell [71, 130, 131] | 3D | Complex | $H_2$/Air at $\phi$ = 0.31-0.4, $CH_4$/Air $\phi$ = 0.7, $C_3H_8$/Air $\phi$ = 0.7, $T^u$ = 298K | Variable | Mixture averaged [113] | Artificially forced, $u'/s_{L0}$~0-150 $l_t/\delta_{T0}$~0.5-1 |
| Hawkes et al. [132, 133] | 3D | Complex | $H_2$/Air at $\phi$ = 0.7, $T^u$ = 700K | Variable | Mixture averaged [113] | Forced by mean shear, $u'/s_{L0}$~1-10 $l_t/\delta_{T0}$~1-10 |
| Sankaran et al. [100] | 3D | Complex | $CH_4$/Air at $\phi$ = 0.8, $T^u$ = 800K | Variable | Mixture averaged [113] | Slot burner, $u'/s_{L0}$~2-3 $l_t/\delta_{T0}$~0.8-1.2 |

## 2.4 Leading points concept

An approach alternative to the “flamelet” paradigm is based upon so-called “leading points”, which are intrinsically *local* properties of the turbulent flame. This concept was originally proposed by Zeldovich [134], who described the "leading/pilot" points as the most forward-lying points of the flame front in the direction of the reactants. This idea was subsequently expanded [4, 61]. In a turbulent premixed flame, the largest velocity fluctuations in the direction of propagation create convex bulges with respect to the reactants which generate flame surface area behind them and determine the average combustion velocity. Thus, leading points are loosely defined as positively curved points on the turbulent flame front that propagate out furthest into the reactants in spatial regions where turbulent eddies induce low approach flow velocities. Within this interpretation, *augmentation of flame surface area is the effect of increased burning rates, not the fundamental cause*. As stated in Ref. [134] (pp. 447-448) for flames propagating in horizontal tubes:

*“The pilot point in a non-stationary flame is the most forward-lying point of the flame front in the direction of combustion propagation. The igniting “impulse” is transmitted from it to adjacent portions of the flame, and so on, until the flame front encompasses the entire mixture volume…* [pilot points] *establish the relationship between an integral characteristic of the process (the surface area of the flame) and a local quantity (the maximum velocity of the gas along the tube).”*

In the leading point concept framework it is postulated that modifications in the overall turbulent combustion speed brought about by Lewis number and preferential diffusion

effects depend solely on modification of the burning rate at the leading points since an increase (decrease) in the average propagation speed of these points causes more (less) flame area to be produced behind them. Thus, such a concept offers the opportunity to substantially simplify the modeling of turbulent premixed flames by reducing the "flamelet library" (a collection of basic characteristics of perturbed laminar flames that allow for all possible type of perturbations) to a single "flamelet page" describing the burning rate of the leading point. In other words, modeling of turbulent burning rates by leading points concept can be thought as consisting of two sub-problems: (1) modeling the burning rates at the leading points and (2) modeling the dynamics/statistics of the leading points in the turbulent flame. Studies that attempted to answer to these two questions are summarized in the next two sections.

### 2.4.1 Leading points burning rates

Several investigators have assumed that the structure of leading points can be well represented by quasi-steady "critically" stretched laminar flames in canonical configurations such as, stationary curved flame ball [135, 136], expanding spherical flames of small radius [42, 137] and planar counterflow twin flames near extinction [9-11, 61]. The idea behind this use of critically stretched laminar flames comes from the following proposed mechanism for the formation of leading points: a flame element can become a leading point if transported toward the reactants by a strong turbulent eddy (especially if $u' \gg s_{L0}$) but its propagation is limited by local extinction; then, at the leading point a local balance between convection and quenching is established similar to that of critically stretched (i.e. under near-extinction conditions) laminar flames. Other

investigators, instead, have simply utilized empirical formulae based on some "effective" Lewis number of the mixture to model leading points burning rates [138-140].

In the literature, testing of these proposed leading points burning rates models has been performed "*a posteriori*", i.e. based on their ability to develop correlations for turbulent flame speed data. For instance, Venkateswaran et al. [9-11] computed the maximum displacement speed $s_{L,max}$ in a twin planar counterflow flame, as shown in Figure 2-23a, and used this quantity to correlate their database of $H_2$/CO/air turbulent flames, which was presented in Figure 1-1. As can be observed from Figure 2-23b, scaling the turbulent flame speed data with $s_{L,max}$ rather than with the unstretched laminar flame speed $s_{L0}$, collapses the measurements on a single curve rather well. This is remarkable, given the fact that in this database the turbulent flame speeds $s_T$ of different mixtures at the same turbulent intensity can display up to a 200% difference.

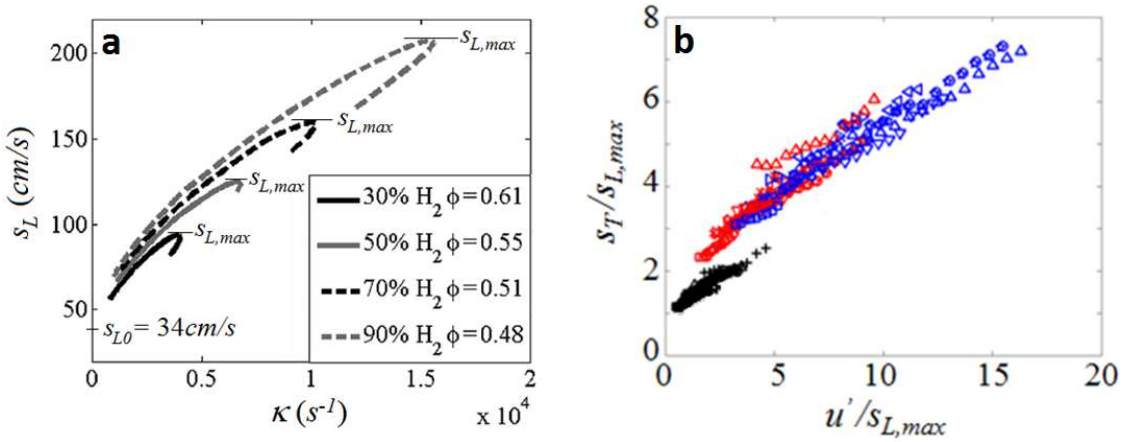


**Figure 2-23. (a) Dependence of laminar flame speed $s_L$ on stretch $\kappa$ as computed in counterflow twin flames for the different $H_2$/CO/air mixtures of Venkatewaran et al. [11]. (b) Same turbulent flame speed data shown in Figure 1-1 [11] but normalized by the $s_{L,max}$ values shown in Figure 2-23a instead of $s_{L,0}$.**

For completeness, we also mention that the phenomenon of rapid flame propagation along the axis of vortex tubes has been taken into consideration as a possible model for the burning rate of leading points [4]. This idea has not seen much development for the modeling of Lewis number and preferential diffusion effects but several turbulent combustion models have focused on this flame propagation mechanism [64]. The possible role of vortex tubes in the formation of leading points will be explored further in Section 3.6 and Chapter 5.

### 2.4.2 Dynamical significance of leading points

Few results addressing the problem of modeling leading point dynamics and statistics in turbulent flames are available in the literature, mainly because the basic leading point argument itself is somewhat phenomenological and remains to be put on firm theoretical footing. However, there are two instances where the leading points concept can be clearly proved.

The first instance regards the application of the Kolmogorov-Petrovskii-Piskunov (KPP) theorem to a statistically stationary, one-dimensional turbulent flame (see Appendix A in Ref. [6] and Ref. [141]). For this geometrical configuration (schematically shown in Figure 2-24a), the balance equation for a Favre' averaged progress variable can be written as

$$\underbrace{\rho^{u} s_T \frac{\partial \tilde{c}}{\partial x}}_{\substack{propagation/\\ convection}} = \underbrace{\frac{\partial}{\partial x}\left( \bar{\rho} D_T \frac{\partial \tilde{c}}{\partial x} \right)}_{turbulent\,diffusion} + \underbrace{\bar{\rho}\tilde{\dot{\omega}}}_{reaction} \tag{2.29}$$

where $\rho^u$ is the unburned gas density, "$\bar{}$" refers to ensemble averaged quantities, "~" refers to Favre' averaged quantities (i.e. density weighted ensemble averaged $\tilde{c} = \overline{\rho c}/\bar{\rho}$), $\tilde{\dot{\omega}}$ is the Favre' averaged reaction rate and $D_T$ represents the turbulent diffusivity (which may be variable and depend on $\tilde{c}$). Equation (2.29) under the assumptions

1) $D_T > 0$ (gradient turbulent transport)

2) $\bar{\rho}\tilde{\dot{\omega}} > 0$

3) $\left.\frac{\partial}{\partial \tilde{c}}\left(\bar{\rho}^2 D_T \tilde{\dot{\omega}}\right)\right|_{\tilde{c}=0} > 0$ and $\left.\frac{\partial}{\partial \tilde{c}}\left(\bar{\rho}^2 D_T \tilde{\dot{\omega}}\right)\right|_{\tilde{c}=0} = \max\left(\frac{\partial}{\partial \tilde{c}}\left(\bar{\rho}^2 D_T \tilde{\dot{\omega}}\right)\right)$

admits a class of solutions known as "pulled fronts" for which the propagation speed $s_T$ is controlled by the leading edge of the turbulent flame brush ($\tilde{c} = 0$):

$$s_T = \frac{2}{\rho_u}\sqrt{\left.\frac{\partial}{\partial \tilde{c}}\left(\bar{\rho}^2 D_T \tilde{\dot{\omega}}\right)\right|_{\tilde{c}=0}} \tag{2.30}$$

Assumptions 1)-3) are satisfied by several turbulent premixed combustion RANS closure models, and it is customary to utilize the KPP theorem to obtain estimates of turbulent flame speed [142]. Within this framework, the "leading points" controlling the turbulent flame propagation are defined as those points where $\tilde{c} \to 0$; we will refer to this point/surface as the "flame brush leading point" in this thesis work.

Despite being rather straightforward, this characterization of the leading points suffers of several drawbacks. First, the validity of assumptions 1)-3) has not yet been proven for

turbulent premixed flames even though many closure models satisfy these restrictions. Second, a perfectly statistically stationary one-dimensional turbulent flame is not realizable experimentally because this configuration is intrinsically unstable. Turbulent flames that approximate these conditions can be realized in slightly divergent or slowly swirling flows, such as in low-swirl burners (LSB). As an example, Figure 2-24 reproduces an image from the low-swirl-burner (LSB) of Marshall *et al.* [143]. Nonetheless, most turbulent flame brushes develop from attachment points that constrain flame motions and impede turbulence from fully wrinkling the flame in their vicinity: predictions inferred from statistically stationary one dimensional flames are often not appropriate in these conditions [144, 145], and it is not clear how to identify leading points for these situations.

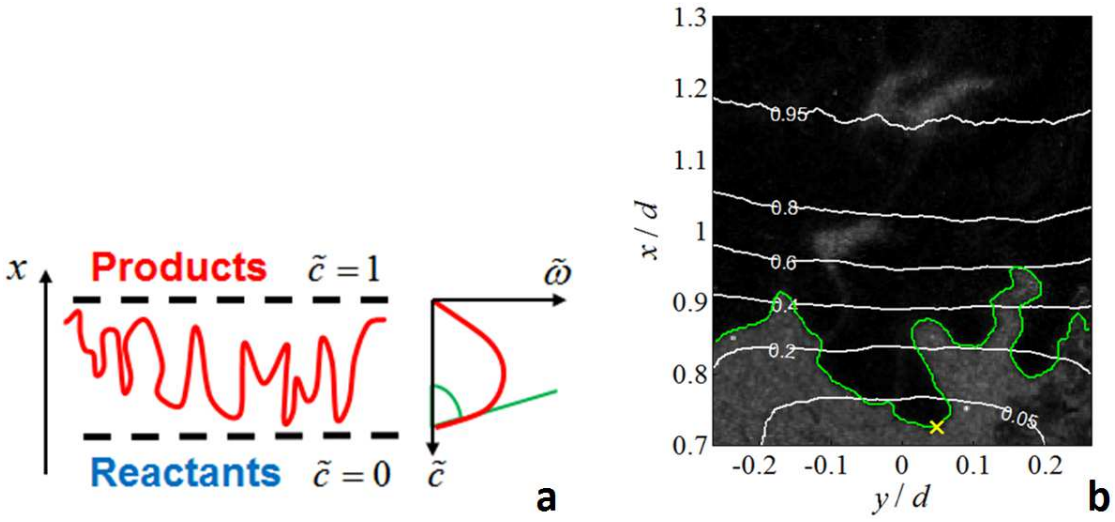


**Figure 2-24. (a) Schematic of a statically one dimensional stationary turbulent flame (b) Mie scattering image from LSB burner of Marshall et al. [143] (d = 36mm, 50/50 $H_2$/CO, 0.55 equivalence ratio, STP conditions). Reactants are flowing from below. Flame edge (green), instantaneous leading point (yellow x) and average progress variable, $\overline{c}$ , (white), are overlaid onto the raw image.**

Third, experimental or numerical study of the leading edge characteristics of a turbulent flame brush is problematic because of difficulty in gathering enough data to develop meaningful statistic; indeed, the $\tilde{c} = 0$ point in any real data set of finite size lies at the point where a single realization of the flame occurs. Note also that within the KPP interpretation, the flame does not possess leading points for the majority of time instants, as the point on the flame that instantaneously lies farthest into the reactants may occur over a range of $\tilde{c}$ values. This makes it difficult to clearly identify the physical mechanism through which leading points influence the overall flame propagation. We will refer to these points as "instantaneous leading points", indicated by the yellow "x" in Figure 2-24, where the instantaneous flame front is overlaid on top of time averaged progress variable contours. For the turbulent flames analyzed by Marshal et al. [143], for 90% of the flame realizations the position of the "instantaneous leading points" occurs over the $0.02 < \tilde{c} < 0.66$ range, with an average location at $\tilde{c} \cong 0.24 - 0.30$, depending on turbulence intensity and fuel composition.

The second example that clearly shows the significance of the leading points in uniquely controlling the burning velocity is shown in Figure 2-25a, following Ref. [11]. This figure illustrates an initially flat flame propagating in a spatially varying, but temporally steady, flow field in which the velocity isocontours are parallel to the direction of flame propagation. If the laminar burning velocity, $s_L$, is constant, then it is seen that the portion of the flame at the lowest velocity point, point "B" in the figure, propagates out the fastest. In the lab-fixed coordinate system, the flame at Point B moves at a speed of $s_L + (\Delta u)_{LP}$, where the subscript "*LP*" denotes the leading point. Moreover, it can easily be shown that, after an initial transient, the entire front reaches a stationary shape and

propagation speed with the value $s_L + (\Delta u)_{LP}$ as shown in Figure 2-25b. As such, the front displacement speed is controlled by the leading points of the flame that propagate into the lowest approach flow velocity regions ahead of the flame. This example clearly illustrates that the resulting increase in flame area induced by the spatially varying velocity field is the *effect* of the higher displacement speed, not the *cause*. Finally, note that in this steady state example, the "flame brush leading point" and "instantaneous leading point" coincide.

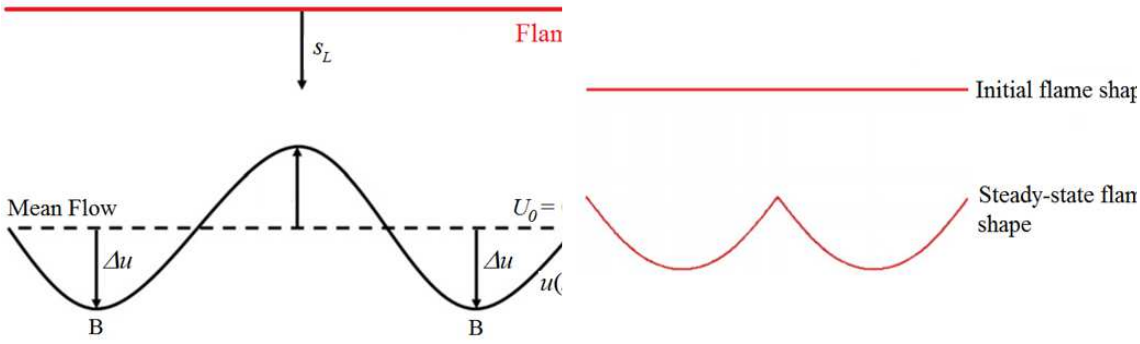


(a) (b)

**Figure 2-25. Model problem of an initially flat flame propagating into a spatially varying flow field (a); level set computation of the model problem, where the initial and final steady-state flame shapes are shown (b) [11].**

More generally, if the unidirectional periodic velocity field is given by $u(x) = f(x)$, then it can be shown that the burning velocity at large times is given by $s_L + \max(-f(x))$ (proved in Appendix C). In other words, *the burning velocity is controlled by conditions at a discrete spatial point* or points and is independent of the initial conditions and the details of the flow field, such as the scale size of the velocity inhomogeneities. This latter model problem becomes more complicated if the flow is

unsteady or three dimensional. In this case, the spatial position of the leading point may evolve in time: following the terminology of Ref. [9, 10], the leading point may no longer be “quasi-steady”, and it is unclear how to apply leading points argument in this case, or if this approach is even valid. This thesis work takes up this problem in detail in order to examine the dynamical significance of leading points, as described in Chapter 4.

# CHAPTER 3
# LEADING POINTS BURNING RATES

Given the background provided in Chapter 2, it follows that information about the structure of the flame front (especially near the turbulent flame brush leading edge) is needed to critically evaluate ideas put forward by leading points concepts and, more generally, to improve models for the turbulent flame propagation of negative Markstein length flames. In particular, this chapter analyzes leading points burning rates by investigating:

1) local flame front characteristics (flame speed, flame thickness, curvature and strain) of turbulent premixed flames
2) how these flame front characteristics compare to model laminar flame calculations and to "critically" stretched laminar flames
3) how this comparison changes for those portion of the flame front located near the leading edge of the turbulent flame brush.

To achieve these objectives, this chapter analyzes a set of direct numerical simulations (DNS) of highly stretch sensitive flames, described by Aspden et al. [71]. These simulations consider very lean $H_2$/air flames ($\phi = 0.31$) at moderate and extremely high turbulent intensities. In these conditions, the effects of non-unity Lewis number and preferential diffusion of species (Section 2.1) are the dominant factors influencing the overall flame structure and propagation characteristics: as a consequence, these simulations represent a good testing ground for leading point concepts.

In order to interpret the statistical information obtained by the DNS database, we calculate reference, one-dimensional computations of stretched premixed flames in several geometrical configurations shown in Figure 3-1: a planar counterflow twin flame (PCF), a tubular counterflow flame [40] (TCF) and an expanding cylindrical flame (ECF) ignited from a pocket of burnt gases. These different geometries are useful to isolate various nonlinear and unsteady effects (see Section 2.1.2) and allow for a comparison of flame response to stretch rates that are imposed through both hydrodynamic stretch and flame curvature. Results for a few other flame geometries (tubular flames with an inner wall and spherical flames) related to those shown in Figure 3-1 are presented in Appendix A.3.

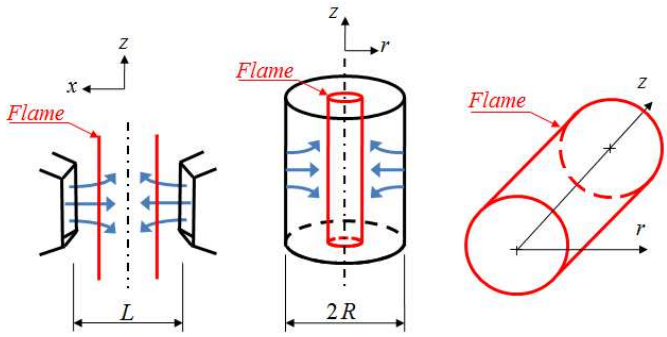


**Figure 3-1. Premixed flame geometrical configurations utilized in this study as model problems to investigate strongly stretched flames: planar counterflow twin flame (PCF, left), tubular counterflow flame (TCF, center), expanding cylindrical flame (ECF, right).**

The rest of the chapter is organized as follows. Section 3.1 briefly overviews the conditions and numerical methods used to compute the three model geometries of Figure 3-1 as well as the characteristics of the turbulent flames computed by the DNS. Section 3.2 details the definitions of local burning rate, flame thickness, curvature and flame

strain used in this thesis to investigate the structure of the turbulent flame front and compare it to the 1D laminar computations. Furthermore, the procedure utilized to identify the leading edge of the turbulent flame brush is described. Results from the model laminar flame computations are outlined in Section 3.3. Analysis of the DNS database is then presented in Section 3.4 for the entire flame front and in Section 3.5 for the portion of the flame front at the leading edge. Finally, in Section 3.6 the chapter concludes with a critical appraisal of the results obtained.

## 3.1 Numerical procedures

All the numerical simulations considered in this chapter utilize the transport coefficients, thermodynamics properties and chemical kinetics of the $H_2/O_2$ system of the GRI 2.11 mechanism [146] and a mixture averaged formulation [113] to model molecular diffusion. We consider an $H_2$/air flame at an equivalence ratio of $\phi$ = 0.31 and with an initial reactants temperature $T^u = 298K$ and at pressure $p = 1atm$. For these conditions, a PREMIX [147] calculation shows that the unstretched laminar flame speed is $s_{L0} = 4.68cm/s$ while the flame thickness computed from the maximum value of the temperature gradient is $\delta_{T0} = \left(T^{b,0} - T^u\right) \Big/ \left(dT/dx\right)_{max} = 1.9mm$, where $T^{b,0} = 1212K$ is the adiabatic flame temperature, and the full width at half maximum (FWHM) of the $H_2$ consumption rate $\dot{\omega}_{H_2}$ profile is $\delta_{H2,0} = 0.67mm$.

First, we briefly describe the computational approaches used to model the three flame geometries shown in Figure 3-1; further details and convergence studies are presented in

Appendix A.1. The PCF was simulated utilizing the standard OPPDIF code with an arc-length continuation technique to capture the extinction point as implemented in CHEMKIN-PRO© [147]. For the TCF configuration, a modified version of the OPPDIF code adapted for the cylindrical geometry [40] was used. The half jets distance $L/2$ for the PCF and the external radius *R* of entrance of the fresh gases for the TCF, were both chosen equal to $10cm$, to ensure that the outer boundary conditions do not affect the flame structure at low strain.

The ECF was simulated with an isobaric, one dimensional formulation of the conservation equations in cylindrical coordinates. The continuity, thermal energy and species equations were discretized and solved with the finite element method, as implemented in the commercial software COMSOL© [148]. The initial conditions ($t = 0$) imposed for temperature $T$, species mass fractions $Y_i$ and gas velocity $u$ are

$$T(r,t=0)=\begin{cases}T^{b,0},\ 0\le r<R_i\\ T^{u},\ R_i\le r<\infty\end{cases}\qquad Y_i(r,t=0)=\begin{cases}Y_i^{b,0},\ 0\le r<R_i\\ Y_i^{u},\ R_i\le r<\infty\end{cases}\qquad u(r,t=0)=0 \tag{3.1}$$

which corresponds to a quiescent cylindrical pocket of radius $R_i$ composed of equilibrium combustion products $Y_i^{b,0}$ at the adiabatic flame temperature $T^{b,0}$ immersed in the fresh mixture ($Y^u$, $T^u$). Calculations were performed for different initial radii, $R_i$, ranging from $\delta_{T0}$ to $\delta_{T0}/4$, which is close to the critical radius of ignition for these simulations. To avoid numerical difficulties, the step discontinuities in the initial conditions were smoothed over an interval of length $\delta_{T0}/10$ centered around $R_i$. It is

important to recognize that a real expanding cylindrical flame at these conditions quickly develops a cellular structure because of thermo-diffusive instabilities - this one dimensional model suppresses this effect. However, this assumption was invoked purposefully since the key point of this computation was to determine the sensitivity of curved cylindrical flames, and not as an actual computation of the dynamics of a real expanding flame.

The flow conditions and characteristics of the DNS database that is analyzed in this chapter are described in detail in Ref. [71] and references therein. The software utilized for these simulations is based on a low-Mach-number formulation of the reacting flow equations for which the limitations imposed by the Courant-Friedrichs-Lewy condition do not require the very small time steps needed by classical DNS codes based on fully compressible Navier-Stokes equations. The code also implements an adaptive mesh refinement strategy to resolve the flame zone and regions of intense vorticity in greater detail. The combination of these approaches allows for the simulation of flame fronts over long durations and enables meaningful estimates of turbulent flame brush features [71, 91].

The DNS considered in this chapter were performed in a computational domain consisting of a high-aspect-ratio ($5\delta_{T0}:5\delta_{T0}:40\delta_{T0}$) parallelepiped volume where the flow was initialized with fresh $H_2$/air mixture beneath the hot combustion products, resulting in a downward-propagating flame. Periodic lateral boundary conditions were specified, along with an insulating free-slip fixed wall at the bottom of the domain and outflow at the top. A density-weighted forcing term in the momentum equations was used to maintain the turbulent background, characterized by an integral length scale

$l_t/\delta_{T0} = 0.5$ and turbulent intensities $u'/s_{L0} = 3.69$ (Case A31), $u'/s_{L0} = 17.1$ (Case B31), $u'/s_{L0} = 32.9$ (Case C31) and $u'/s_{L0} = 106.8$ (Case D31). This numerical configuration does not have a direct experimental analogue, but this approach is preferred to using an inflow boundary as it allows for arbitrarily large turbulence levels that are numerically incompatible with an inflow boundary condition. Further details of the DNS database are reported in Table 2, where the Karlovitz number, Damköhler number, and Reynolds number for the various cases are listed.

**Table 2. Turbulent flame properties for the four simulations at equivalence ratio $\phi$ = 0.31. The Reynolds number *Re* is evaluated utilizing the kinematic viscosity of the reactants $\nu^u$ = 0.175 $cm^2/s$ (viscosity of the adiabatic equilibrium products is ten times higher $\nu^b$= 1.74 $cm^2/s$)**

| Case | A31 | B31 | C31 | D31 |
|---|---|---|---|---|
| $\delta_{T0}$ [mm] | 1.9 | 1.9 | 1.9 | 1.9 |
| $s_{L0}$ [cm/s] | 4.68 | 4.68 | 4.68 | 4.68 |
| $u'/s_{L0}$ | 3.69 | 17.1 | 32.9 | 106.8 |
| $l_t/\delta_{T0}$ | 0.5 | 0.5 | 0.5 | 0.5 |
| $1/\tau_t = u'/l_t$ | $7.38\, s_{L0}/\delta_{T0}$ | $34.2\, s_{L0}/\delta_{T0}$ | $65.8\, s_{L0}/\delta_{T0}$ | $213.6\, s_{L0}/\delta_{T0}$ |
| $Ka = \left(u'^3 l_t/s_{L0}^3\delta_{T0}\right)^{1/2}$ | 10 | 100 | 266 | 1562 |
| $Da = \left(l_t/\delta_{T0}\right)/\left(u'/s_{L0}\right)$ | $1.36 \times 10^{-1}$ | $2.92 \times 10^{-2}$ | $1.52 \times 10^{-2}$ | $4.68 \times 10^{-3}$ |
| $Re = u' l_t/\nu^u$ | 9.4 | 43.4 | 83.6 | 271.3 |

According to the Borghi-Peters diagram (see Section 2.2) case A31 and B31 are in the "thin reactions zone" regime while case C31 and D31 are in the "distributed reactions zone". However, reactions remain confined to thin fronts for all the cases (see Figure 5 in Ref. [71]) and no transition to distributed reactions is observed. This is the result of the strong effect of non-unity Lewis number and preferential diffusion of species which substantially increase the reaction rate of positively stretched flame elements as discussed

in Ref. [71] and in the next sections. Similarly to most DNS studies, the magnitude of $Da$ and $Re$ of these simulations is small relative to many experiments (such as those described in Chapter 1) and turbulent premixed flames of practical interest. These limitations, which depend on DNS computational requirements, will be commented on further in Section 3.6.

## 3.2 Definitions

Burning velocities were calculated using the same procedure described in Day *et al.* [28]. As described in Section 2.1.1, this definition is one of the most numerically robust and meaningful definition of burning speeds. For the three-dimensional flames obtained by the DNS, this procedure starts with the tessellation of a temperature isosurface $T_{ref}$, and the construction of normal vectors by extending along integral curves $s_j$ of temperature gradient. A prism, $\Omega$, can then be built as shown in Figure 3-2. The consumption speed $s_c$ is then calculated by integrating the hydrogen mass consumption rate $\dot{\omega}_{H_2}$ over the $\Omega$ volume and normalizing by the area $A_{ref}$ intersection between $\Omega$ and the flame surface, multiplied by the initial hydrogen density contained in the reactants $\left(\rho Y_{H_2}\right)_{reac}$

$$s_c = \frac{\int_\Omega \dot{\omega}_{H_2} d\Omega}{\left(\rho Y_{H_2}\right)_{reac} A_{ref}} \tag{3.2}$$

The mean curvature $K_C$ and strain rate $K_S$ are computed at the flame surface using the identities (see Section 2.1)

$$\begin{aligned} K_C &= \nabla \cdot \vec{n} \\ K_S &= -\vec{n}\vec{n} : \nabla \vec{u} + \nabla \cdot \vec{u} \end{aligned} \tag{3.3}$$

where $\vec{n}$ is a unit vector locally aligned with the temperature gradient and $\vec{u}$ represents the gas flow velocity vector. The following analogues of equation (3.2) are used for the geometries of Figure 3-1:

$$\text{PCF:} \qquad s_c = \int_0^{L/2} \dot{\omega}_{H_2} dx \Big/ \left(\rho Y_{H_2}\right)_{reac} \tag{3.4}$$

$$\text{TCF:} \qquad s_c = \int_0^{R} \dot{\omega}_{H_2} r\, dr \Big/ \left[\left(\rho Y_{H_2}\right)_{reac} R_{ref}\right] \tag{3.5}$$

$$\text{ECF:} \qquad s_c = \int_0^{\infty} \dot{\omega}_{H_2} r\, dr \Big/ \left[\left(\rho Y_{H_2}\right)_{reac} R_{ref}\right] \tag{3.6}$$

where, for the two curved flames geometries, $R_{ref}$ corresponds to the radial position at which the temperature is equal to $T_{ref}$, and $K_C = 1/R_{ref}$. The reference flame isosurface in the above definitions was chosen as the $T_{ref} = 1088K$ isotherm, which corresponds to the position at which the consumption rate of hydrogen $\dot{\omega}_{H_2}$ peaks in a laminar one dimensional unstretched flame, as calculated by PREMIX [147]. Sensitivity studies (presented in Appendix B.1) were performed by repeating these procedures using $T_{ref}$

surfaces of $990K$ and $1190K$ for the model calculations and DNS, showing little change in the conclusions presented later in this chapter.

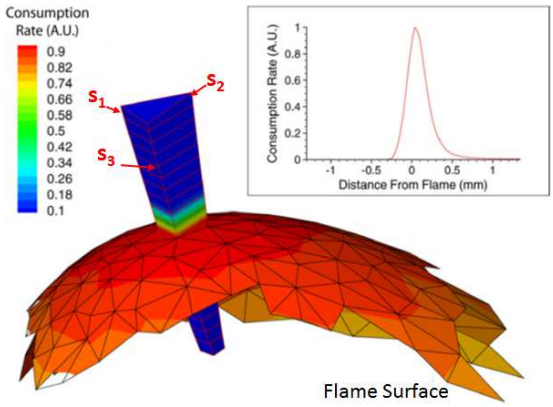


**Figure 3-2. Prism shaped volume, $\Omega$, constructed using curves $s_j$ locally normal to the temperature isotherms; the inset plot shows a typical variation of $\dot{\omega}_{H_2}$ along $s_j$ [28].**

To determine the local flame thickness, temperature and $H_2$ consumption rate fields were interpolated along the integral curves $s_j$ of Figure 3-2. From these profiles, a flame thickness based on maximum temperature gradient, $\delta_T$, and full width at half maximum of $H_2$ consumption rate profile, $\delta_{H2}$, were defined for each of the triangular elements dividing the flame surface as

$$\delta_T = \frac{1}{3}\sum_{j=1}^{3}\frac{T^{b,0}-T^{u}}{\left(dT_j/ds_j\right)_{max}} \tag{3.7}$$

$$\delta_{H2} = \frac{1}{3}\sum_{j=1}^{3}\mathrm{FWHM}\left(\dot{\omega}_{H_2,j}\left(s_j\right)\right) \tag{3.8}$$

where the summation is taken over the three $s_j$ corresponding to a single triangular element. The lengths $\delta_T$ and $\delta_{H2}$ are intended to provide an estimate of the local thickness of preheat-zone and $H_2$ consumption layer, respectively. Also, note that the difference $T^{b,0} - T^u$ used to normalize the temperature gradient is purely a reference value, since the local temperature values in lean hydrogen flames can differ from the adiabatic flame temperature, due to Lewis number effects and preferential diffusion of species. The analogous flame thickness definitions for the 1D geometries are readily obtained by substituting $s_j$ in equations (3.7) and (3.8) with either $r$ for the TCF and ECF, or $x$ for the PCF, and discarding the averaging over different $s_j$.

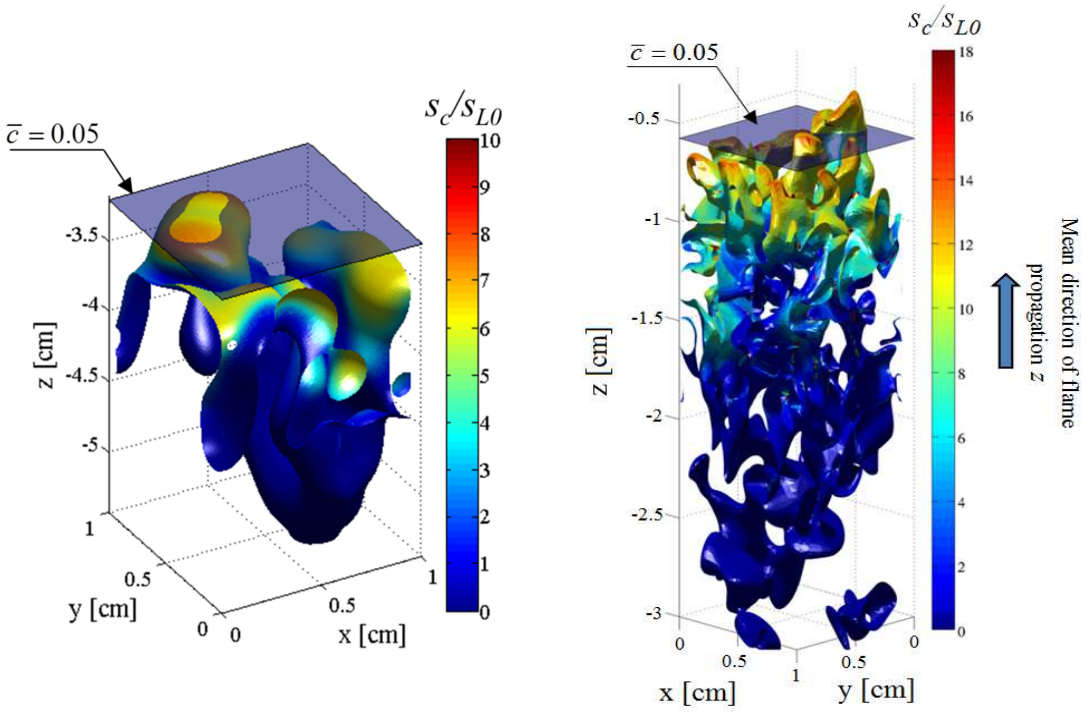


**Figure 3-3. Instantaneous snapshots of the $T_{ref} = 1088K$ isosurface colored by local consumption rate $s_c$ for case A31 (left) and C31 (right). The transparent plane ($\bar{c} = 0.05$) indicates the z-position at which 1/20 of the total consumption of $H_2$ in the entire computational domain is reached. The flames are propagating upward in these images.**

Statistical data for the DNS were gathered at multiple time instants on temporal intervals in which the turbulent flame can be considered statistically stationary (see Figure 7a in Ref. [71]). To identify the leading edge of the turbulent flame brush, the $H_2$ consumption rate field was averaged spatially at each time instant in the direction perpendicular to the mean direction of flame propagation, obtaining a one dimensional average consumption rate profile. Based on this profile, the leading edge of the flame brush was then defined as the portion of space comprised between the most forward lying flame position towards the reactants and the position at which the cumulative average $H_2$ consumption rate reaches 1/20 of the total. This particular value was chosen for practical reasons as a compromise between collecting values sufficiently close to the edge of the flame brush and having enough realizations across different snapshots in time to build meaningful statistics (see Appendix B.2). This procedure is equivalent to defining a progress variable $\overline{c}$ at each time instant based on the instantaneous consumption rate of $H_2$ and then defining the leading edge as the region $0 \leq \overline{c} \leq 0.05$ as shown in Figure 3-3. We note also that implicit within the approach described above is an ansatz that the flame is statistically flat.

### 3.3 One dimensional numerical simulations

In interpreting the results, it is important to recognize that the sensitivity of premixed flames to large stretch values is not unique, but a function of the stretch profile through the flame and, therefore, the configuration in which the calculation is performed [42, 49] (see Section 2.1.2). This also implies that the maximum burning rate $s_{L,max}$ is not a

unique quantity but varies with geometrical configuration. In order to illustrate this sensitivity, Figure 3-4 presents consumption speed $s_c$ values plotted against flame stretch, $\kappa$, for the geometries shown in Figure 3-1. The stretch rate, $\kappa$, is evaluated at the $T_{ref}$ isotherm applying the following definitions:

$$\text{PCF: } \kappa = \frac{\partial u_z}{\partial z} \qquad \text{TCF: } \kappa = \frac{\partial u_z}{\partial z} \qquad \text{ECF: } \kappa = \frac{1}{R_{ref}} \frac{dR_{ref}}{dt} \tag{3.9}$$

where $u_z$ represent the flow velocity in the $z$ direction (see Figure 3-1) and $R_{ref}$ is defined as in equations (3.5) and (3.6). A maximum value of the burning velocity is only evident for the PCF. This is due to the fact that in Figure 3-4, as in all the following figures, results for the ECF are plotted starting from the time instant at which maximum $H_2$ consumption rate is reached, to avoid plotting the initial phase of the ignition process (see Appendix A.2). It is known that for lean $H_2$/air mixtures ignition transients can be quite long [41], as evidenced by the slow convergence of the various ECF toward a common solution at low stretch rates. A maximum burning velocity is more ambiguous for these flames, as it is difficult to differentiate the ignition transient from the quasi-steady stretch sensitivity. Results for the TCF are also plotted up to the highest values of consumption speed, which is reached just before extinction, as for the PCF. At low stretch rates, all five curves tend to converge towards a common solution as expected, but diverge for higher values; e.g., curved flames display a higher consumption rate then the PCF. These curves also suggest that for this flame $s_{L,max}$ values of about 12-18 times

larger than the unstretched burning velocity $s_{L0}$ can be achieved, depending on how flame stretch is applied.

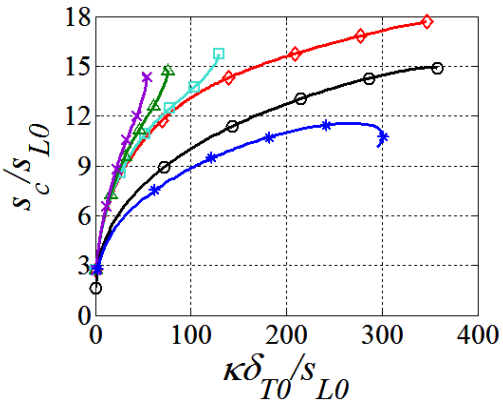


**Figure 3-4. Consumption rate $s_c$ dependence on stretch rate $\kappa$ for PCF " * ", TCF "○", ECF with different initial ignition radius ($R_i/\delta_{T0}=0.25$ "◊", $R_i/\delta_{T0}=0.5$ "□", $R_i/\delta_{T0}=0.75$ "Δ", $R_i/\delta_{T0}=1$ "x").**

For reference, Figure 3-5a re-plots several of these cases as a function of curvature. The flame thickness itself is a strong function of curvature/stretch rate as shown in Figure 3-5b and c, which plot the ratio of unstretched to stretched flame thickness $\delta_T$ and $\delta_{H2}$ as a function of mean curvature $K_C$, for the curved laminar flame geometries. The figure shows that increasing curvature can reduce the flame thickness $\delta_T$ up to 6-8 times and $\delta_{H2}$ up to 2.5-3 times relative to the unstretched flame. For the TCF, Figure 3-5c shows that $\delta_{H2}$ at first becomes thinner with increasing curvature and then thickens because the flame is pushed closer to stagnation axis ($r=0$) reducing the residence time available for the reactions to complete. At $K_C\delta_{T0}\sim 7$ the curve is terminated, because for curvatures larger than this value the flame has been pushed so close to stagnation axis that the $H_2$

consumption rate $\dot{\omega}_{H_2}$ at $r=0$ becomes larger than half of the maximum value, making $\delta_{H2}$ ill-defined. The thermal thickness $\delta_T$ instead increases monotonically as the flame becomes more curved as shown in Figure 3-5b. For the ECF, however, both flame thicknesses $\delta_{H2}$ and $\delta_T$ display a non-monotonic behavior [41, 48]. For sufficiently low values of curvature, however, ECF are thinner than TCF.

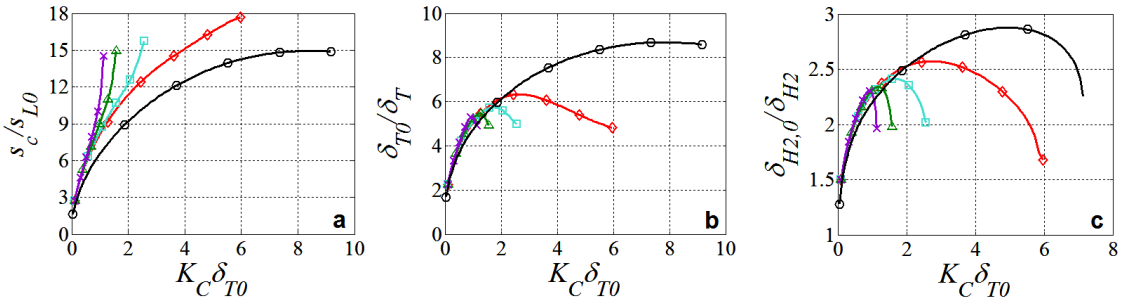


**Figure 3-5. Consumption rate $s_c$ (a), inverse of flame thickness $\delta_T$ (b) and $\delta_{H2}$ (c) plotted against mean curvature $K_C$ for the curved flame geometries: symbols are the same as in Figure 3-4.**

Finally, Figure 3-6 presents the strain rate $K_S$ for the curved flame geometries in Figure 3-1 calculated at the $T_{ref}=1088K$ isosurface utilizing the following expressions:

$$\begin{aligned} &\text{PCF: } K_S=\frac{\partial u_z}{\partial z}=\kappa \quad \text{TCF: } K_S=\frac{\partial u_z}{\partial z}+\frac{u_r}{R_{ref}} \quad (u_r<0) \\ &\text{ECF: } K_S=\frac{u_r}{R_{ref}} \quad (u_r>0) \end{aligned} \tag{3.10}$$

For the PCF, strain rate and stretch are the same while for TCF and ECF strain rate depends also on the curvature of the flame as discussed in Section 2.1. Figure 3-6 shows

that for the same value of curvature $K_C$ the stretch rates $\kappa$ for ECF and TCF are similar while the strain rates $K_S$ differ substantially. As explained in Section 2.1, $K_S$ is a measure of the flow velocity spatial gradients contribution to flame stretch. The geometries of Figure 3-1 are each characterized by a different flow field structure and this represents another reason why their response to stretch rate is not the same.

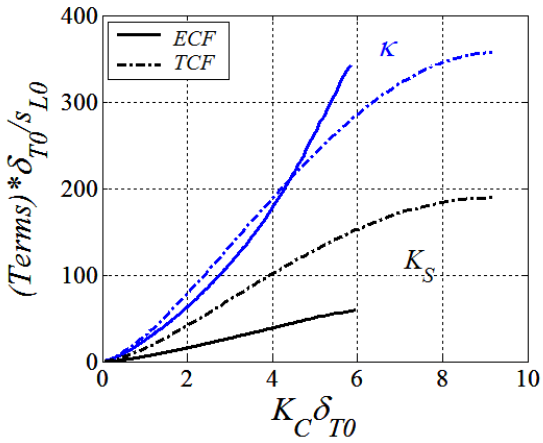


**Figure 3-6. Strain rate $K_S$ and stretch rate $\kappa$ dependence on curvature $K_C$ for expanding cylindrical flame (ECF) with $R_i/\delta_{T0}=0.25$ and tubular counterflow flame (TCF). Every quantity is calculated at the $T_{ref}=1088K$ isosurface applying equations (3.9) and (3.10).**

## 3.4 Turbulent flame front structure

### 3.4.1 Local flame front curvatures, shapes and strain rates

In this section, we start the analysis of the DNS turbulent flames by studying their local curvatures, shapes and strain rates. Firstly, the geometry and shape of the flame front is investigated in terms of principal curvatures $k_1$ and $k_2$ ($K_C=k_1+k_2$, $k_2<k_1$) in Figure

3-7. This figure shows the joint PDFs, weighted by area, of the principal curvatures $k_1$ and $k_2$ of the $T_{ref} = 1088K$ isosurface for case A31 to D31. From this figure it can be seen that the probability of measuring larger values of curvatures grows as turbulence intensity increases and that most of the $T_{ref} = 1088K$ isosurface exhibits convex toward the products (negatively curved $K_C < 0$) geometries, especially at high turbulent intensities. However, at positions where the $T_{ref} = 1088K$ isosurface is negatively curved, the flame is likely non-burning because of the strong non-unity Lewis number effects and preferential diffusion of species characterizing these flames. In fact, for these types of flames, joint PDFs weighted by area have the undesirable effect of including in the statistical analysis large portions of non-burning flame area. A possible solution to this problem would be to define the "flame area" as the portion of the $T_{ref} = 1088K$ isosurface over which the fuel consumption rate is above a given threshold [28]. However, this threshold is arbitrary. The strategy adopted in the rest of the chapter, unless otherwise specified, consists in weighting the PDFs by the local fuel consumption, $\int_\Omega \dot{\omega}_{H_2} d\Omega$, rather than area, $A_{ref}$ (see Figure 3-2). With this approach, portions of the flame front that are not burning are excluded from the statistical analysis without the inclusion of arbitrary parameters. Besides, the integral of PDFs weighted by fuel consumption is physically meaningful because it is equal to the total consumption rate of fuel over the entire computational domain and is directly related to the total turbulent flame speed $s_T$ (see Chapter 1).

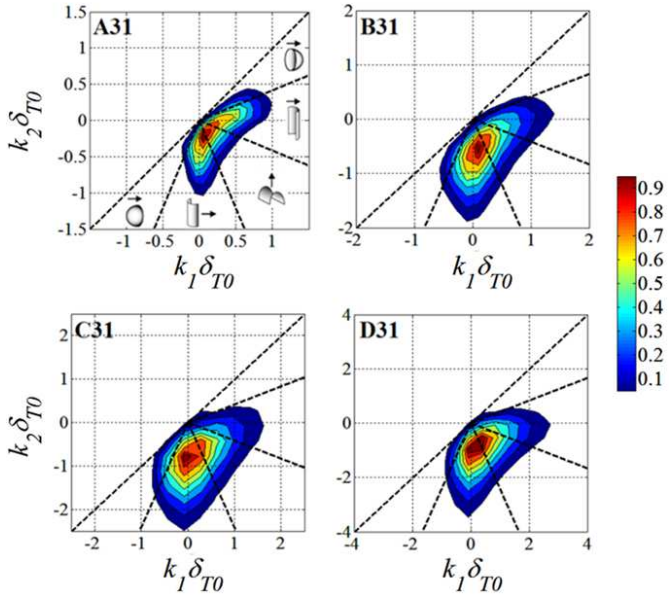


**Figure 3-7. Area-weighted joint PDFs of the principal curvatures $k_1$ and $k_2$ ($K_C = k_1 + k_2$, $k_2 < k_1$) of the $T_{ref} = 1088K$ isosurface for case A31, B31, C31 and D31. The PDFs are normalized to the peak values. Small pictures in the figure of case A31, show a classification of the flame shapes in (from top, clockwise) spherical and cylindrical convex toward the fresh gases, saddle-point, cylindrical and spherical convex toward the burnt gases (arrows point toward the unburnt side).**

Figure 3-8 shows the same data of Figure 3-7, but weighted by local fuel consumption; clearly, much of the negatively curved portions of the $T_{ref} = 1088K$ isosurface have been excluded in these plots. From this figure it can be seen that at low turbulent intensity (i.e. Case A31) most of the fuel is consumed by flame elements with a cylindrical/spherical shape convex toward the reactants. For higher turbulent intensities, instead, the flame becomes more tightly wrinkled and exhibits also saddle-point and cylindrical toward the products geometries. Figure 3-8 also shows that the most highly curved elements tend to have a cylindrical geometry [59] and this partially justifies the choice of cylindrical one-dimensional geometries in Figure 3-1, as also discussed in Section 2.3.

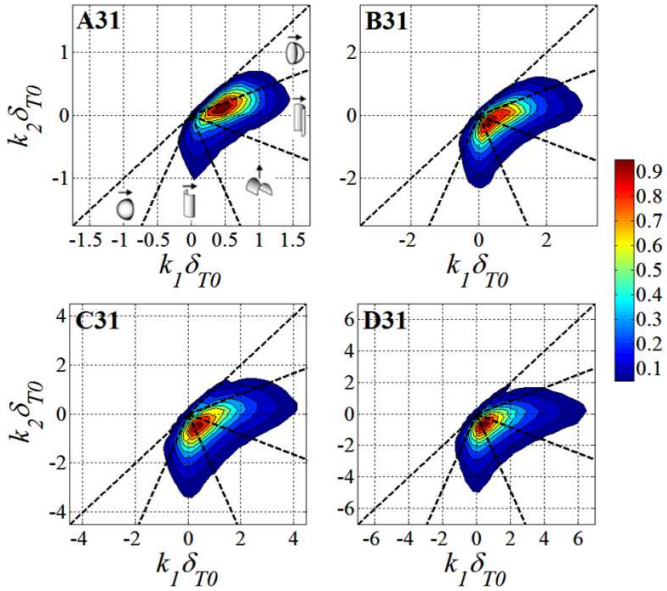


**Figure 3-8. Fuel consumption-weighted joint PDFs of principal curvatures $k_1$ and $k_2$ ( $K_C = k_1 + k_2$, $k_2 < k_1$) of the $T_{ref} = 1088K$ isosurface for case A31, B31, C31 and D31. The PDFs are normalized to the peak values. Legend is the same as in Figure 3-7.**

Secondly, we analyze the local strain rates at the turbulent flame fronts. Figure 3-9 shows the fuel consumption weighted joint PDFs of strain rate $K_S$ and curvature $K_C$ for cases A31 to D31. Mean strain rate values increase with increasing turbulent intensity with the peak probability in these joint PDFs is approximately located at $K_S \sim 1/\tau_t = u'/l_t$ (see Table 2). For each case the correlation $K_S - K_C$ is negative, similarly to past DNS studies which considered lower turbulent intensities [102-106]. As discussed in Section 2.3, this trend arises from defocusing of heat in front of positively curved flamelets, and vice versa for negatively curved flamelets. However, non-unity Lewis number effects and preferential diffusion of species tend to increase (decrease) the temperature at positively (negatively) curved portions of the flame front contrasting the effect of heat defocusing (focusing). For this reason $K_S$ values are more skewed toward positive values than the

data presented in Figure 2-19, even though weighting the joint PDFs by fuel consumption tends to highlight positively curved portions of the flame front for which $K_S$ tends to be negative. Furthermore, for $K_C \sim 0$, the spread between lower and higher values of $K_S$ tends to be larger than for highly positive or highly negative $K_C$ values (i.e. the joint PDFs have a triangular shape) and this spread grows with increasing turbulence levels. This is due to the fact that for $K_C \sim 0$ strain rates are dominated by random turbulent straining rather than correlation with curvature. Finally, it is interesting to note that the negative correlation of $K_S$ and $K_C$ differs from the data presented in Figure 3-6 for the laminar flame calculations, for which $K_S$ increases monotonically with $K_C$. This observation affects the comparison between laminar and turbulent flames especially for highly curved flame elements which are of interest for the study of leading point burning rate models as detailed in the next sections.

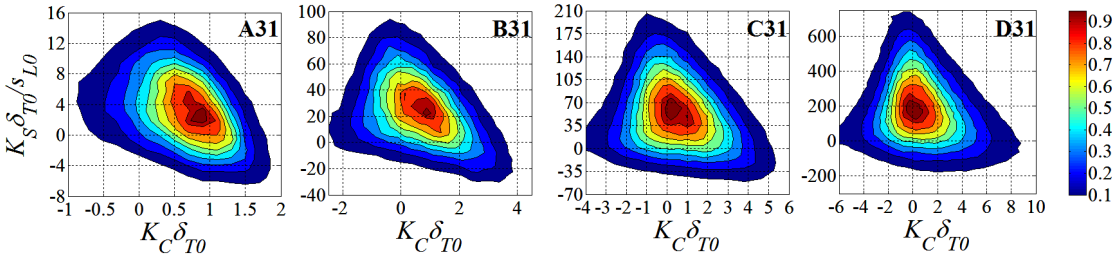


**Figure 3-9. Fuel consumption-weighted joint PDFs of curvature $K_C$ and strain rate $K_S$ at the $T_{ref} = 1088K$ isosurface for case A31, B31, C31 and D31. The PDFs are normalized to the peak values.**

### 3.4.2 Case A31

In this section we compare the local characteristics (flame speed, flame thickness, curvature and strain) of the turbulent premixed flame obtained in Case A31 with the laminar flame computations described in Section 3.3. The low turbulent intensity of this case makes its description simpler compared to the other cases which are discussed in the next section. In the following discussion, flame front characteristics are described in term of local mean curvature $K_C$, since strain rates are relatively low (see Figure 3-9) and most of the flame front displays a cylindrical or spherical shape (see Figure 3-8).

Figure 3-10 presents fuel consumption-weighted joint PDFs of mean curvature $K_C$ and burning speed $s_c$ (a), inverse of flame thickness $\delta_T$ (b), $\delta_{H2}$ (c) and strain rate $K_S$ (d) and compares them with data obtained from laminar flames computations described in the previous section. These figures show that the position of the joint PDFs peak probability is approximately situated between the laminar simulations except for the strain rate; for reference, in Figure 3-10 about 50% of the total $H_2$ burning is comprised by flame elements inside the iso-contour 0.4 of the joint PDFs. On the contrary, the strengths of the correlations $s_c - K_C$, $\delta_T - K_C$, $\delta_{H2} - K_C$ are weaker than that predicted by the model laminar flames calculations. This means that highly positively curved flamelets tend to burn less intensely and tend to be thicker than the model laminar flames with the same curvature, and vice versa for flat or negatively curved flamelets. These trends are explained by the negative correlation between strain rate and curvature which is opposite to the monotonic increase of strain rate with curvature characterizing the laminar model flames. In fact, Figure 3-10d suggests that at high curvatures ($K_C \delta_{T0} > 1$), the strain rate at the turbulent flame front tends to be lower than what is predicted by the

model laminar flames and vice versa at low curvatures ( $K_C\delta_{T0} < 0.5$ ). Besides, the joint PDFs $\delta_T - K_C$ and $\delta_{H2} - K_C$ appear to be more concentrated around the peak probability values and to be less sensitive to curvature variations. For this reason, in Figure 3-10b and Figure 3-10c, the contour corresponding to the lowest probability plotted does not extend to curvature values as negative as those of the $s_c - K_C$ joint PDF in Figure 3-10a.

The remaining dispersion in the joint PDFs data can be explained by unsteady effects in the flame response. Non-flamelet behaviors are also partly responsible for the disparity in behavior between the model laminar flames and flamelets with low and negative curvatures. In fact, these flamelets are mostly situated at the borders of the cellular structures that characterize the geometry of this case, as shown in Figure 3-3. It is known that at these locations diffusive and thermal gradients are not parallel to each other due to the low burning rates of these elements and considerable species fluxes parallel to the temperature isosurfaces occur [28]. As a consequence, the one dimensional laminar flames described in the previous section are not an appropriate model for the flame behavior these locations.

Finally, Figure 3-10 shows that the consumption speed values of the most highly curved flamelets (~7 $s_{L0}$ ) are about half the $s_{L,max}$ values obtained from the model laminar flame calculations described in Section 3.3 (~12-18 $s_{L0}$ ). A similar consideration is valid for flame thicknesses, since the thinnest portions of the turbulent flame front are about twice as large as the critically stretched model laminar flames. This indicates that at the low turbulent intensity and low Reynolds number characterizing case A31, critically stretched flames are not a relevant model for turbulent flame propagation. This conclusion is compared to what is observed at higher turbulent intensities in the next sections.

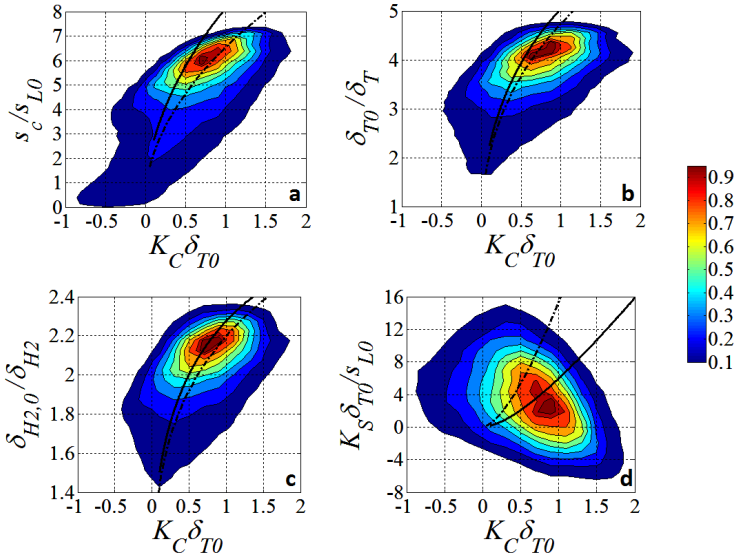


**Figure 3-10. Fuel consumption-weighted joint PDFs of mean curvature $K_C$ and burning speed $s_c$ (a), inverse of flame thickness $\delta_T$ (b), $\delta_{H2}$ (c) and strain rate $K_S$ (d) for case A31. The PDFs are normalized to the peak values. Lines superimposed to the contours refer to results obtained from one-dimensional laminar flame computations (see Figure 3-5): dot-dashed lines refer to TCF computations while solid lines refer to ECF computations with $R_i/\delta_{T0}=0.25$.**

### 3.4.3 Case B31, C31 and D31

In this section, the flame front characteristics of the higher turbulent intensity cases (B31, C31 and D31) are analyzed. Figure 3-11 shows the fuel consumption weighted joint PDFs of thermal flame thickness $\delta_T$ with curvature $K_C$ (top row) and strain rate $K_S$ (bottom row), for case B31, C31 and D31. The first observation from these figures is that most of the fuel is consumed in flamelets that are thinner than the unstretched laminar flame $\delta_{T0}$. Contrary to what is observed for case A31, the dependence of $\delta_T$ on either $K_C$ or $K_S$ is non-monotonic due to the strong competition between curvature and strain rate effects; in fact, compared to case A31, case B31, C31 and D31 are characterized by much higher mean strain rates, as shown in Figure 3-9. These trends are consistent with

those of past DNS studies with single step chemistry [105, 106] (see Figure 2-21 and Figure 2-22) and complex chemistry [121] (see Figure 9 in the cited paper) except for the fact that here the turbulent flame front is much thinner than the unstretched laminar flame. Observing the bottom row of Figure 3-11 it is clear that $\delta_T$ is correlated with $K_S$ only in regions where the flame is sufficiently thin and the strain rate is sufficiently negative or positive. For example, for case B31 the correlation $\delta_T - K_S$ is strong only for $\delta_{T0}/\delta_T > 4$ and $K_S\delta_{T0}/s_{L0} > 60$ or $K_S\delta_{T0}/s_{L0} < -20$. For the higher turbulent intensities of case C31 and D31 similar regions can be identified but only with growing difficulty because of the increased scatter of the joint PDFs due to unsteady effects. The top row of Figure 3-11 suggests that thick flames (i.e. low values of $\delta_{T0}/\delta_T$ ) that do not correlate with $K_S$ are mostly associated with negatively curved flamelets for which strain rates are relatively low (see Figure 3-9). The negative correlation between strain rate and curvature explain also the negative correlation between $\delta_{T0}/\delta_T$ and $K_C$, for $K_C > 0$. In summary, the trends shown in Figure 3-11 can be interpreted in terms of local strain rates and their correlation with curvature. The growing dispersion in the joint PDFs for increasing turbulence levels is likely due to unsteady effects.

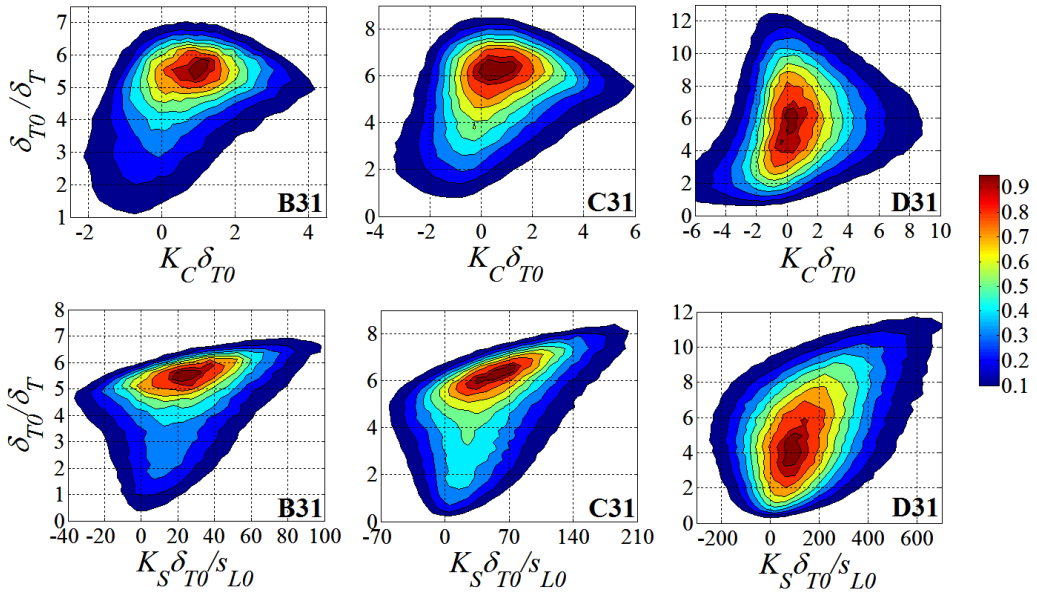


**Figure 3-11. Fuel consumption-weighted joint PDFs $K_C-\delta_T$ (top row) and $K_S-\delta_T$ (bottom row) for case B31, C31 and D31. The PDFs are normalized to their peak values.**

Similar observations are valid for the flame thickness measured by $\delta_{H2}$. Figure 3-12 shows the fuel consumption weighted joint PDFs of flame thickness $\delta_{H2}$ with curvature $K_C$ (top row) and strain rate $K_S$ (bottom row), for case B31 and C31, while case D31 is not shown. For this latter case, the $H_2$ consumption layer is extremely contorted (see Figure 5 in Ref. [71]) and pockets of burned gases frequently form. At the center of these pockets, the $H_2$ consumption rate does not decrease to half of the maximum value computed along $s_j$, making $\delta_{H2}$ ill-defined. Even for case B31 and C31, some caution is necessary when calculating $\delta_{H2}$ since at some positions in the flame front there may not be a clear peak in the hydrogen consumption rate, especially where the flame is burning less intensely. For this reason, the joint PDFs in Figure 3-12 are calculated utilizing only flame elements for which the $H_2$ consumption rate $\dot{\omega}_{H2}$ at the $T_{ref}$ isotherm is greater

than 30% of the maximum value of $\dot{\omega}_{H2}$ in an unstretched laminar flame, which is equal to $0.575\ \ kg/\left(m^3 s\right)$. Despite these difficulty in calculating $\delta_{H2}$, comparing Figure 3-11 and Figure 3-12 it is clear that the overall shape of these joint PDFs is similar, which suggests that $\delta_{H2}$ and $\delta_T$ are controlled by similar physical phenomena.

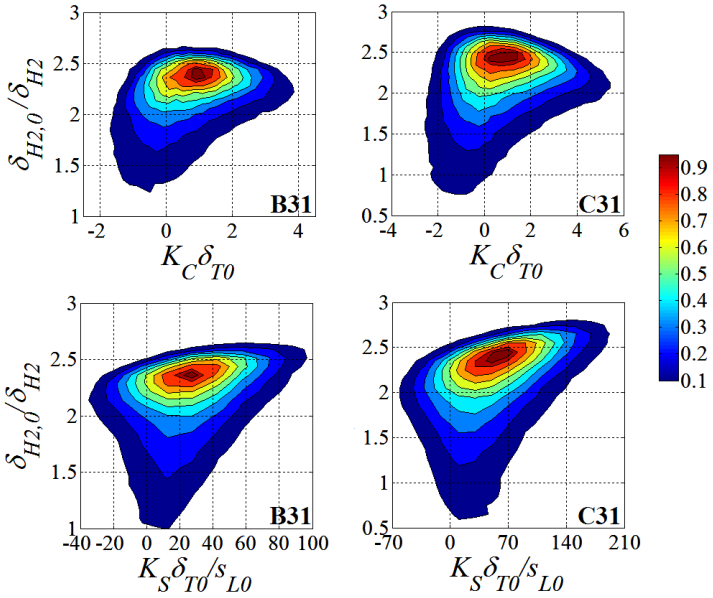


**Figure 3-12. Fuel consumption-weighted joint PDFs $K_C-\delta_{H2}$ (top row) and $K_S-\delta_{H2}$ (bottom row) for case B31 and C31. The PDFs are normalized to their peak values. Only flame elements with $\dot{\omega}_{H2}$ at $T_{ref}=1088K$ larger than 0.3 times $0.575 kg/\left(m^3 s\right)$ are utilized to build these joint PDFs.**

Finally, Figure 3-13 shows the fuel consumption weighted joint PDFs of consumption speed $s_c$ with curvature $K_C$ (top row) and strain rate $K_S$ (bottom row) for case B31, C31 and D31. These figures indicate that consumptions speeds correlate better with local mean curvature rather than strain rate unlike local thermal flame thickness $\delta_T$. This is probably due to the fact that strain rates and curvatures have a different influence on the

thermal gradients than on the structure of the reaction zone. Similar trends were observed for a stoichiometric $H_2$/air flame ($\phi = 1.0$, $T^u = 700K$, $u'/s_{L0} = 1.74$, $l_t/\delta_{T0} = 2$) in Ref. [121], where it was found that local heat release rate correlated better with curvature rather than strain rate (see Figure 8 in the cited paper) while the flame thickness behaved as in Figure 3-11 and Figure 3-12 (see Figure 9 in the cited paper). Furthermore, Figure 3-13 shows that the consumption speed is positively correlated with curvature (as expected for these $Ma_c < 0$ flames) and the data become more scattered as the turbulence intensity increases passing from case B31 to D31. For highly positively curved flamelets, the correlation $s_c - K_C$ appears to be negative, as for $\delta_T - K_C$, but the correlation is much weaker. On the contrary, the dependence on strain is more difficult to interpret and no correlation is easily distinguishable.

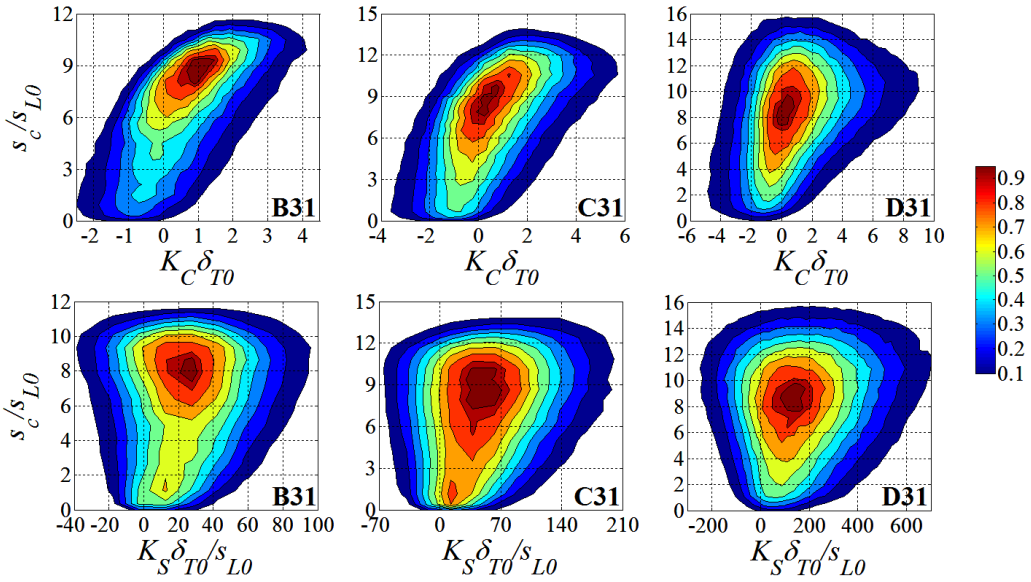


**Figure 3-13. Fuel consumption-weighted joint PDFs $K_C - s_c$ (top row) and $K_S - s_c$ (bottom row) for case B31, C31 and D31.**

Given the complexity of the trends described in Figure 3-11, Figure 3-12 and Figure 3-13, it is clear that a direct comparison between laminar flame models and local statistics of the turbulent flame structure has to be performed with more care, unlike that performed in the previous paragraph for case A31. This is mainly due to the increased geometrical complexity of the flame front, the stronger interaction between curvature and strain rate and the growing influence of unsteady effects for these three cases compared to case A31. For these reasons in the next two paragraphs, the flame front characteristics are analyzed distinguishing between different geometries in an attempt to provide a better comparison with laminar flame computations. Since positively curved flamelets (either cylindrical or spherical) and positively strained flat flamelets are candidates for being leading points flamelets, the next two sections focus on these two geometries.

#### 3.4.3.1 Cylindrical and spherical flamelets

This section investigates the structure of the cylindrical and spherical shaped portions of the flame fronts of case B31, C31 and D31. To identify spherical and cylindrical geometries only flame elements with positive principal curvatures $k_1 > k_2 > 0$ are considered (see Figure 3-8). It should also be noted for case A31 most of the flame front displays cylindrical and spherical geometries (see Figure 3-8) and thus it is possible to compare directly the data described in this section with the data presented in Section 3.4.2.

Figure 3-14 shows the fuel consumption weighted joint PDFs of local mean curvature $K_C$ with consumption speed $s_c$ (a), inverse of flame thickness $\delta_T$ (b), $\delta_{H2}$ (c) and strain rate $K_S$ for the cylindrical and spherical flamelets of case B31. Since the large majority

of the flame elements presented in this figure are characterized by a high consumption speed (unlike the data presented in the previous section), $\delta_{H2}$ is well defined and no further conditioning of its joint PDF with $K_C$ is necessary.

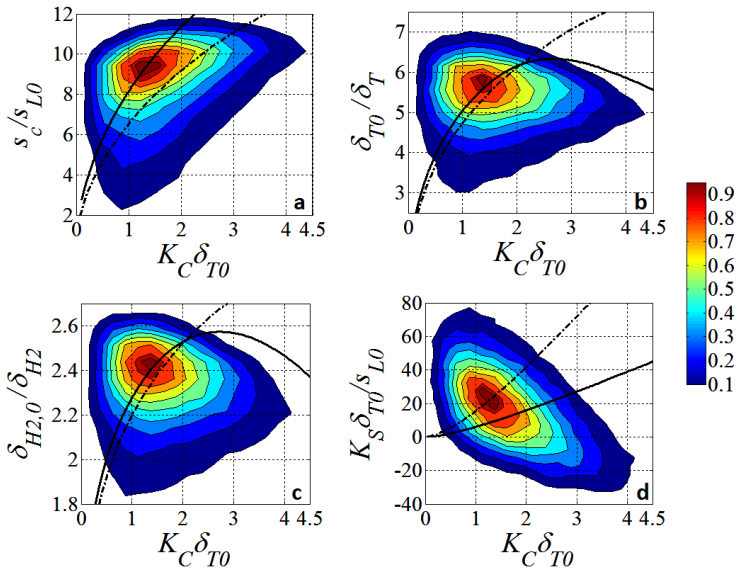


**Figure 3-14. Fuel consumption-weighted joint PDFs of mean curvature $K_C$ and burning speed $s_c$ (a), inverse of flame thickness $\delta_T$ (b), $\delta_{H2}$ (c) and strain rate $K_S$ (d) for case B31. These joint PDFs are built utilizing only positions at which the principal curvatures of the $T_{ref}=1088K$ isosurface are both positive ($k_1>k_2>0$: cylindrical and spherical shaped elements). Legend is the same as in Figure 3-10.**

Similarly to Figure 3-10, the position of the joint PDFs peak probability falls on top of the model laminar flame computations, which are represented by the thick black lines superimposed to the contours of the joint PDFs. This peak probability occurs at substantially higher values of curvature and consumption speed and substantially lower values of flame thickness than for case A31. On the contrary, the overall dependence of $s_c$, $\delta_T$ and $\delta_{H2}$ does not agree with the model laminar flame calculations. The main

reason for this behavior is due to the opposite effect of $K_C$ and $K_S$ on the flame structure as described in the previous section. In fact, Figure 3-14 shows that strain rates and curvatures are negatively correlated for the turbulent flame while for the one-dimensional model laminar flames strain rates increase monotonically with curvature. This effect was already present for case A31 but for case B31 it is much stronger because of higher values of $K_S$. At $K_C \sim 0$, the strain rate tend to be extensive (i.e. positive) and flame elements tend to be thinner and burn more intensely than the model laminar flames with the same $K_C$; in these conditions the effects of curvature are less important than strain rate, as described in detail in the section 3.4.3.2. At $K_C \gg 0$, instead, flame elements are subject to compressive strain rates which counteract the effect of positive curvature (see Figure 3-9). Incidentally, it is also interesting to notice that the dependence of $s_c$ on $K_C$ follows better the laminar models results than $\delta_T$ and $\delta_{H2}$ flames because, as noted in the previous section, consumption speed is less sensitive to the local strain rate than flame thickness.

Similar considerations are valid for cases C31 and D31, whose statistics are shown in Figure 3-15 and Figure 3-16, respectively. For case D31 in Figure 3-16 the joint PDF of $\delta_{H2}$ with $K_C$ is not shown, for the reasons discussed in the previous section. The scatter in these joint PDFs is higher than case B31 likely due to the growing unsteadiness of the flame response, but the peak probability of the joint PDFs falls on top of the model laminar flame computations even at these higher turbulent intensities. This agreement was not necessarily expected, as it is known that non-steady effects decrease the effective stretch sensitivity of the flame [93, 97], and so we had anticipated the DNS results for consumption speed to fall below the laminar calculations. This result might be a

manifestation of the insensitivity of curvature-induced flame speed modifications to frequency, as opposed to its strong sensitivity to nonsteadiness in hydrodynamic stretch [56], that is suggested by theory (see Section 2.1.2).

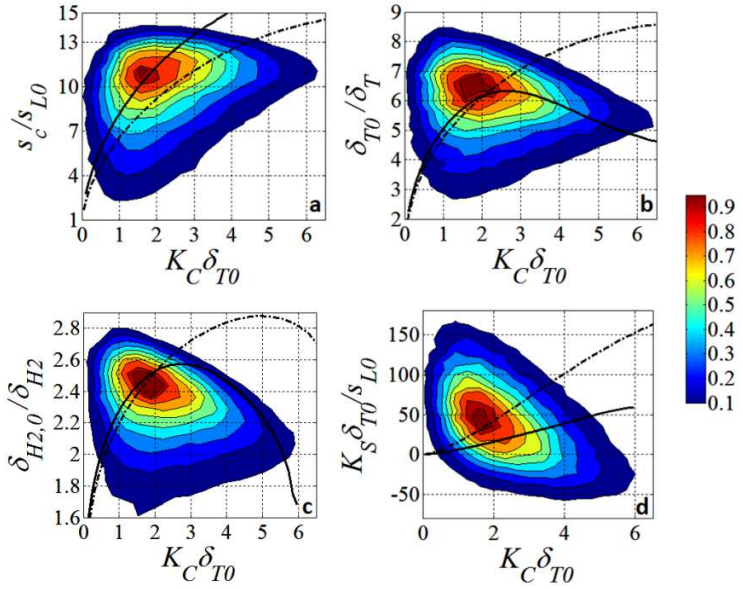


**Figure 3-15. Case C31: fuel consumption-weighted joint PDFs of mean curvature $K_C$ and burning speed $s_c$ (a), inverse of flame thickness $\delta_T$ (b), $\delta_{H2}$ (c) and strain rate $K_S$ (d) for cylindrical and spherical flame elements ($k_1 > k_2 > 0$). Legend is the same as in Figure 3-14.**

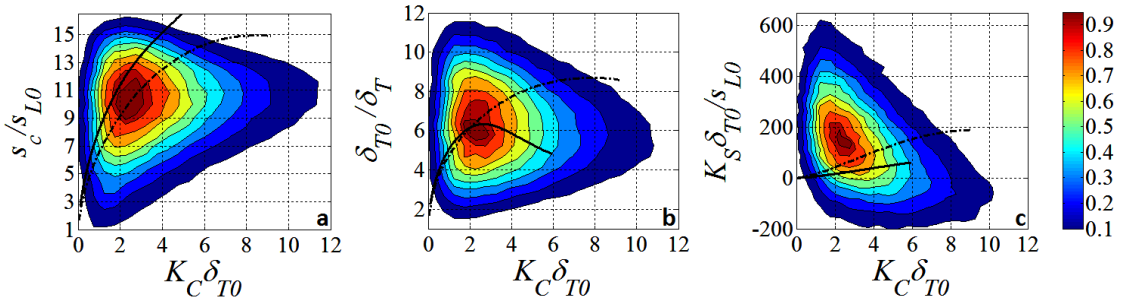


**Figure 3-16. Case D31: fuel consumption-weighted joint PDFs of mean curvature $K_C$ and burning speed $s_c$ (a), inverse of flame thickness $\delta_T$ (b) and strain rate $K_S$ (c) for cylindrical and spherical flame elements ($k_1 > k_2 > 0$). Legend is the same as in Figure 3-14.**

3.4.3.2 Flamelets with low curvature

As shown in Figure 3-8, for case B31, C31 and D31 most of the fuel is consumed by flame elements with $K_C \sim 0$ (i.e. $k_1 + k_2 \sim 0$) and their importance increases with increasing turbulence intensity. For this reason, in this section we investigate the structure of flame elements with low curvature by considering only portions of the flame front at which the mean curvature of the $T_{ref} = 1088K$ isosurface is less than one tenth of the unstretched thermal flame thickness (i.e. $\left|K_C \delta_{T0}\right| < 0.1$). This type of analysis is also important to clarify the discrepancy, highlighted in the previous section, between ECF/TCF computations and flamelets with low curvature.

Figure 3-17 shows the fuel consumption weighted join PDFs of strain rate $K_S$ with consumption speed $s_c$ (a) and flame thickness $\delta_T$ (b), $\delta_{H2}$ (c) for flame elements characterized by $\left|K_C \delta_{T0}\right| < 0.1$ for case B31. Additionally, Figure 3-18 and Figure 3-19 present the same analyses for case C31 and D31, respectively. As it can be observed, the trends in these joint PDFs are well represented by PCF computations (thick black line superimposed to the isocontoturs lines) for case B31 and C31, while for case D31 there is no agreement. It appears that the dispersion in the data characterizing these joint PDFs increases progressively with turbulence intensity until it becomes too large for the PCF computations to be a meaningful comparison. The possible reasons for this dispersion in the data are numerous. First, most of the flame elements with $\left|K_C \delta_{T0}\right| < 0.1$ are characterized by a saddle-point geometry rather than being perfectly flat (see Figure 3-8). These multidimensional effects appear to affect more the consumption rate data rather than flame thickness data presumably because the geometry of the prismatic volume $\Omega$

(see Figure 3-2) used to calculate $s_c$, becomes very distorted when the flame has a saddle-point geometry. Second, the response to strain rate is affected by unsteady effects, as described in Section 2.1.2. Strain rates in a turbulent premixed flame are characterized by a wide range of frenquencies and, as shown in Figure 2-9, the structure of PCF is insensitive to flow pertubations that vary rapidly in time. As a result, the local structure of a turbulent premixed flame front may depend more on the average strain rate rather than on the instantaneous value of strain rate. Third, non-laminar behaviors may be of importance especially for flame elements characterized by low burning rates and large flame thicknesses. In fact, in these conditions it is possible for turbulent eddies to penetrate into the flame and substantially disrupt its laminar structure [7, 70-72] (see Section 2.2). Fourth, flame merging and flame-flame interaction may also cause dispersion in the statistics [118]. These phenomena are also important for the PCF computations since for $K_S > 180\, s_{L0}/\delta_{T0}$ the flame has been pushed so close to stagnation axis that the $H_2$ consumption rate $\dot{\omega}_{H_2}$ at $x = 0$ (see Figure 3-1) becomes larger than half of the maximum value, making $\delta_{H2}$ ill-defined. This is the reason why the $\delta_{H2}$ curves corresponding to PCF are interrupted at this value in Figure 3-18c. Finally, at high turbulent intensities it is possible that turbulent eddies aid the recirculation of hot gasses on the product side of the flame introducing an effect that is not present in the PCF configuration. In the PCF configuration burned gasses are flowing away from the flame surface for every value of strain rate $K_S$.

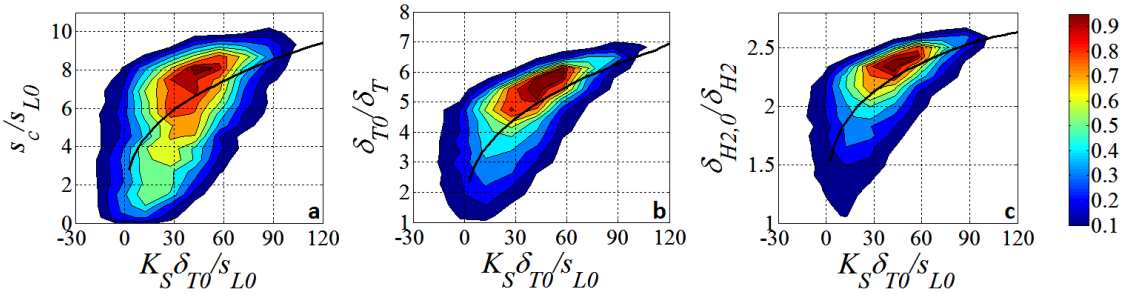


**Figure 3-17. Case B31: fuel consumption weighted joint PDFs of strain rate $K_S$ and burning speed $s_c$ (a), inverse of flame thickness $\delta_T$ (b) and $\delta_{H2}$ (c). Only positions at which the mean curvature of the $T_{ref}=1088K$ isosurface is less than one tenth of the unstretched thermal flame thickness are considered $|K_C\delta_{T0}|<0.1$. The PDFs are normalized to the peak values. Solid lines refer to PCF computations.**

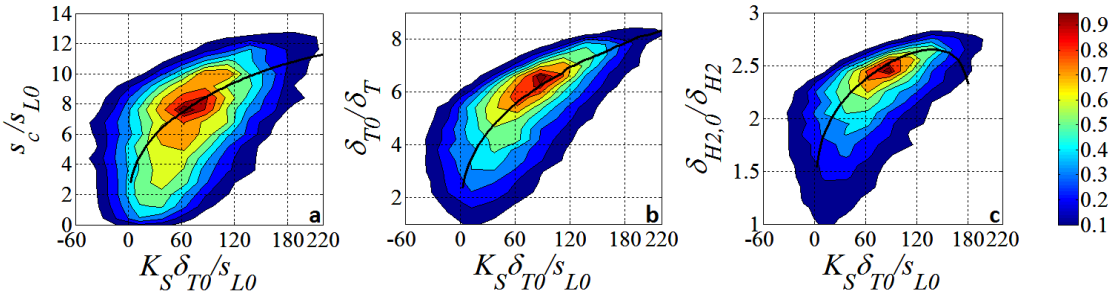


**Figure 3-18. Case C31: fuel consumption weighted joint PDFs of strain rate $K_S$ and burning speed $s_c$ (a), inverse of flame thickness $\delta_T$ (b) and $\delta_{H2}$ (c) for flame elements with $|K_C\delta_{T0}|<0.1$. Legend is the same as in Figure 3-17.**

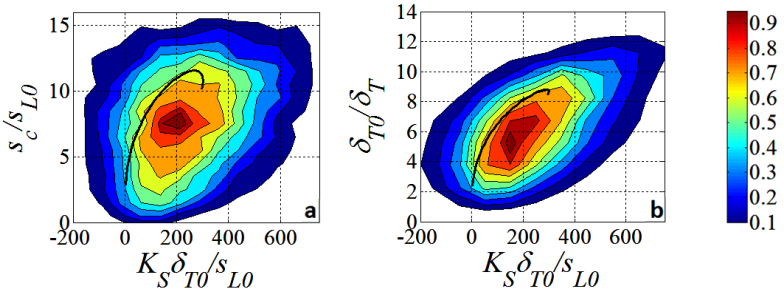


**Figure 3-19. Case D31: fuel consumption weighted joint PDFs of strain rate $K_S$ and burning speed $s_c$ (a), inverse of flame thickness $\delta_T$ (b) and $\delta_{H2}$ (c) for flame elements with $|K_C\delta_{T0}|<0.1$. Legend is the same as in Figure 3-17.**

### 3.5 Flame front structure at the leading edge

We next analyze statistical data collected at the leading edge of the turbulent flame brush, as defined in Section 3.2. Figure 3-20 presents area weighted probability density functions of the consumption rate $s_c$, mean curvature $K_C$ and inverse of flame thickness $\delta_T$ and $\delta_{H2}$ at the leading edge while Figure 3-21 shows area weighted probability density functions of strain rate $K_S$ at the leading edge. Area weighting of pdfs is employed in this section instead of fuel consumption weighting because all the flame elements at the leading edge are burning at a rate much higher than the unstretched laminar flame, as shown in Figure 3-20a: in these conditions area weighting and fuel consumption weighting of the statistical data produce substantially similar results.

The data in Figure 3-20 show that the flame front tends to burn more intensely and in thinner layers as the turbulent intensity is increased from case A31 to D31; values of mean curvature at the leading edge tend to be positive (by geometric necessity), but at higher turbulent intensity more finely wrinkled flames accommodate a wider range of features in the leading edge interrogation zone (e.g., see Figure 3-3). In Figure 3-20d, the PDF of $\delta_{H2}$ for case D31 is not shown. For this case, the $H_2$ consumption rate at the center of the pockets that can occur in the interrogation region do not decrease to half of the maximum value computed along $s_j$, making $\delta_{H2}$ ill-defined, as also described in Section 3.4.3. Figure 3-21 shows that strain rates at the leading edge are mostly skewed toward positive values.

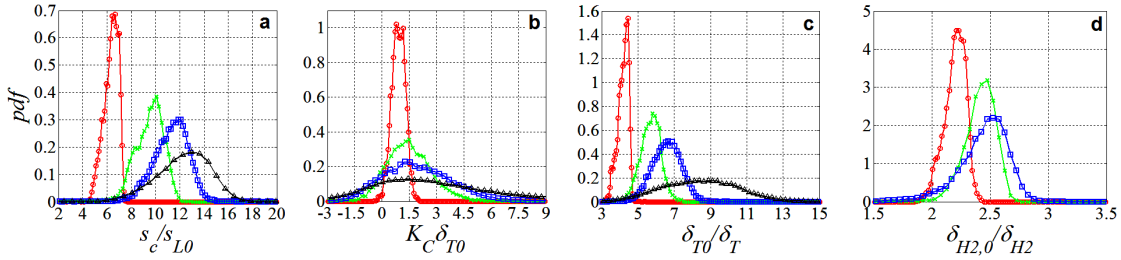


**Figure 3-20. Probability density functions at the leading edge (weighted by area) of consumption rate $s_c$ (a), mean curvature $K_C$, (b) inverse of flame thickness $\delta_T$ (c) and $\delta_{H2}$ (d). Symbols refer to different DNS cases (A31 "○", B31 "x", C31 "□" and D31 "Δ").**

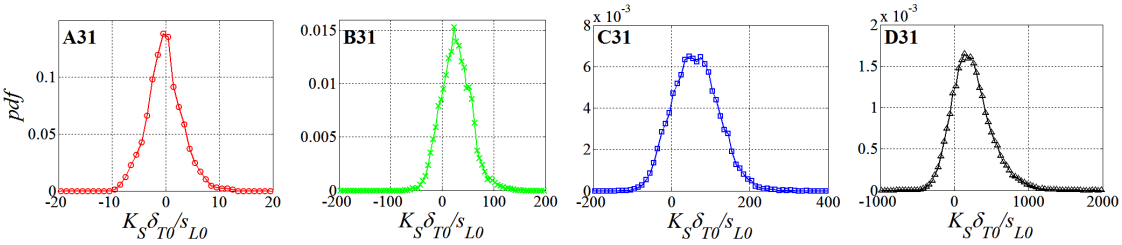


**Figure 3-21. Probability density functions at the leading edge (weighted by area) of strain rate for case A31, B31, C31 and D31.**

To better characterize the geometries of the flame elements at the leading edge of the flame brush, the shape of the flame front is also examined using principal curvatures $k_1$ and $k_2$ ($K_C = k_1 + k_2$, $k_2 < k_1$) in Figure 3-22, which shows their joint PDFs, weighted by area, for case A31 to D31. From this figure it can be seen that most of the flame surface at the leading edge exhibits a geometry that is cylindrical/spherical convex toward the reactants and that the most highly curved elements tend to have a cylindrical geometry [59]. For increasing turbulence intensities, the flame becomes more tightly wrinkled and exhibits also saddle-point and cylindrical toward the products geometries, for the reasons discussed above.

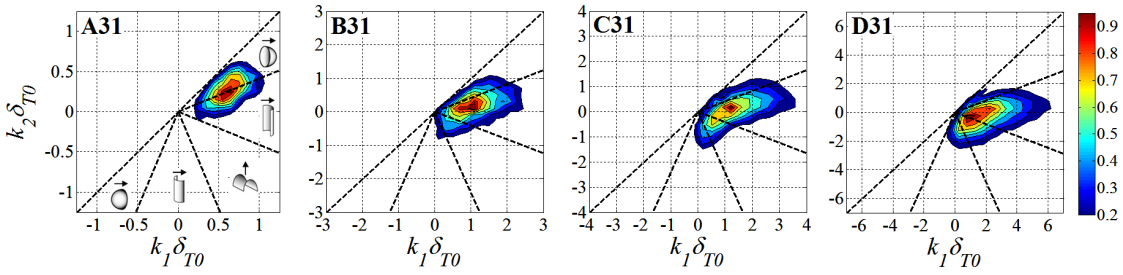


**Figure 3-22. Joint PDFs of the principal curvatures $k_1$ and $k_2$ ($k_2 < k_1$) weighted by area and normalized to the maximum value of weighted probability. Legend is the same as in Figure 3-8.**

To compare statistics collected at the leading edge of the flame brush with the laminar simulations, the pdf's shown in Figure 3-20 are presented in Figure 3-23 and Figure 3-24 in terms of mean $\mu$ and standard deviations $\sigma$ weighted by flame area. Further statistical analysis of the data collected at the leading edge is presented in Appendix B.3. Means $\mu$ and standard deviations $\sigma$ are calculated using the following expressions

$$\mu = \left(\sum_i A_{ref,i}\, x_i\right) \Big/ \left(\sum_i A_{ref,i}\right)$$
$$\sigma = \sqrt{\left(\sum_i A_{ref,i}\, (x_i - \mu)^2\right) \Big/ \left(\sum_i A_{ref,i}\right)} \qquad (3.11)$$

where $A_{ref,i}$ denotes the area of the triangular element (see Figure 3-2) associated with the *i*-th value $x_i$ which either represents mean curvature $K_C$, strain rate $K_S$, consumption speed $s_c$ or flame thickness $\delta_{H2}$ and $\delta_T$.

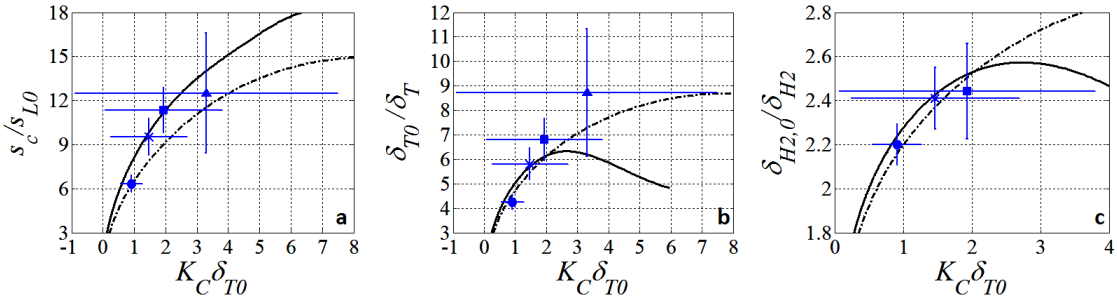


**Figure 3-23. Leading edge mean consumption rate $s_c$ (a), mean of the inverse of flame thickness $\delta_T$ (b) and $\delta_{H2}$ (c) plotted against leading edge average mean curvature $K_C$. Symbols refer to different DNS cases (A31 "●", B31 "x", C31 "■" and D31 "▲"). The total length of the error bars is equal to $\sigma$ on each side. Thicker solid lines refer to ECF computations with $R_i = \delta_{T0}/4$ while thicker dot-dashed lines refer to TCF computations.**

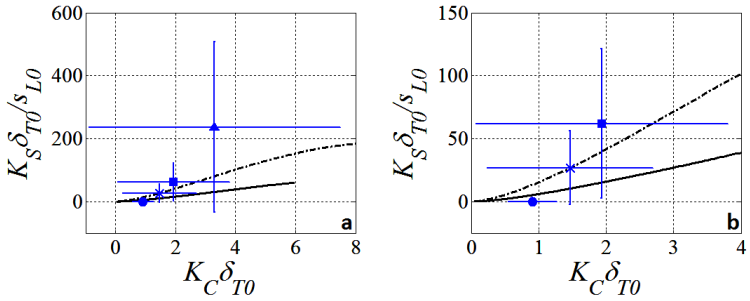


**Figure 3-24. Leading edge mean strain rate $K_S$ plotted against leading edge average mean curvature $K_C$. Figure (b) shows a magnified view of Figure (a) centered on case A31, B31 and C31. Legend is the same as Figure 3-23.**

Figure 3-23a shows that the 1D laminar simulations computed at the average value of mean curvature reasonably follow the enhancement in consumption speed with increasing turbulent intensity and that case D31 seems to approach the highest values of consumption speed and curvature calculated by the model laminar flame computations. This conclusion seems also justified by the data of Figure 3-23c, which show that the decreasing trend in the average thickness of the $H_2$ consumption layer with increasing turbulence levels follows the 1D laminar simulations. Figure 3-23b, however, shows that

the structure of the thermal layer as measured by $\delta_T$ is captured by the 1D simulations up to case B31, while cases C31 and D31 seem to progressively diverge from this solution. This effect is presumably due to the presence flamelets with low curvature ($K_C \sim 0$) at the leading edge, especially at high turbulent intensities, as shown in Figure 3-22. For these flamelets, curvature effects are likely to be less important than strain rate effects, accounting for some of the differences between model laminar computations and statistics obtained from the DNS. In fact, Figure 3-24 shows that for the same values of curvature these case C31 and D31 are characterized by higher strain rates than the model laminar flame computations. To partially eliminate these effects, Figure 3-25 and Figure 3-26 reproduce the results of Figure 3-23 and Figure 3-24 but excluding all the elements that are not cylindrically or spherically shaped, analogously to the analyses presented in Section 3.4.3.1. These figures show that the agreement with the model laminar flame calculations increases especially at higher turbulent intensities. This agreement was not necessarily expected, as it is known that non-steady effects decrease the effective stretch sensitivity of the flame (see Section 2.1.2), and so we had anticipated the DNS results for consumption speed to fall below the laminar calculations (note that although these are "time averaged" leading edge values, the leading edge curvatures for a given flame element are intrinsically unsteady as flame features move in and out of the leading edge interrogation region). This result might be a manifestation of the weak sensitivity of curvature-induced flame speed modifications to frequency, as opposed to its strong sensitivity to nonsteadiness in hydrodynamic stretch [56].

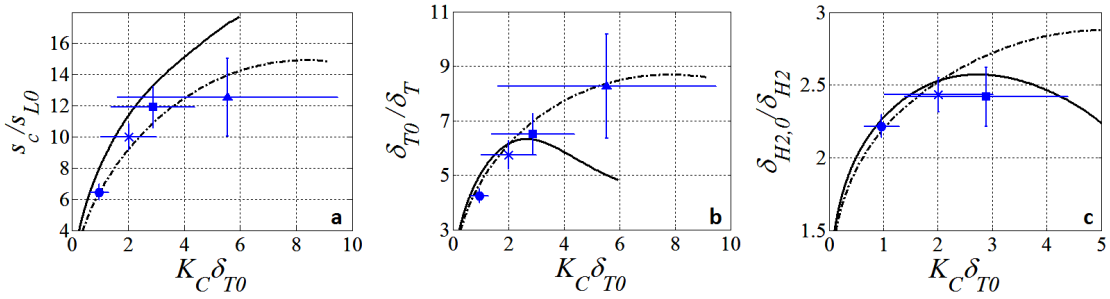


**Figure 3-25. Leading edge mean consumption rate $s_c$ (a), mean of the inverse of flame thickness $\delta_T$ (b) and $\delta_{H2}$ (c) plotted against leading edge average mean curvature $K_C$. Only positions at which the principal curvatures of the $T_{ref} = 1088K$ isosurface are both positive are utilized ($k_1 > k_2 > 0$: cylindrical and spherical elements). Legend is the same as Figure 3-23.**

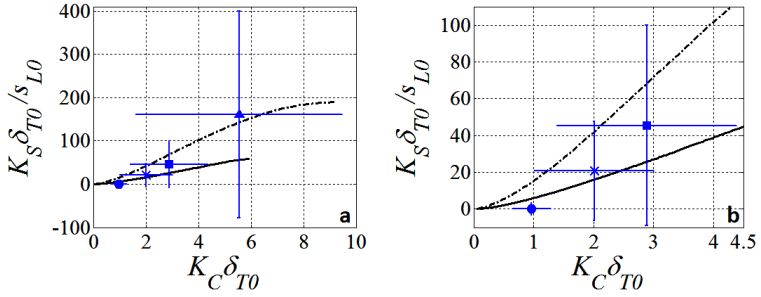


**Figure 3-26. Leading edge mean strain rate $K_S$ plotted against leading edge average mean curvature $K_C$. Only positions at which the principal curvatures of the $T_{ref} = 1088K$ isosurface are both positive are utilized ($k_1 > k_2 > 0$: cylindrical and spherical elements). Figure (b) shows a magnified view of Figure (a) centered on case A31, B31 and C31. Legend is the same as Figure 3-23.**

The figures shown in this section allow some assessment of ideas put forward by leading point concepts. From the data shown in Figure 3-23 and Figure 3-24, it is clear that the overall trend of increasing leading edge mean values of $s_c$, $K_C$ and decreasing $\delta_T$, $\delta_{H2}$ with increasing turbulence levels follows closely the results of model laminar flame computations. The agreement improves when only spherical and cylindrical shapes are considered to compute the leading edge mean values, as shown in Figure 3-25 and Figure

3-26. It is also interesting to notice that the trends described in this section closely mirror those described in Section 3.4.3 (see Figure 3-14, Figure 3-15 and Figure 3-16) for the peak probability of the joint PDFs of cylindrical and spherical flamelets (see also Appendix B.3). Given the ambiguities and configuration-specific nature of $s_{L,max}$, it is difficult to make a precise assessment, but, in terms of orders of magnitude, these comparisons show that curvatures and burning velocities can be similar to those of "critically" stretched laminar flames especially at high turbulent intensities. For the highest turbulent intensity case (case D31), burning rates do appear to approach the computed range of $s_{L,max}$ values. Nonetheless, in Section 3.4, it has been shown that the most highly curved flamelets are subject to compressive strain rates which prevent the flame from becoming too curved for a given level of turbulent intensity and from reaching a critically stretched structure. As described in Section 2.3, this trend arises because for highly curved flamelets the importance of wrinkling and stretching by turbulent eddies is overcome by gas expansion effects. This effect is not present in the 1D model laminar simulations. As a consequence, the flame structure of the most highly curved flamelets for each case is not well described by model laminar flame computations.

## 3.6 Conclusions

This chapter has described a comparison between DNS results of lean, $H_2$/air flames and results from several highly-stretched, model geometries [149]. This type of information is useful for modeling purposes in the framework of the leading points concept and may

also be compared to similar attempts to collapse flame speed data obtained by DNS of turbulent flames using different (planar) laminar flame models [99] (see Section 2.3). For the lean hydrogen/air mixture investigated, it has been shown that the overall trend of increasing $s_c$, $K_C$ and decreasing $\delta_T$ and $\delta_{H2}$ with increasing turbulence levels follows closely the behavior of model laminar flame computations. In particular, at the leading edge the average flame front structure can be reproduced reasonably well by results obtained from model geometries with the same average mean curvature. However, the comparison between model laminar flame computations and highly curved flamelets is complicated by gas expansion across the flame which generates compressive strain rates and prevents the flame from becoming too curved for a given level of turbulent intensity. For the highest turbulent intensity investigated, case D31, local consumption speed, curvatures and flame thicknesses seems to approach the maximum values obtained by the laminar model geometries, while other cases display substantially lower values. This seems to suggest that at low turbulent intensities "critically" stretched flamelets are not a good model for leading points burning rates, at least for the low Reynolds and low Damköhler number accessible by direct numerical simulations. At higher Reynolds number, turbulent vorticity fluctuations tend to be more concentrated in thin region of space, known as "worms" or "vortex tubes", which are a manifestation of the "internal intermittency" of the turbulent flow [150]. It has been postulated that these flow structures are able to wrinkle and distort the flame much more efficiently than what suggested by low Reynolds number computations and, as such, critically stretched flamelets may be relevant also at low $u'/s_{L0}$ [4]. A relation between "vortex tubes" and regions of high heat release rate was for example claimed in the DNS of Tanahashi et al.

[121]. However, this proposed mechanism is difficult to verify computationally because of the large computer resources needed to simulate premixed flames at high Reynolds number [133].

# CHAPTER 4
# LEADING POINTS DYNAMICS

Section 2.4.2 described two model problems which illustrate rather straightforwardly the role of leading points in determining the overall displacement speed of the flame front. The first model problem regards the application of the Kolmogorov-Petrovskii-Piskunov (KPP) theorem to a statistically stationary one dimensional turbulent flame. This characterization of the leading points suffers of several drawbacks (see Section 2.4.2) and is difficult to extend to more complex flow geometries.

The second example that clearly shows the significance of the leading points in uniquely controlling the overall burning velocity is represented by the case of an initially flat flame propagating in a one-dimensional steady shear flow in which the velocity isocontours are parallel to the direction of flame propagation. In this situation, it can be demonstrated that the front displacement speed is controlled by the leading points of the flame that propagate into the lowest approach flow velocity regions ahead of the flame. This latter model problem provides a more geometrical and physically meaningful characterization of the leading points. However, the dynamical significance of the leading points is more difficult to identify in more complex or unsteady flow fields. Following the terminology of Ref. [9, 10], the leading points may no longer be “quasi-steady”, and it is unclear how to apply leading points arguments in this case, or if this approach is even valid.

This chapter takes up this problem in detail in order to examine the dynamical significance of leading points. Specifically, this chapter considers the passive (i.e., with zero heat release) propagation of a premixed flame in a one-dimensional, incompressible, unsteady, periodic shear flow. In this context, it proposes a definition for points that

control the displacement speed of the front, and studies their dynamics. This type of flow configuration has been previously studied as a model problem for flame propagation in inhomogeneous flow fields [151-159]. In particular, we will investigate a specific velocity field which was considered first by Embid *et al.* [160], who presented an exact solution for the front displacement speed. This problem is re-interpreted within the leading points framework in this chapter. Despite representing a rather idealized situation, this model problem provides clues on how to extend leading point ideas to more complex flow fields.

The rest of the chapter is organized in the following manner. Section 4.1 introduces the G-equation, which is utilized as a model for flame front propagation. Section 4.2 presents pertinent results from the theory of Hamilton-Jacobi equations, which, when applied to the G-equation, lead to our proposed mathematical formulation of leading points. These ideas are then applied to a specific shear flow in Section 4.3, chosen because the instantaneous leading points evolve temporally, but also because is amenable to an exact solution. The laminar flame speed $s_L$ is assumed to be constant in Sections 4.2 and 4.3. Section 4.4 then considers generalizations of these results to the case where the burning velocity $s_L$ has a linear dependence on curvature, where the proportionality coefficient is a positive Markstein length, $\ell$. Finally, we conclude in Section 4.5 with a summary of the principal findings.

### 4.1 G-equation

To model the reaction front propagation we utilize the *G-equation*, which was first formulated by F. Williams [161] and is used extensively for various combustion problems such as the theoretical determination of flame transfer functions [162] and turbulent consumption rates [163], as well as in many computational fluid dynamics (CFD) studies [164, 165].

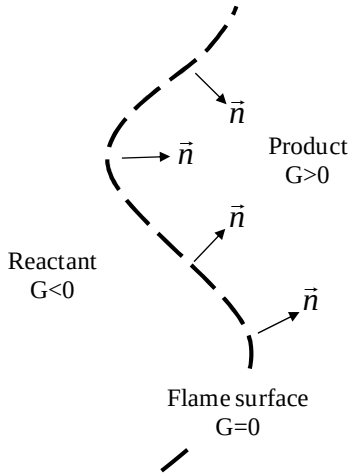


**Figure 4-1. Instantaneous snapshot of a wrinkled laminar flame sheet, whose instantaneous position is given by the parametric equation *G(x, y, z, t)* = 0 [84].**

The G-equation relates the motion of the flame front with various flow/flame parameters. Consider the flame front as a gas dynamic discontinuity in three dimensional space whose position is described by the parametric equation, $G(\vec{x},t) = const$. It is convenient to set $G(\vec{x},t) = 0$ such that $G < 0$ and $G > 0$ for the unburned and burned states, respectively (see Figure 4-1). In a flame-fixed (Lagrangian) coordinate system, the fact that $G(\vec{x},t) = 0$ on the flame implies that:

$$\frac{D}{Dt}G(x,y,z,t)\Big|_{\substack{at\ the\ flame\\ surface}} = 0 \tag{4.1}$$

Converting this expression into an Eulerian form gives:

$$\frac{\partial G}{\partial t} + \vec{v}_F \cdot \nabla G = 0 \tag{4.2}$$

where $\vec{v}_F$ is the velocity of the flame front which can be decomposed into the sum of flow velocity and normal flame propagation speed as $\vec{v}_F = \vec{u} - s_L \cdot \vec{n}$ (see also Section 2.1.1). Note that the normal direction to the flame front can be written as $\vec{n} = \nabla G / \|\nabla G\|$ (see Figure 4-1). Then, Eq. (4.2) can be expressed as:

$$\frac{\partial G}{\partial t} + \vec{u}(\vec{x},t) \cdot \nabla G = s_L \|\nabla G\| \tag{4.3}$$

where the zero level set of the scalar function $G$ represents the flame position, $s_L$ is the laminar flame speed (assumed constant, except in Section 4.4) and $\vec{u}(\vec{x},t)$ is the flow velocity at the flame, which is considered as prescribed. In the combustion literature, equation (4.3) is known as the G-equation and was originally employed to model flame motions in flow fields characterized by length scales much larger than the laminar flame thickness, such as in the wrinkled and corrugated flamelet regime [161]. However as a phenomenological model, the G-equation is rather flexible in that many factors

influencing front motion can be incorporated into $s_L$, making it useful to model flame front motion also in the thin reaction zone regime [57]. Additionally, prescribing the flow field $\vec{u}(\vec{x},t)$ upstream of the flame is equivalent to neglecting gas expansion across the flame and is, as such, rigorously valid only in the limit of low density ratio flames. This is a common assumption made in these types of analyses [151-159] – discussion of its implications can be found in these references.

## 4.2 Problem formulation and mathematical background

### 4.2.1 One dimensional problem formulation

In this chapter we assume a two-dimensional flame front whose location is a single valued function, $\xi$, of the coordinate $x$ (see Figure 4-2). Because of this assumption we can define $G(x,y,t) = y - \xi(x,t)$. Inserting this expression in Eq. (4.3) leads to [144]:

$$\frac{\partial \xi}{\partial t} + u_x(x,t)\frac{\partial \xi}{\partial x} - u_y(x,t) = -s_L\sqrt{1+\left(\frac{\partial \xi}{\partial x}\right)^2} \tag{4.4}$$

Eq. (4.4) is a Hamilton-Jacobi equation, whose convex Hamiltonian is represented by $H = H(x,t,g) = s_L\sqrt{1+g^2} + u_x g - u_y$ where $g = \partial\xi/\partial x$ is the flame slope. The flame slope satisfies the conservation equation associated to eq. (4.4):

$$\frac{\partial g}{\partial t}+\frac{\partial}{\partial x}H\left(x,t,g\right)=0 \tag{4.5}$$

which can be obtained simply differentiating in $x$ Eq. (4.4). In this section, we assume that $u_x$ and $u_y$ are periodic in $(x,t)$ with period $[0,L]\times[0,T]$ and form an incompressible flow field: with this latter assumption, the condition $\nabla\cdot\vec{u}=0$ dictates that $u_x\left(x,t\right)=u_x\left(t\right)$. We are interested in the study of the average front displacement speed at large time, $s_T$, defined as:

$$s_T=-\frac{1}{L}\frac{1}{T}\int_0^L\int_0^T\frac{\partial\xi}{\partial t}\,dx\,dt=\frac{1}{L}\frac{1}{T}\int_0^L\int_0^T H\left(x,t,g\right)dx\,dt \tag{4.6}$$

In the context of multiscale expansions of Hamilton-Jacobi equations, $s_T$ is also referred to as the "homogenized (or effective, or critical) Hamiltonian" (see Appendix C).

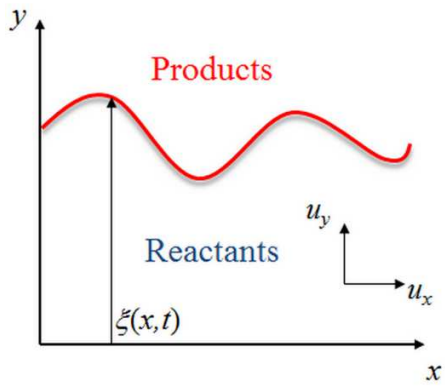


**Figure 4-2. Schematic of a two-dimensional flame whose position is a single valued function of the *x* coordinate.**

Away from discontinuities in the graph of $g$, which are known as "shocks" and represents cusps in the graph of $\xi$, the solution of Eq. (4.5) can be described in terms of characteristic curves. Characteristic curves satisfy the following system of ordinary differential equations:

$$\begin{aligned} a)\quad & \frac{dx}{dt} = \frac{\partial H}{\partial g} = s_L \frac{g}{\sqrt{1+g^2}} + u_x \\ b)\quad & \frac{dg}{dt} = -\frac{\partial H}{\partial x} = \frac{\partial u_y}{\partial x} \end{aligned} \tag{4.7}$$

Solutions of Eq. (4.4) admit also a variational representation, known as the "Lax-Oleinik formula" [166] in the context of partial differential equation theory, "principle of least action" [167] in the context of Hamiltonian dynamical systems theory or "principle of dynamic programming" [168] in control theory, given by

$$\xi(x,t) = \min_{\gamma \in AC,\, \gamma(t)=x} \left\{ \int_{\tau}^{t} \mathcal{L}\left(\gamma(s), s, \dot{\gamma}(s)\right) ds + \xi\left(\gamma(\tau), \tau\right) \right\} \quad \forall \tau < t \tag{4.8}$$

where *AC* represents the set of all Lipschitz continuous paths $\gamma : \mathbb{R} \to \mathbb{R}$ and $L$ is the Lagrangian function (or Legendre transform) associated with the Hamiltonian $H$:

$$\begin{aligned} \mathcal{L}(x,t,\dot{\gamma}) &= \sup_{g} \left( g \cdot \dot{\gamma} - H(x,t,g) \right) = \\ &= \begin{cases} -\sqrt{s_L^2 - \left(\dot{\gamma} - u_x(t)\right)^2} + u_y(x,t) & \text{for } s_L \geq \left|\dot{\gamma} - u_x(t)\right| \\ +\infty & \text{for } s_L < \left|\dot{\gamma} - u_x(t)\right| \end{cases} \end{aligned} \tag{4.9}$$

When the Lagrangian assumes finite values (i.e., for $s_L \geq \left|\dot{\gamma} - u_x(t)\right|$), it can be demonstrated that the characteristic curves are solutions of the minimization problem (4.8), and from Eq. (4.7) we have:

$$\dot{\gamma} = \frac{dx}{dt} = \frac{\partial H}{\partial g} \tag{4.10}$$

Then, from a physical point of view, it can be seen that the Lagrangian represents the propagation speed in the *y*-direction of the points on the flame surface that follows the trajectory of the characteristic curve $\gamma$. As defined in [169], those curves, $\gamma$, which solve Eq. (4.8) on intervals $]-\infty, t]$ are referred to as "one-sided minimizers" and "two-sided" (or global) minimizers if they solve it on intervals $]-\infty, +\infty[$.

In general, the Lagrangian can also achieve infinite values for $s_L < \left|\dot{\gamma} - u_x(t)\right|$. At positions where $s_L = \left|\dot{\gamma} - u_x(t)\right|$ the flame slope $g$ becomes infinite as shown by the equation

$$g = \frac{\partial \mathcal{L}}{\partial \dot{\gamma}} = \frac{\dot{\gamma} - u_x}{\sqrt{s_L^2 - \left(\dot{\gamma} - u_x\right)^2}} \tag{4.11}$$

which is the convex (or Legendre) conjugate of Eq. (4.10). In these instances, Eq. (4.4) loses meaning because the flame position can no longer be represented by a single valued function $\xi$ and the full G-equation (4.3) must be solved to model the front dynamics.

To illustrate the physical meaning of equation (4.8), in the next section we consider a simplified version (the Hopf-Lax formula [166]) valid for problems where the flame propagates into a quiescent flow.

### 4.2.2 Hopf-Lax formula and Huygens propagation

The Hopf-Lax formula [166] is a simplification of Eq. (4.8) valid when the flame propagates into a quiescent flow ($u_x = u_y = 0$). In this situations the governing equation for the flame position, Eq. (4.4), becomes

$$\frac{\partial \xi}{\partial t} = -s_L \sqrt{1+\left(\frac{\partial \xi}{\partial x}\right)^2} \tag{4.12}$$

and the characteristic curves have a constant slope (i.e. $\dot{\gamma} = dx/dt = const$) since $dg/dt = 0$ in equation (4.7). Then, the Lagrangian (Eq. (4.9)) can be written as:

$$\mathcal{L}(\dot{\gamma}) = \begin{cases} +\infty & \dot{\gamma} > s_L \\ -\sqrt{{s_L}^2 - \dot{\gamma}^2} & -s_L \le \dot{\gamma} \le s_L \\ +\infty & -s_L > \dot{\gamma} \end{cases} \tag{4.13}$$

and the general solution Eq. (4.8) becomes the Hopf-Lax formula [166]:

$$\xi(x,t) = \min_{x-s_L t < x^* < x+s_L t} \left( \xi_{init}(x^*) - \sqrt{(s_L t)^2 - (x-x^*)^2} \right) \tag{4.14}$$

where $\xi_{init} = \xi(x, t=0)$ represents the initial position of the flame front. Noticing that the expression between paranteses in eq. (4.14) represents the equation of a circle, this solution simply states that the flame propagates in every radial direction from all points on flame fronts $\left(x^*, \xi_{init}\left(x^*\right)\right)$ with a speed equal to $s_L$. To illustrate, Figure 4-3 shows the instantaneous flame location at two instances of time, $t = 0$ and $dt$. The dashed lines indicate circles of radius $s_L dt$, centered at points on the flame fronts at $t = 0$. The flame position at later times can be constructed geometrically by drawing such circles about every point along the flame at each time, as shown in Figure 4-3. This process is also referred to as "Huygens propagation" (see Ref. [66]). If the flame is curved, different points influence the flame propagation in different ways. For example, some concave regions do not contribute at all in determining the flame front position at later times (point D) as its propagation is overshadowed by propagation from neighboring points (points C and E). In other words, only convex regions are important in determining the position of the flame front in the large time limit.

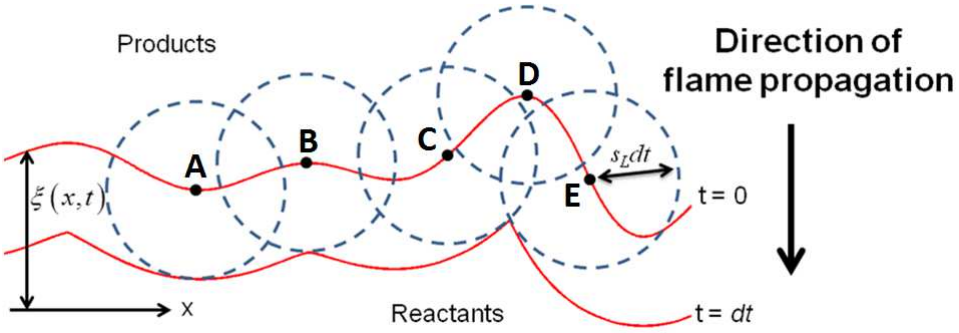


**Figure 4-3. Sketch illustrating Huygens propagation (Hopf-Lax solution for flame propagation).**

### 4.2.3 Aubry-Mather theory

Let us first consider a multidimensional autonomous Hamilton-Jacobi equation

$$\frac{\partial \varphi}{\partial t} + H\left(\vec{x}, \nabla \varphi\right) = 0 \quad \vec{x} \in \mathbb{R}^n \tag{4.15}$$

where the Hamiltonian function $H$ is smooth, convex in the $\nabla \varphi$ variable, is periodic in $\vec{x}$ with period $[0,1]^n$ and satisfies the so called coercivity condition:

$$\lim_{\|\nabla \varphi\| \to +\infty} H\left(\vec{x}, \nabla \varphi\right) = +\infty \tag{4.16}$$

With these assumptions, it is possible to prove that among the characteristic curves associated with Eq. (4.15) there always exist global minimizers (i.e., characteristic curves that exists on time interval $]-\infty, +\infty[$) and that the long time behavior of the solutions of Eq. (4.15) is completely determined by their trajectories [170, 171]. For the one dimensional problem considered in Section 4.2.1, the coercivity condition is satisfied for $|u_x| < s_L$ when the flow field is time independent, which is also a sufficient condition to prevent the flame slope from becoming infinite ($g < \infty$) for any solution of Eq. (4.4), given sufficiently regular initial conditions [171]. In this situation, global minimizers $\gamma^*$ exist and the front speed $s_T$ can be expressed just in terms of their trajectories as [172]

$$\begin{aligned} s_T &= -\frac{1}{T}\int_0^T \mathcal{L}\left(\gamma^*(t), t, \dot{\gamma}^*(t)\right) dt \\ &= -\frac{1}{T}\int_0^T \left( -\sqrt{s_L^2 - \left(\dot{\gamma}^*(t) - u_x\right)^2} + u_y\left(\gamma^*(t)\right)\right) dt \end{aligned} \tag{4.17}$$

To understand, the physical meaning of these results it is useful to visualize the global minimizers in the $x-t$ plane. Let us return to the problem considered in Section 2.4.1 - an initially flat flame, $\xi(x,0)=g(x,0)=0$, propagating in a steady periodic flow field, $u_y=-A\cos(2\pi x/L)$, with no transverse flow, $u_x=0$. In this case, the characteristic curves can be obtained by solving Eq. (4.7) analytically [153]. Figure 4-4 plots the temporal evolution of $g$ and $\xi$ for $A/s_L=0.5$. It can be seen that, after an initial transient, the solution develops a shock in the graph of $g$ (a cusp in the graph of $\xi$) at $x/L=0.5$, which grows until the steady state is reached. The characteristic curves of these solutions are plotted in the $x-t$ plane in Figure 4-5. Note that the only trajectories that are never absorbed by the shock correspond to the positions where $u_y$ is minimum. These trajectories represent the global minimizers and, from Eq. (4.17), the front displacement speed can be readily obtained as

$$s_T=A+s_L \tag{4.18}$$

The *characteristic curve trajectories that are global minimizers uniquely determine the large-time behavior of the flame propagation*. The points on the flame front that follows these trajectories can also be seen as the points that propagate most quickly in the *y*-direction and, in a sense, they represent the "optimal" solutions in the variational problem (4.8) [172]. In contrast, the dynamics of the one-sided minimizers, which form the "domain of attraction" of the shock [173], determines the overall shape of the flame (as

will become clearer in the next section), but do not provide any information about the large-time front displacement speed.

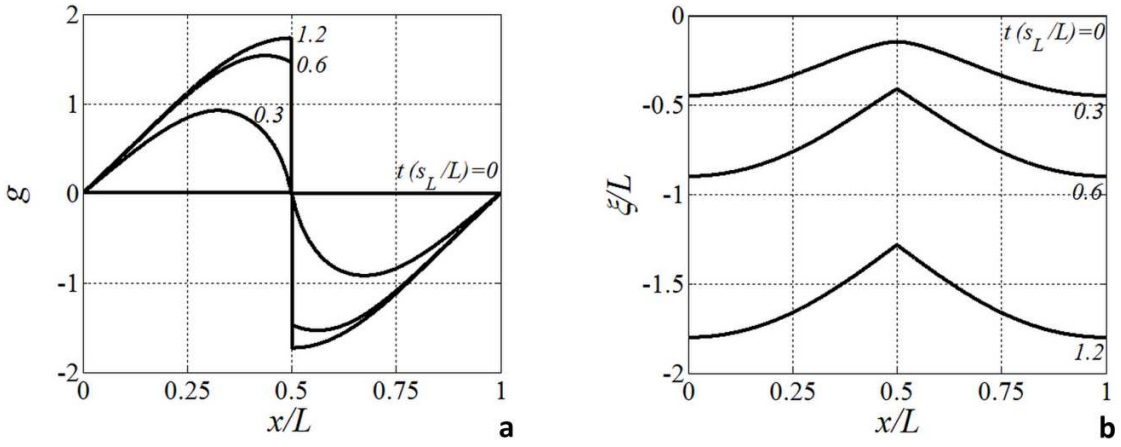


**Figure 4-4. Flame slope $g$ (a) and flame shape $\xi$ (b) at different normalized times $t\left(s_L/L\right)$ for the flow field $u_y = -A\cos\left(2\pi x/L\right)$, $u_x = 0$ with $A/s_L = 0.5$.**

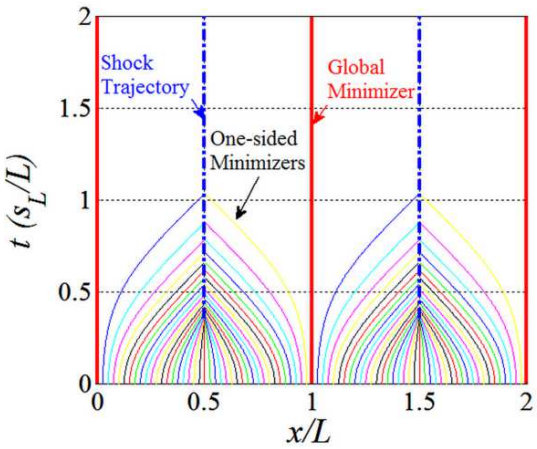


**Figure 4-5. Characteristic curves in the $x$-$t$ plane for the solutions showed in Figure 4-4. One-sided minimizers are represented by variously colored thin lines, global minimizers by thick red lines and the shocks trajectories by thick blue dot-dashed lines.**

The existence of global minimizers is not guaranteed in general for the G-equation. In fact, its Hamiltonian $H\left(x,\nabla G\right) = s_L\left|\nabla G\right| - \vec{u}\left(x\right)\cdot\nabla G$, does not satisfy Eq. (4.16) for a

mean-zero velocity field $\vec{u}(x)$ which changes sign and has amplitude larger than the laminar flame speed $s_L$ [174]. From a physical point of view, the lack of coercivity means that the propagation of the flame front is dominated by stirring and convection and it is possible that certain flow profiles may "block" all characteristic curves and prevent them from existing on time intervals $]-\infty,+\infty[$ (i.e., prevent it from being a global minimizer). A two dimensional example of this situation is the so called "cellular flow" whose stream function is given by $\psi = A\sin x \sin y$ (with $u_x = \partial\psi/\partial y$, $u_y = -\partial\psi/\partial x$) with $A >> s_L$ [175]. A sketch of the streamlines and velocity vectors of this flow field are shown in Figure 4-6. As it can be observed all the streamlines form closed periodic paths and for sufficiently high flow velocities ($A >> s_L$) they impede the motion of the characteristic curves [175].

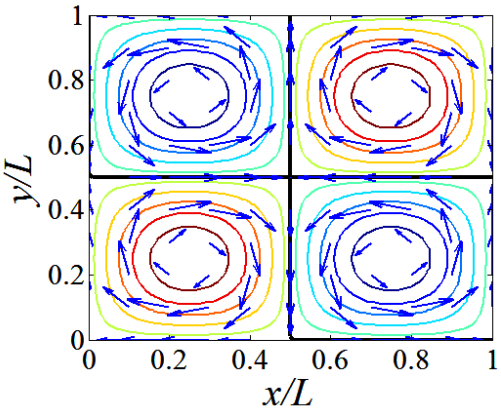


**Figure 4-6. Streamlines (thick lines) and velocity vectors (arrows) for the cellular flow.**

However, for this flow field some success in studying front displacement speeds trends has been made by considering "least time" trajectories [176] or local "action minimizing"

trajectories [177], which seem to have analogies to the global minimizers but in a local setting. Thus, it is conceivable that investigating the dynamics of global minimizers in situations in which they exist can still be of relevance to understand more general flows.

For time-dependent Hamiltonians, the coercivity condition is no longer sufficient to ensure the existence of global minimizers. A stronger assumption on the Hamiltonian that guarantees the existence of global minimizers is the so called superlinearity

$$\lim_{\|\nabla\varphi\|\to+\infty} \frac{H\left(\vec{x},t,\nabla\varphi\right)}{\left\|\nabla\varphi\right\|} = +\infty \tag{4.19}$$

An example of Hamiltonian satisfying this conditions, is the "classical" Hamiltonian $H\left(\vec{x},t,\nabla\varphi\right) = \left\|\nabla\varphi\right\|^2/2 + F\left(\vec{x},t\right)$ (where $\left\|\nabla\varphi\right\|^2/2$ represents the kinetic energy and $F\left(\vec{x},t\right)$ the potential energy) whose associated conservation equation (similar to Eq. (4.5)) is

$$\frac{\partial\vec{v}}{\partial t} + \left(\vec{v}\cdot\nabla\right)\vec{v} = -\nabla F\left(\vec{x},t\right) \tag{4.20}$$

where $\vec{v} = \nabla\varphi$ and is referred to as the "forced inviscid Burgers equation" [178]. On the contrary, the Hamiltonian of the G-equation is of the "relativistic" type [179] and is not superlinear. Note that the G-equation reduces to this forced Burgers equation in the limit of small flow fluctuations [153, 180].

### 4.2.4 Definition of Aubry-Mather Leading Points

Based on the theory described in the previous section, we concentrate first on steady flow fields for which the coercivity condition Eq. (4.16) is satisfied. In this context, we define "Aubry-Mather points" as those parts of the flame whose propagation follows the trajectories of the global minimizers. Note that the global minimizers may not be isolated trajectories and, as such, they may not be discrete points on the flame as the name "leading points" seems to suggest. For instance, if in the example of Figure 4-4 and Figure 4-5 we had chosen a function with degenerate (i.e., with zero second derivative) absolute minima to represent the steady shear flow profile, then the trajectories of the global minimizers could originate from a continuous band of spatial positions. In the context of the Hamiltonian dynamical system defined by equations (4.7), when the trajectories of the global minimizers are isolated from each other, they are also known as "hyperbolic trajectories" [167]. When the system is autonomous (i.e., the velocity flow field does not depend explicitly on time), they may be also referred to as "hyperbolic fixed (or equilibrium) points", since they are equilibrium points for the characteristic curves in Eq. (4.7). In the case of a flame propagating in a unidirectional steady shear flow ($u_y = f(x),\ u_x = 0$), it can be shown that the Aubry-Mather points are hyperbolic points (i.e., a finite number of isolated points) only if $f(x)$ possesses a finite number of non-degenerate absolute minima for $x \in [0, L]$. Thus, this analysis suggests a third potential leading point definition, which we refer to as the "Aubry-Mather Leading points", as those parts of the flame that follows the trajectories of global minimizers, in the case these are hyperbolic trajectories. These are the discrete points on the flame that control its propagation speed.

### 4.3 Example problem

In this section, we consider a flame propagating in a periodic steady shear flow $u_y = f(x)$ with a constant mean transverse wind $u_x = V \geq 0$. Eq. (4.4) admits an analytical solution [160] for this flow field, which is reproduced in Appendix C. With a change in coordinate system, this problem is also equivalent to a flame propagating at an angle of $\theta = \tan^{-1}(V/s_T)$ to the velocity isocountours of $u_y$. In this framework, the mean transverse wind $V$ can be interpreted as a parameter of the "unsteadiness" of the axial flow $u_y$ since in a reference frame attached to the transverse flow (moving in the *x*-direction with velocity $V$) the Galilean transformations

$$\begin{aligned} x' &= x + Vt & u_x' &= u_x - V = 0 \\ t' &= t & u_y' &= u_y \end{aligned} \tag{4.21}$$

eliminates the transverse mean flow, with the shear flow now being time dependent $u_y'(x,t) = f(x' - Vt')$. In this new reference frame, the shear is therefore acting on the flame with a time-scale given by $L/V$, where $L$ is the spatial period of $u_y(x)$. The competition between this time scale and the time scale associated with flame propagation, which can be taken as proportional to $L/s_L$, generates rich and interesting behavior [158]. In fact, the rate at which the front displacement speed $s_T$ is enhanced by increasing flow intensity $A$ is reduced as the unsteadiness $V$ grows, analogous to one of the mechanism leading to the "bending effect" discussed in the turbulent combustion literature [156].

In order to demonstrate several points about the characteristics of the global minimizers, we consider two periodic flow fields: one consisting of a single harmonic

$$u_y(x) = -A\cos(2\pi x/L) \tag{4.22}$$

and one with multiple harmonics

$$\begin{aligned} u_y(x) = -\frac{A}{\Delta}\Bigg[ &\cos\left(2\pi\frac{x}{L}\right) + \frac{1}{2}\sin\left(2\pi\frac{x}{L}\right) + \frac{1}{2}\cos\left(4\pi\frac{x}{L}\right) + \\ &+ \frac{1}{2}\cos\left(6\pi\frac{x}{L}\right) - \frac{1}{4}\sin\left(6\pi\frac{x}{L}\right) + \frac{1}{2}\cos\left(8\pi\frac{x}{L}\right)\Bigg] \end{aligned} \tag{4.23}$$

where $\Delta$ is a suitable normalization factor so that the expression in square parentheses has unit amplitude. The latter shear flow (4.23) is considered here as it was also used in references [160, 181] as an example of a profile with a complex structure and an asymmetrical form with multiple local maxima and minima. Figure 4-7 shows a sketch of the shear profiles (4.22) and (4.23).

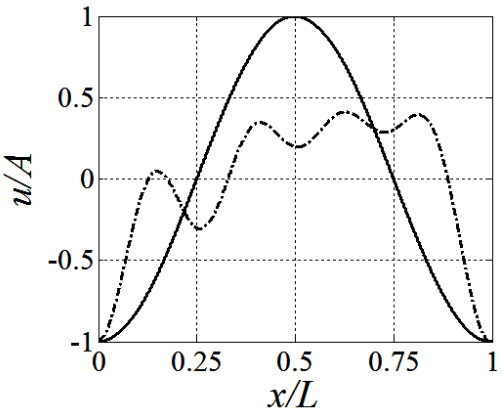


**Figure 4-7. Shear flow profiles given by equation (4.22) (solid line) and equation (4.23) (dot dashed line).**

Figure 4-8a shows the dependence of $s_T$ on the shear flow amplitude $A$ for both profile (4.22) and (4.23) at different values of "unsteadiness parameter", $V$. Its inhibiting effect is illustrated by the fact that when no unsteadiness is present ($V = 0$) $s_T$ depends linearly on $A$, and is given by Eq. (4.18) for both shear flow profiles, while the front displacement speed monotonically decreases for increasing $V$. Figure 4-8b replots these same data in terms of normalized enhancement of the displacement speed $(s_T - s_L)/A$ in order to better illustrate this effect. Here, the significance of increasing $V$ on decreasing the displacement speed is clearly shown. At large enough values of $V$, $s_T$ always asymptotes to $s_L$. However, $s_T$ exceeds $s_L$ for a larger range of $V$ values with increasing amplitude, $A$.

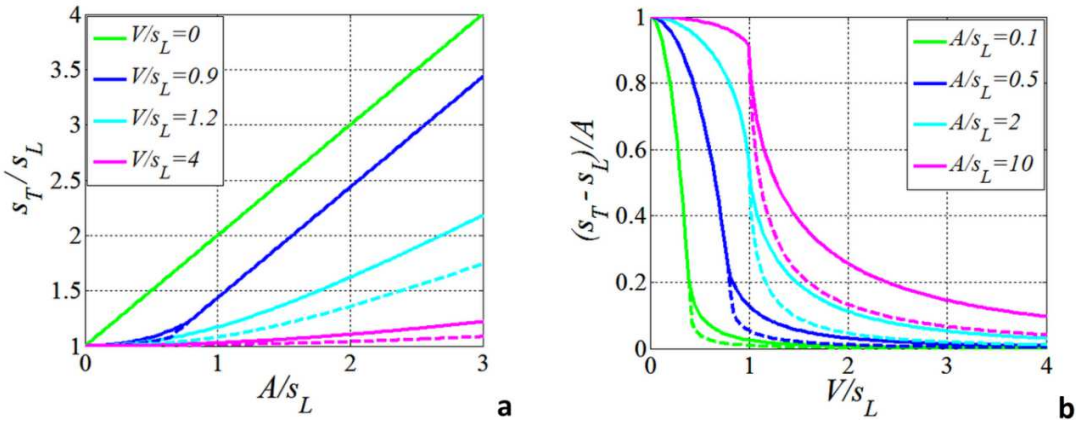


**Figure 4-8. Dependence of front displacement speed $s_T$ on shear flow amplitude $A$ for fixed unsteadiness parameter $V$ (a). Normalized enhancement of displacement speed $(s_T - s_L)/A$ as a function of unsteadiness parameter $V$ at fixed shear flow amplitude $A$ (b). Solid lines refer to the shear flow profile (4.22) while dashed lines refer to the shear flow profile (4.23).**

The classical interpretation of these effects is in terms of flame area. To illustrate, Figure 4-9 plots flame shapes at the steady state for a fixed shear flow amplitude ($A/s_L = 0.5$) and different values of transverse wind intensity. It can be observed how the overall flame area decreases as the unsteadiness parameter $V$ increases. However, this explanation does not clarify why, for certain values of $A$ and $V$, the front displacement speed is identical for the two shear flow configurations, while it is different for other combination of $A$ and $V$. Specifically, Figure 4-8 shows that $s_T$ values are different for the two shear flow profiles (i.e., dashed and solid lines are not superimposed) for large values of unsteadiness $V$.

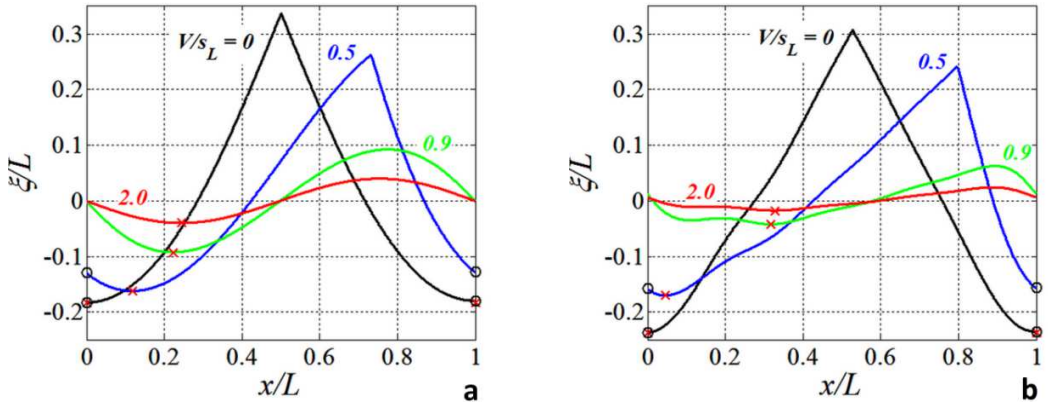


**Figure 4-9. Flame shape $\xi$ for $A/s_L = 0.5$ and different values of $V/s_L$ for both profile (4.22) (a) and profile (4.23) (b). The graphs of $\xi$ are adjusted so that their average is zero. "Aubry-Mather leading points" are indicated by black circles (which only exist for the $V/s_L$ = 0 and 0.5 cases); "instantaneous leading points" are indicated by red crosses.**

We now show that the differences in the occurrence of the inhibiting effect between shear flow profile (4.22) and (4.23) can be interpreted in terms of the dynamics of global minimizers (i.e., in terms of the "Aubry-Mather leading points"). First we remark that both profiles (4.22) and (4.23) have only one absolute minimum per period at points where $u_y = -A$. The equilibrium points of the characteristic curves (4.7) for these velocity flow fields are given by

$$\begin{cases} \dfrac{dx}{dt} = s_L \dfrac{g}{\sqrt{1+g^2}} + V = 0 \\ \dfrac{dg}{dt} = \dfrac{du_y}{dx} = 0 \end{cases} \rightarrow \begin{cases} \overline{x} = \left( x \in \mathbb{R} : \dfrac{du_y}{dx} = 0 \right) \\ \overline{g} = -\dfrac{V}{\sqrt{s_L^2 - V^2}} \end{cases} \tag{4.24}$$

and can be classified as hyperbolic (or saddle) fixed points when $d^2u_y/dx^2 > 0$ (local minimum of $u_y$), elliptic (or centers) when $d^2u_y/dx^2 < 0$ (local maximum of $u_y$) and non-hyperbolic (or non-isolated) when $d^2u_y/dx^2 = 0$ [182]. According to the discussion in the previous section then, for $V = 0$ the solution of Eq. (4.4) possesses a unique hyperbolic global minimizer per period whose position coincides with the hyperbolic fixed point in correspondence of the absolute minimum in velocity.

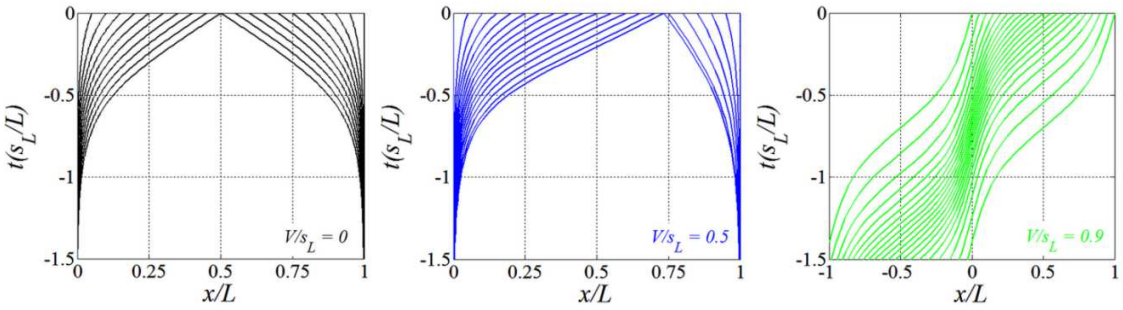


**Figure 4-10. Backward characteristic curves in the $x$-$t$ plane corresponding to the solutions shown in Figure 7a (shear flow profile of equation (4.22) with $A/s_L = 0.5$ and $V/s_L = 0$ (a), $V/s_L = 0.5$ (b), $V/s_L = 0.9$ (c)).**

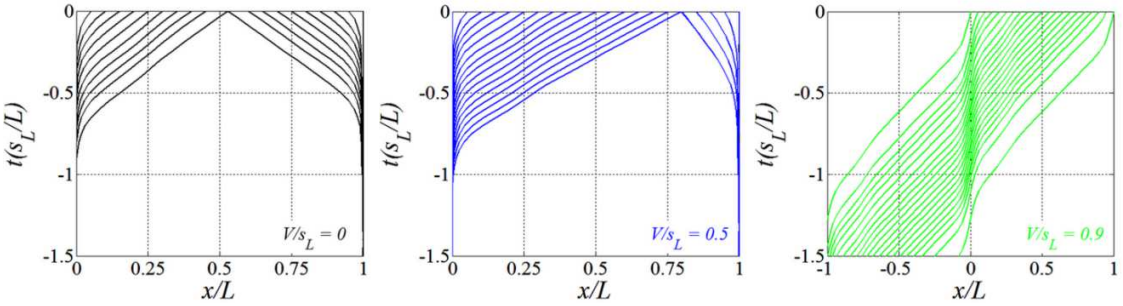


**Figure 4-11. Backward characteristic curves in the $x$-$t$ plane corresponding to the solutions shown in Fig. 7b: shear flow profile of Eq. (4.23) with $A/s_L = 0.5$ and $V/s_L = 0$ (a), $V/s_L = 0.5$ (b), $V/s_L = 0.9$ (c).**

A convenient way to visualize the global minimizers in the $x-t$ plane is to solve the equations (4.7) backward in time since all the characteristic curves (one-sided minimizers) converge to the global minimizers for $t \to -\infty$ [169, 183]. Figure 4-10 and Figure 4-11 illustrate these backward characteristic curves for the solutions plotted in Figure 4-9. Figure 4-10a and Figure 4-11a show that when no unsteadiness in the flow is present ($V/s_L = 0$) all the one-sided minimizers converge to the global minimizers for both shear flow profiles. Then, from Eq. (4.17), it is clear that both profiles yield the same front displacement speed since $\max\left(-u_y\right) = A$. This conclusion is not influenced by the trajectories of the one-sided minimizers which determine the details of the flame shape and depend on the form of the shear flow profile $u_y$. From Figure 4-10b and Figure 4-11b, it is clear that a limited amount of "unsteadiness" in the flow does not alter the trajectory and the hyperbolic character of the global minimizers. In this case, the front displacement speed and its "bending" with increasing $V$ are the same for both shear flows. Examining the flame shapes plotted in Figure 4-9 for $V/s_L = 0.5$, it also interesting to notice that the discrete global minimizer trajectory does not correspond to the most forward-lying position of the flame – *i.e., the "Aubry-Mather leading points" and the "instantaneous leading points" do not coincide*. In other words, the points controlling the front displacement speed are not the most forward-lying position of the flame front in the direction of the reactants.

A bifurcation in solution characteristics occurs when the unsteadiness parameter, $V$, reaches a critical value. For example, in Figure 4-10c and Figure 4-11c *all* the trajectories are global minimizers and their hyperbolic character is lost. In this case, the trajectories of the global minimizers depend on the spatial details of the shear flow structure, and the

two profiles (4.22) and (4.23) yield different values of front displacement speed according to Eq. (4.17). This is better illustrated in the phase space $g$-$x$ associated with the system of equations (4.7) shown in Figure 4-12. In this figure, for the shear flow profile (4.22), several orbits are plotted as thin lines, the fixed points given by Eq. (4.24) are represented by thick dots and the slope $g$ of the flame shapes of Figure 4-9a are represented by thick lines. As it can be observed for $V/s_L = 0.9$ the hyperbolic fixed points do not belong to the steady state solution, while for $V/s_L = 2$ no fixed point is present among the orbits of the characteristic curves.

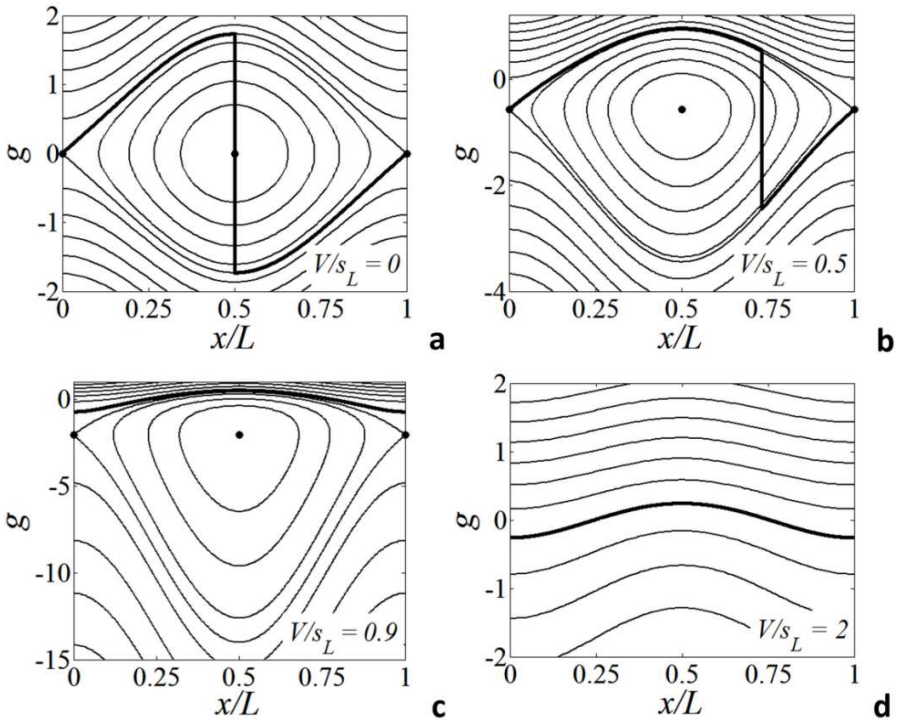


**Figure 4-12. Phase space $g$-$x$ associated with the characteristic curves of shear flow profile (4.22) with $A/s_L = 0.5$ and $V/s_L = 0$ (a), $V/s_L = 0.5$ (b), $V/s_L = 0.9$ (c) and $V/s_L = 2$ (d) . Thin lines represent orbits of the characteristic curves, thick lines represent the steady state solution and dots represent fixed (equilibrium) points.**

From the analytical solution shown in Appendix C, it is then possible to solve for the parameter values $A$ and $V$ where the hyperbolic fixed points do not belong to the steady state solution of Eq. (4.4), as plotted in Figure 4-13. The figure shows that for $V > s_L$ the unsteadiness is too high and no fixed points are present for all values of $A$. At low $A$ values, the fixed point can be lost even at lower values of $V$. This situation mirrors the trends shown in Figure 4-8.

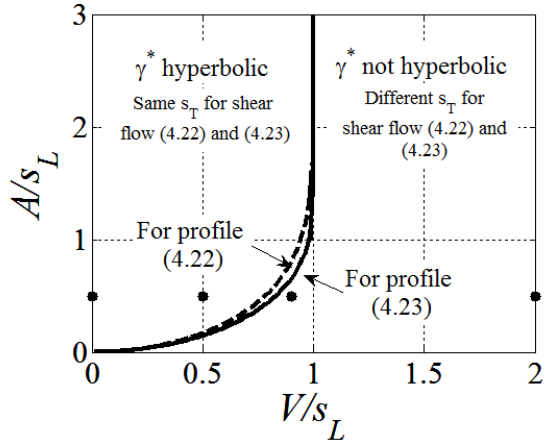


**Figure 4-13. Parameter space $A$-$V$ divided into regions in which solutions of the model problem admit and do not admit hyperbolic global minimizers $\gamma^*$. Dots indicate the conditions at which solutions plotted in Figure 4-9 are obtained ($L = 1$).**

Two key results emerge from this section. First, under certain conditions, the front displacement speed is controlled by velocity field characteristics at discrete points on the flame, points we define as "Aubry-Mather leading points". However, these points do not generally lie on the farthest forward point of the front (the "instantaneous leading point"). Under these conditions, the two totally different velocity fields with the same minimum value lead to identical front displacement speeds. Second, for other conditions, the front displacement speed is not controlled by discrete points, but rather by the entire spatial

distribution of the velocity field. For these conditions, the “instantaneous leading points” do not have any dynamical significance in controlling the front displacement speed. The extent to which these two results modify proposed leading point arguments as articulated in the Section 2.4 remains to be seen, however, as care must be exercised in translating results from this deterministic problem to the ensemble average characteristics of the stochastic problem that is of interest for the turbulent problem [184].

### 4.4 Curvature effects

The previous section considered the case where the laminar burning velocity $s_L$ was constant. In reality, for mixtures with non-zero Markstein lengths it is well known that the laminar burning velocity is a function of the flame stretch rate that, in turn, is a function of the local flow shear and flame curvature (see Section 2.1). As shown in Chapter 3, DNS studies of turbulent premixed flames show that local changes of flame speed correlate strongly with the local curvature of the flame front [4, 60]. In this section, we incorporate a curvature sensitivity into the burning velocity, by means of the following linear expression (see eq. (2.9)):

$$s_L = s_{L0}\left(1-\ell K_C\right) = s_{L0}\left(1-\ell\frac{\partial^2\xi/\partial x^2}{\left(1+\left(\partial\xi/\partial x\right)^2\right)^{3/2}}\right) \tag{4.25}$$

where $s_{L0}$ represents the laminar unstretched flame speed, $\ell$ is the Markstein length and $K_C$ represents the curvature, defined as in Chapter 3. Let us first consider weak curvatures (i.e., small amplitude of wrinkling relative to the transverse length scale of wrinkling), for which this expression can be linearized and, when inserted into the G-equation, yields an additional "viscous" term [185]:

$$\frac{\partial \xi}{\partial t} + u_x \frac{\partial \xi}{\partial x} - u_y = -s_{L0}\sqrt{1+\left(\frac{\partial \xi}{\partial x}\right)^2} + s_{L0}\ell \frac{\partial^2 \xi}{\partial x^2} \tag{4.26}$$

In this section, we consider only positive Markstein lengths $\ell > 0$ (i.e., thermo-diffusionally stable flames). From a physical point of view, the viscous term can be interpreted as a diffusion effect that "blurs" the otherwise "sharp" trajectory of the global minimizer. Indeed, Eq. (4.26) admits a variational solution that is quite similar to Eq. (4.8), but with white noise addition [179, 186]:

$$\xi(x,t) = \min_Y E\left\{\int_\tau^t \mathcal{L}\left(r(s),\dot{\eta}(s),s\right)ds + \xi\left(r(\tau),\tau\right)\right\} \tag{4.27}$$

where $r$ solves for $\tau < s \le t$ the stochastic differential equation

$$\begin{cases} \mathrm{d}r(s) = Y\left(r(s),s\right)\mathrm{d}s + \sqrt{2s_{L0}\ell}\,\mathrm{d}w(s) \\ r(t) = x \end{cases} \tag{4.28}$$

and $Y$ varies in the class of smooth, time dependent functions, $\dot{\eta}(s) = Y(r(s), s)$, $w$ represents a one dimensional Wiener process and $E$ denotes the expectation with respect to the Wiener measure. If we call $Y_\ell$ the minimal $Y$ in Eq. (4.27) and $r_\ell$ the solution of the corresponding stochastic differential Eq. (4.28) then it is possible to obtain a formula analogous to Eq. (4.10) [186]

$$\dot{\eta}_\ell(s) = Y_\ell(x, s) = \frac{\partial}{\partial g} H(x, s, g) \tag{4.29}$$

Despite being presented here for the one dimensional case, we remark that the stochastic variational representation can be extended to the three dimensional viscous G-equation, as described in Ref. [179].

It seems intuitive to expect that the strength of the Markstein length effect depends on the behavior of $\partial^2 \xi / \partial x^2$ along the global minimizers trajectories (i.e., the behavior of the "curvature" at the leading points). If the set of global minimizers for the inviscid problem consists of a finite number of hyperbolic trajectories in each period, then it can be shown that this intuitive physical picture is indeed correct. Let us define the large-time average value of $\partial^2 \xi / \partial x^2$ following the *i*-th global minimizer for the inviscid problem as

$$C_i \equiv \frac{1}{T} \int_0^T \frac{\partial^2}{\partial x^2} \xi\left(\gamma_i^*(s), s\right) ds \tag{4.30}$$

and assume that, among all the global minimizers, there exist only one $C_I = \min_i C_i$ per period. Then, it can be demonstrated that [187-189]

$$\frac{1}{s_{L0}} \lim_{\ell \to 0} \frac{\partial s_T}{\partial \ell} = -C_I \tag{4.31}$$

To illustrate, we consider the effect of the viscous term for the model problem described in Section 4.3 for shear flow (4.22) and (4.23) in the $A-V$ parameter space where the solution possesses a unique, hyperbolic global minimizer per period (see Figure 4-13). Using the analytical solution in Eq. (C.7), the values of $C_I$ for both profiles are given by:

$$\begin{aligned} C_I &= \frac{s_{L0}}{\left(s_{L0}^2 - V^2\right)^{3/4}} \sqrt{\frac{\partial^2 u_y}{\partial x^2}\left(x = \gamma^*\right)} \\ &= \begin{cases} \dfrac{2\pi}{L} \dfrac{s_{L0}\sqrt{A}}{\left(s_{L0}^2 - V^2\right)^{3/4}} & \text{shear flow (4.22)} \\ 2.495 \dfrac{2\pi}{L} \dfrac{s_{L0}\sqrt{A}}{\left(s_{L0}^2 - V^2\right)^{3/4}} & \text{shear flow (4.23)} \end{cases} \end{aligned} \tag{4.32}$$

This expression clearly shows the inhibiting effect that a positive Markstein length has on the front displacement speed. This result is well known from measurements of turbulent flame speeds of lean, heavy fuels [4, 7]. The effect of the curvature term is stronger for the shear flow (4.23), since the absolute minimum at $x = \gamma^*$ is sharper.

This $\ell / L \ll 1$ result can be compared to more general solutions by solving Eq. (4.26) numerically. The computational scheme discretized first order spatial derivatives in Eq.

(4.26) using a fifth-order WENO scheme [190] and a central sixth-order scheme for the viscous term. A Total Variation Diminishing (TVD), third order Runge–Kutta scheme [191] was used for time integration and the Local Lax-Friedrich (LLF) scheme was used for improved stability [190]. Comparison between the numerical computation of $s_T$ and the asymptotic result in Eq. (4.31) is shown in Figure 4-14 for different values of *A* and *V*. These results show that equations (4.31)-(4.32) exactly captures the dependence of $s_T$ upon $\ell$ for $\ell/L \ll 1$, especially when the value of $\partial^2\xi/\partial x^2$ at the leading point is not too high (such as for shear flow (4.22) in Figure 4-14a). For high values of $\partial^2\xi/\partial x^2$, the dependence of $s_T$ on $\ell$ becomes nonlinear, and the linearized approximation loses accuracy.

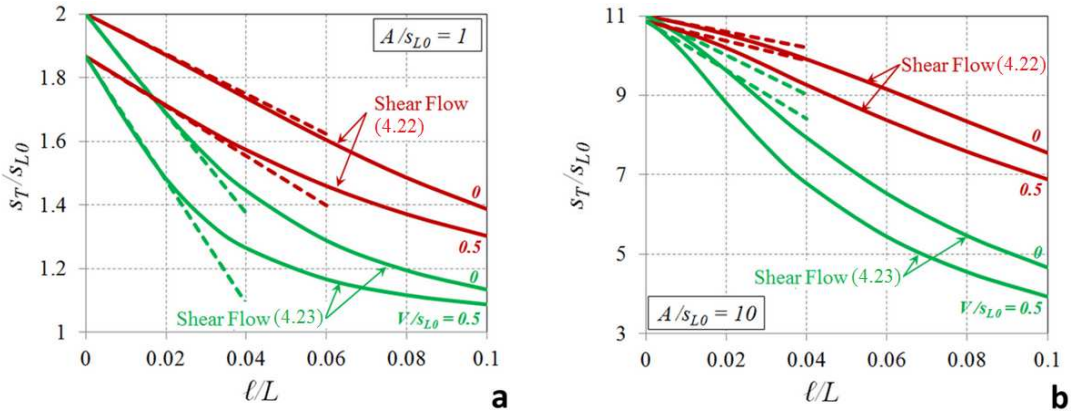


**Figure 4-14. Front displacement speed $s_T$ dependence on Markstein length $\ell$ for $A/s_L = 1$ (a), $A/s_L = 10$ (b) and different $V$ values for the model problem of Section 4.3. Solid lines refer to numerical solutions of Eq. (4.26), dashed lines to the linear approximation (4.31)-(4.32).**

Analogous results are valid when the weak curvature assumption is removed and the full curvature expression is used in Eq. (4.26), which becomes

$$\frac{\partial \xi}{\partial t}+u_x\frac{\partial \xi}{\partial x}-u_y=-s_{L0}\sqrt{1+\left(\frac{\partial \xi}{\partial x}\right)^2}+s_{L0}\ell\frac{\partial^2\xi/\partial x^2}{1+\left(\partial\xi/\partial x\right)^2} \tag{4.33}$$

The last term in Eq. (4.33) is a second order elliptic operator (see p.260 in [192]) which can be considered a generalization of the Laplacian (i.e., the viscous term in Eq. (4.26)). It is possible to prove that the same theory presented above is valid when the viscous term is substituted by any second order elliptic operator (see Remark 6 in [188]). Eq. (4.31) is still valid but with $C_i$ now given by

$$C_i \equiv \frac{1}{T}\int_0^T \frac{\frac{\partial^2}{\partial x^2}\xi\left(\gamma_i^*(s),s\right)}{1+\left(\frac{\partial}{\partial x}\xi\left(\gamma_i^*(s),s\right)\right)^2}ds \tag{4.34}$$

which is the averaged flame curvature computed following the *i*-th global minimizer for the inviscid problem. Using the analytical solution, Eq. (C.7), the value of $C_I$ for the model problem of Section 4.3 is now given by:

$$\begin{aligned} C_I &= \frac{\left(s_{L0}^2-V^2\right)^{1/4}}{s_{L0}}\sqrt{\frac{\partial^2 u_y}{\partial x^2}\left(x=\gamma^*\right)} \\ &= \begin{cases} \dfrac{2\pi}{L}\dfrac{\left(s_{L0}^2-V^2\right)^{1/4}}{s_{L0}}\sqrt{A} & \text{shear flow (4.22)} \\ 2.495\dfrac{2\pi}{L}\dfrac{\left(s_{L0}^2-V^2\right)^{1/4}}{s_{L0}}\sqrt{A} & \text{shear flow (4.23)} \end{cases} \end{aligned} \tag{4.35}$$

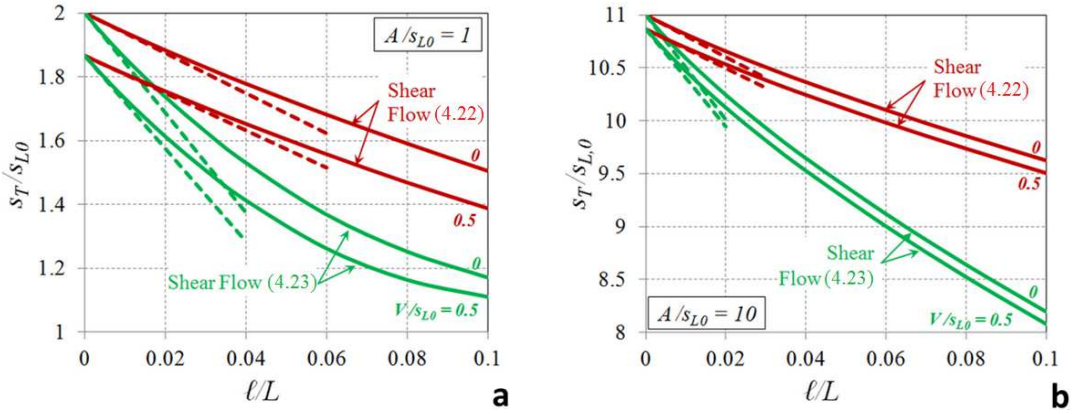


**Figure 4-15. Front displacement speed $s_T$ dependence on Markstein length $\ell$ for $A/s_L = 1$ (a), $A/s_L = 10$ (b) and different $V$ values for the model problem of Section 4.3. Solid lines refer to numerical solutions of Eq. (4.33), dashed lines to the linear approximation of Eq. (4.31)-(4.35).**

Analogously to Figure 4-14, Figure 4-15 compares equations (4.31)-(4.35) with the value of $s_T$ computed solving numerically Eq. (4.33).

## 4.5 Conclusions

In order to assess leading points arguments, this chapter has analyzed exact solutions for flame propagation in periodic shear flows [193]. These results validate some basic ideas from leading points arguments, but also modify them appreciably, at least for this deterministic problem. In particular, these results clearly show that for sufficiently strong (high $A$) and steady (low $V$) flow perturbations, the front displacement speed is controlled by velocity field characteristics at discrete points on the flame. However, these points do not generally lie on the farthest forward point of the front (the "instantaneous leading point"). On the contrary, for sufficiently weak (low $A$) or unsteady (high $V$)

flow perturbations, the front displacement speed is not controlled by discrete points, but rather by the entire spatial distribution of the velocity field. For these conditions, the "instantaneous leading points" do not have any dynamical significance in controlling the front displacement speed. Finally, these results clearly show that the effects of flame curvature sensitivity in modifying the front displacement speed can be successfully interpreted in term of leading point concepts in cases where the set of global minimizers consists of hyperbolic fixed points.

In future it will be of interest to verify if the ideas described in this chapter can be extended to two and three dimensional flows for which the G-equation do not admit global minimizers such as cellular flows consisting of array of vortices [175-177], which may resemble more to the turbulent flow field experienced by a real premixed flame. Also it will be of interest to extend the theory presented in Section 4.4 to thermo-diffusively unstable flames for which $\ell < 0$.

# CHAPTER 5
# CONCLUSIONS AND RECOMMENDATIONS

In this chapter, the overall contributions of the work presented in this thesis are outlined. Additionally, recommendations for further work are put forward for consideration.

## 5.1 Conclusions

The influence of fuel/oxidizer composition on the progration and structure of turbulent premixed flames is a phenomenon of considerable complexity. In order to make progress in understanding this subject it is necessary to identify key governing processes while cutting-off interesting but marginal phenomena. Leading point concepts suggest that the turbulent burning velocity of premixed flames is controlled by the velocity of the points on the flame that propagate farthest out into the reactants. It is also postulated that modifications in the overall turbulent combustion speed depend solely on modifications of the burning rate at the leading points since an increase (decrease) in the average propagation speed of these points causes more (less) flame area to be produced behind them. Several investigators have also assumed that the structure of leading points can be well represented by quasi-steady “critically” stretched laminar flames in canonical configurations. In this framework modeling of turbulent burning rates can be thought as consisting of two sub-problems:

1) modeling of burning rates at the leading points
2) modeling of the dynamics/statistics of the leading points in the turbulent flame.

To address the first sub-problem Chapter 3, has described a comparison between DNS results of lean, $H_2$/air flames and results from several highly-stretched, model geometries. This type of information is useful for modeling purposes in the framework of the leading point concept and may also be compared to similar (but less detailed) attempts to collapse local flame speed data obtained by DNS of turbulent flames using planar laminar flame models [99] (see Section 2.3). For the turbulent flames investigated in this thesis, the influence of curvature on the local structure of the flame front is too large to be neglegted and use only planar laminar flames for comparison.

For the lean hydrogen/air mixture investigated, it has been shown that the overall trend of increasing mean $s_c$, $K_C$ and decreasing $\delta_T$ and $\delta_{H2}$ with increasing turbulence levels follows closely the behavior of model laminar flame computations. In particular at the leading edge, the average flame front structure can be reproduced reasonably well by results obtained from model geometries with the same average mean curvature. This agreement was not necessarily expected, as it is known that unsteady effects decrease the effective stretch sensitivity of the flame. This result might be a manifestation of the weak sensitivity of curvature-induced flame speed modifications to frequency, as opposed to its strong sensitivity to nonsteadiness in hydrodynamic stretch.

For the highest turbulent intensity investigated, case D31, local consumption speed, curvatures and flame thicknesses seems to approach the maximum values obtained by the laminar model geometries, while other cases display substantially lower values. This suggests that at low turbulent intensities “critically” stretched flamelets are not a good model for leading points burning rates, at least for the low Reynolds and low Damköhler number accessible by direct numerical simulations. Such consideration should be taken

into account when developing models for turbulent flame speeds based on leading points concepts, and may explain difficulties of this approaches in modeling turbulent flame speed data at high pressures [9] or for very lean hydrogen/air flames [137].

A major source of difference between model laminar flame computations and highly curved flamelets is the presence of negative (i.e., compressive) strain rates. For the model laminar flames considered in this thesis, strain rates increase monotonically with curvature and are always positive, while for the investigated turbulent flames the correlation between strain rates and curvatures is negative. Because of this effect, the most higly curved flamelets at each turbulent intensity display lower values of consumption speed and are thicker than model laminar flames with equal curvature.

To address the second sub-problem, Chapter 4 covers exact solutions for flame propagation in periodic shear flows. These results validate some basic ideas from leading points arguments, but also modify them appreciably, at least for the deterministic problems considered in this thesis. For the simple case of a front propagating in a one-dimensional shear flow, these results clearly show that the average front displacement speed is controlled by flow field characteristics at discrete points on the flame only when the amplitude of the shear flow is sufficiently large and does not vary too rapidly in time. Furtheremore in these conditions, if the local laminar flame speed at which the flame propagates depends linearly on the flame front local curvature, then overall modifications in the average front displacement speed can be successfully interpreted just studying the curvature of leading points. However, these points do not generally lie on the farthest forward point of the front, differently from the original definition of leading points.

On the contrary, for sufficiently weak or unsteady flow perturbations, the front displacement speed is not controlled by discrete points, but rather by the entire spatial distribution of the velocity field. For these conditions, the leading points do not have any dynamical significance in controlling the front displacement speed. These results seem to indicate that the leading points are able to drive the progation of a flame front only if sufficiently steady and intense flow perturbations exist in the flow field.

## 5.2 Recommendations for future work

To expand and verify results presented in Chapter 3 it would be desirable to investigate turbulent flames at higher Reynolds number and higher Damköhler numbers than those characterizing the DNS database utilized in this thesis. At higher Reynolds number vorticity fluctuations tend to be more concentrated in thin region of space, known as "worms" or "vortex tubes", which are a manifestation of the "internal intermittency" of the turbulent flow [150]. It has been postulated that these flow structures are able to wrinkle and distort the flame much more efficiently than what suggested by low Reynolds number computations and, as such, critically stretched flamelets may be relevant also at low $u'/s_{L0}$ [4]. A relation between "vortex tubes" and regions of high heat release rate was, for example, claimed in the DNS of Tanahashi et al. [121]. However, this proposed mechanism is difficult to verify computationally because of the large computer resources needed to simulate premixed flames at high Reynolds number [133].

Further theoretical/numerical work is also required to better understand unsteady effects on the response of curved premixed laminar flames. As described in Section 2.1.2, most studies on unsteady effects consider flat strained laminar flames in a counterflow configuration. Some insight, may be obtained from flame vortex interactions studies but this configuration is rather complicated. It is envisaged that an improved knowledge of unsteady effects will allow for a more accurate understanding of the local structure of turbulent premixed flames. A possible flame-flow configuration that could be used to study unsteady-curvature effects would be to force harmonically the inlet of a tubular counterflow flame in order to achieve a flame whose curvature varies periodically in a prescribed manner.

Moreover, it will be of interest to verify if the ideas described in Chapter 4 can be extended to two and three dimensional flows for which the G-equation do not admit global minimizers such as cellular flows consisting of array of vortices [175-177] or random flows [174, 194-196], which may resemble more to the turbulent flow field experienced by a real premixed flame. Finally, it will be of interest to extend the theory presented in Section 4.4 to thermo-diffusively unstable flames for which $\ell < 0$.

# APPENDIX A

## A.1. Numerical convergence and validation of the 1D numerical simulations

This section describes numerical convergence studies for the one dimensional numerical models utilized in Chapter 3.

The different versions of the standard OPPDIF code [197] that have been used to simulate the planar counterflow flame and the tubular flame utilize an adaptive placement of mesh points to calculate more accurate solutions on finer meshes starting from solutions calculated on coarser meshes. The adaptive placement of the mesh points is controlled by the first and second derivatives of the solution vector $\varphi$. The code recursively checks that the following inequalities are respected at each grid point $j$:

$$\left|\varphi_j - \varphi_{j-1}\right| < \mathrm{GRAD} \cdot \left|\max\varphi - \min\varphi\right| \tag{A.1}$$

$$\left|\left(\frac{d\varphi}{dx}\right)_j - \left(\frac{d\varphi}{dx}\right)_{j-1}\right| < \mathrm{CURV} \cdot \left|\max\left(\frac{d\varphi}{dx}\right) - \min\left(\frac{d\varphi}{dx}\right)\right| \tag{A.2}$$

where GRAD and CURV are two user-defined parameters which can assume values comprised between 0 and 1. Figure A-1 shows a study on the numerical convergence of three planar counterflow flame calculations characterized by different inlet velocities. These simulations consider a $H_2$/Air flame at an equivalence ratio of $\phi = 0.31$ and reactants at standard temperature and pressure (298K, 1atm). Based on these data, it can be observed that solutions with approximately 2000 mesh points (corresponding to

GRAD = CURV = 0.01) can be considered as numerically converged. For this reason, all the calculations shown in Chapter 3 were performed imposing GRAD = CURV = 0.01.

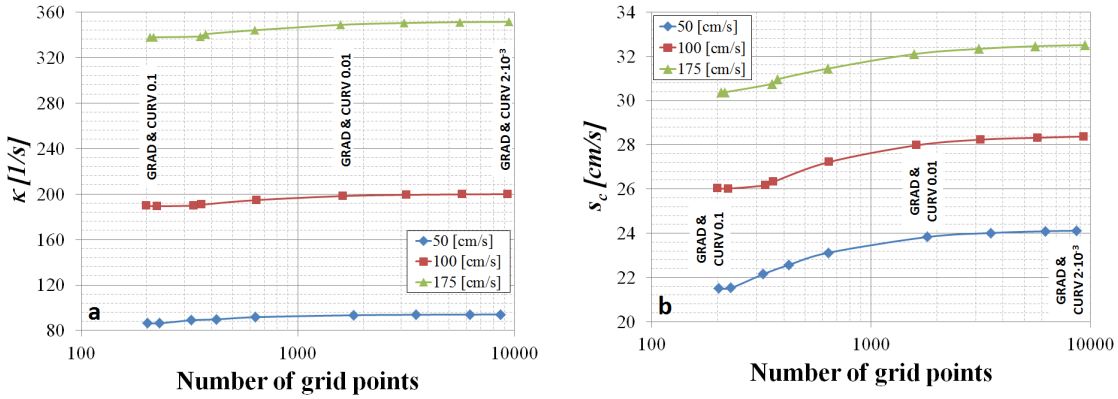


**Figure A-1. Stretch rate $\kappa$ (a) and consumption speed $s_c$ (b) for planar counterflow flame calculations with different number of grid points at three different reactants inlet velocities. For these calculations the distance between jets is equal to 2*cm*.**

As already described in Chapter 3, the expanding cylindrical flame was simulated with an isobaric, one dimensional formulation of the conservation equations in cylindrical coordinates where the continuity, thermal energy and species equations were discretized and solved by means of finite element method as implemented in the commercial software COMSOL© [148]. The $H_2$/Air flames considered in Chapter 3 were resolved with a mesh size $\Delta x = 5 \cdot 10^{-6} m$ corresponding to a ratio $\delta_{T0}/\Delta x = 380$ and advanced in time using the backward differentiation formula implemented in DASPK [198]: relative and absolute tolerances were set equal to $10^{-6}$ and $10^{-9}$, respectively.

To check the accuracy of the time-stepping method, ignition delay times for different mixtures were calculated utilizing the plug-flow reactor code implemented in the "Reaction Engineering Interface" of COMSOL© [148] and compared with those obtained from the standard plug-flow reactor code implemented in CHEMKIN [147]. Figure A-2

shows a comparison between the temperature-time profiles as calculated by the two programs for a $H_2$/CO/Air mixture at different initial temperatures. As it can be observed the calculations agree very well with each other.

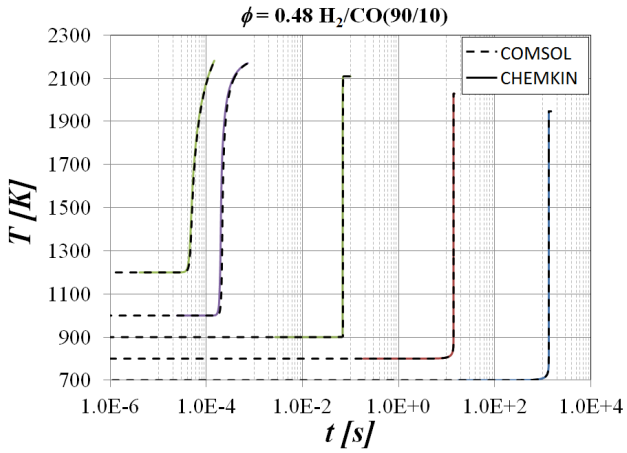


**Figure A-2. Temperature time-history for plug-flow reactors as computed in COMSOL (dashed black lines) and CHEMKIN (solid colored lines). The mixture consider is $H_2$/CO/Air with $\phi$ = 0.48 and $H_2$/CO volumetric ratio equal to 90/10. Initial temperatures range from 700*K* to 1200*K*. The numerical simulations utilize the Davis chemical mechanism [199].**

The ability of the mesh to resolve the flame motion was checked repeating expanding cylindrical flame computations with different mesh sizes. Figure A-3 shows the temperature profiles computed at $t = 1ms$ as obtained by two expanding cylindrical flame calculations characterized by different mesh sizes. The coarse mesh ($\Delta x = 15\mu m$) is already sufficient to accurately compute the flame propagation, but for the calculations in Chapter 3 the finer mesh ($\Delta x = 5\mu m$) was chosen to better resolve spatial and temporal derivatives needed to evaluate the thermal flame thickness $\delta_T$ and the flame displacement speed $dR_{ref}/dt$ (see Section 3.3).

As a final validation of the code developed in COMSOL©, the propagation of a one-dimensional planar flame was computed modifying the code utilized for the expanding cylindrical flame. Figure A-4 illustrates the result of a calculations in which a planar $H_2$/air ($\phi = 0.31$) flame propagated until reaching steady state and shows that the solution computed agrees with profiles computed from the standard PREMIX code [200].

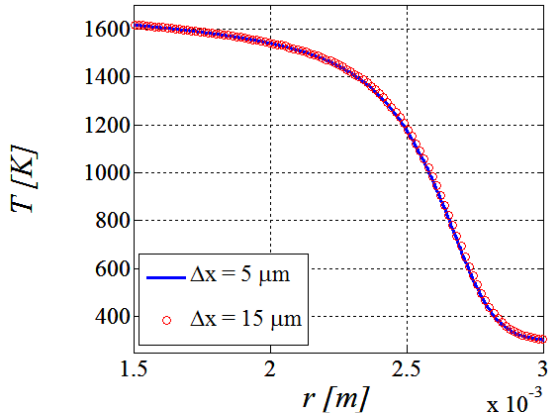


**Figure A-3. Temperature profiles at t = 1*ms* for two expanding cylindrical flame calculations computed with different mesh sizes Δ*x* ($H_2$/Air, $\phi = 0.37$, $T^u = 298K$, $p = 1atm$, $R_i/\delta_{T0} = 1$ [201]).**

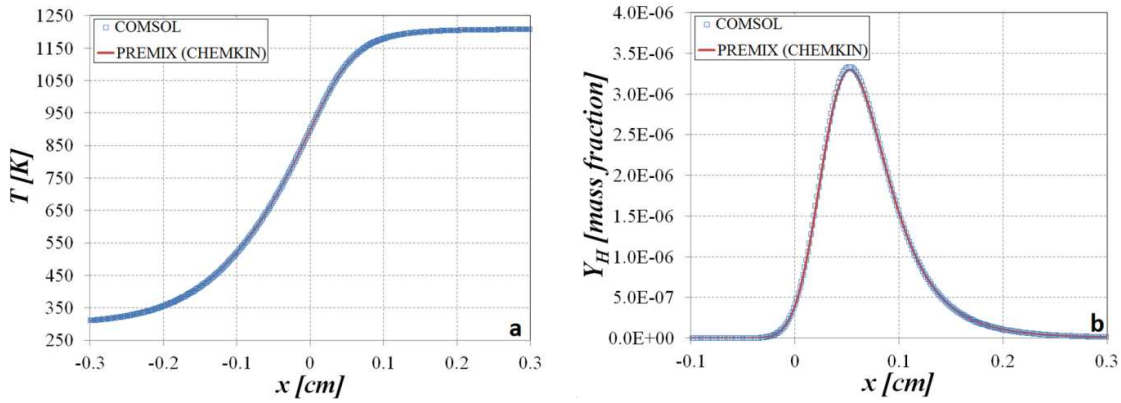


**Figure A-4. Comparison between solutions obtained from PREMIX [200] and from one-dimensional planar computations in COMSOL at steady state. Figure (a) and (b) show temperature and H atom mass fraction profiles, respectively. The two numerical simulations utilize the same transport coefficients, thermodynamics properties and chemical kinetics of the $H_2/O_2$ system of GRI 2.11 mechanism [146] and a mixture averaged formulation [113] to model molecular diffusion.**

## A.2. Quasi-steady response and ignition transients of expanding cylindrical flames

This section discusses the quasi-steady response and the ignition transients associated with the cylindrical flames numerical simulations presented in Section 3.3. We follow a procedure similar to that described in Ref. [48] to identify unsteady effects in the response of propagating flames. The starting point of this analysis is the energy balance equation written in cylindrical coordinates [202]:

$$\rho c_p \left( \frac{\partial T}{\partial t} + u_r \frac{\partial T}{\partial r} \right) = \frac{1}{r} \frac{\partial}{\partial r} \left( r \lambda \frac{\partial T}{\partial r} \right) - \sum_{k=1}^{K} c_{pk} j_{kr} \frac{\partial T}{\partial r} + \dot{q}''' \qquad \text{(A.3)}$$

where $\rho$ represents the density of the gas mixture, $c_p$ is the specific heat at constant pressure of the gas mixture, $u_r$ is the gas flow velocity in the radial direction, $\lambda$ is the thermal conductivity of the gas mixture, $c_{pk}$ is the specific heat at constant pressure of the $k$-th species, $j_{kr}$ is the diffusion flux of the $k$-th species and $\dot{q}'''$ is the heat release per unit volume due to chemical reactions. Rewrinting equation (A.3) in a reference frame moving with the flame at a speed $s_d = dR_{ref} / dt$ we obtain

$$\underbrace{-\rho c_p \left( \frac{\partial T}{\partial t} + s_d \frac{\partial T}{\partial r} \right)}_{\substack{\textit{Unsteady} \\ \textit{Term}}} \underbrace{-\left( u_r - s_d \right) \frac{\partial T}{\partial r}}_{\substack{\textit{Convection} \\ \textit{Term}}} + \underbrace{\frac{1}{r} \frac{\partial}{\partial r} \left( r \lambda \frac{\partial T}{\partial r} \right)}_{\substack{\textit{Diffusion} \\ \textit{Term}}} \underbrace{- \sum_{k=1}^{K} c_{p,k} j_{r,k} \frac{\partial T}{\partial r} + \dot{q}'''}_{\substack{\textit{Chemical} \\ \textit{heat source}}} = 0 \qquad \text{(A.4)}$$

Unsteady effects are associated with the first term in equation (A.4): in the quasi-steady limit, this term is small compared to the others.

Figure A-5 shows the magnitude of the various terms of equation (A.4) plotted against radial position $r$ at different time instants ($t$ = 0.1, 0.2, 0.5 and 1ms) after ignition ($t$ = 0ms) for ECF with $R_i/\delta_{T0} = 0.25$. For convenience, Figure A-6 shows these time instants plotted as dots on the graphs of consumption rate $s_c$ versus time $t$ or curvature $K_C$ to have a direct comparison with the data presented in Section 3.3. Figure A-7 and Figure A-8 show the same analyses as Figure A-5 and Figure A-6 but for the ECF with $R_i/\delta_{T0} = 0.75$. As it can be observed from these figures, the magnitude of the unsteady term (solid line) is small at $t$ = 0.5 and 1ms for both intial radii $R_i$ of the ignition pocket. These data indicate that after reaching a peak consumption speed, the response of these cylindrical flames quickly becomes quasi-steady. The difference between quasi-steady responses of ECF with different $R_i$ are entirely due to the different energy contained in the ingntion pocket [48]. Finally, it should be noted that the unsteady term does not become exactly equal to zero because the flame thickness is increasing and the products at the center of the pocket are cooling as the flame expands because of non-unity Lewis number effects and differential diffusion of species.

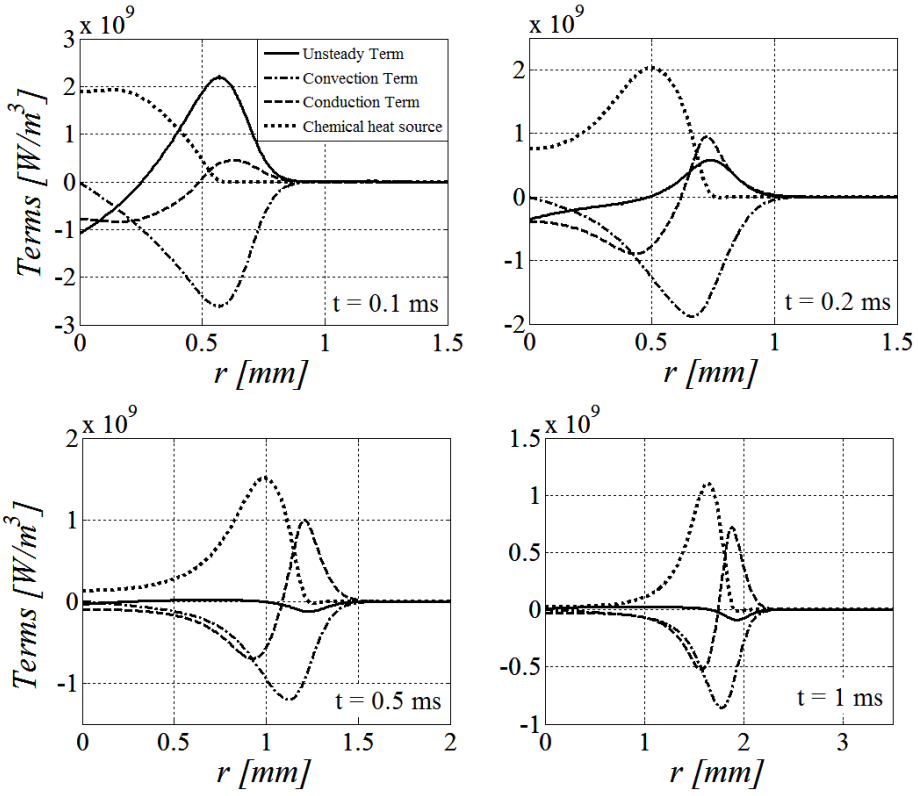


**Figure A-5. Magnitude of the terms in equation (A.4) plotted against radial position *r* at different time instants (*t* = 0.1, 0.2, 0.5 and 1ms shown in Figure A-6) after ignition (*t* = 0ms) for ECF with $R_i/\delta_{T0} = 0.25$.**

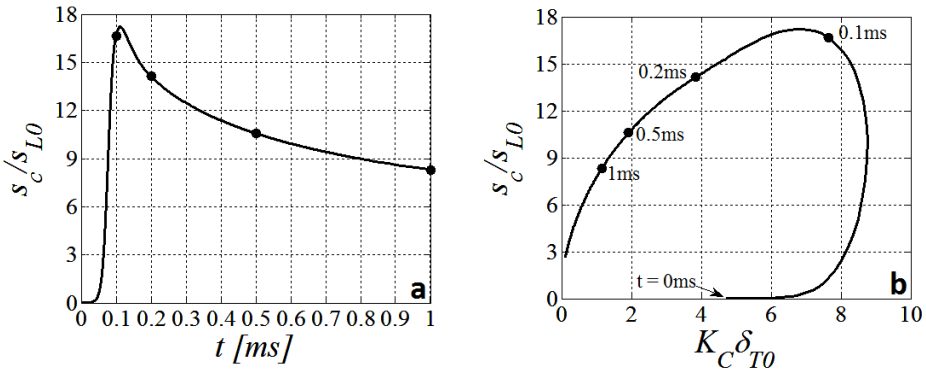


**Figure A-6. Consumption rate $s_c$ plotted against time $t$ (a) and curvature $K_C = 1/R_{ref}$ (b) for ECF with $R_i/\delta_{T0} = 0.25$. The dots represent the time instants at which the data in Figure A-5 are obtained.**

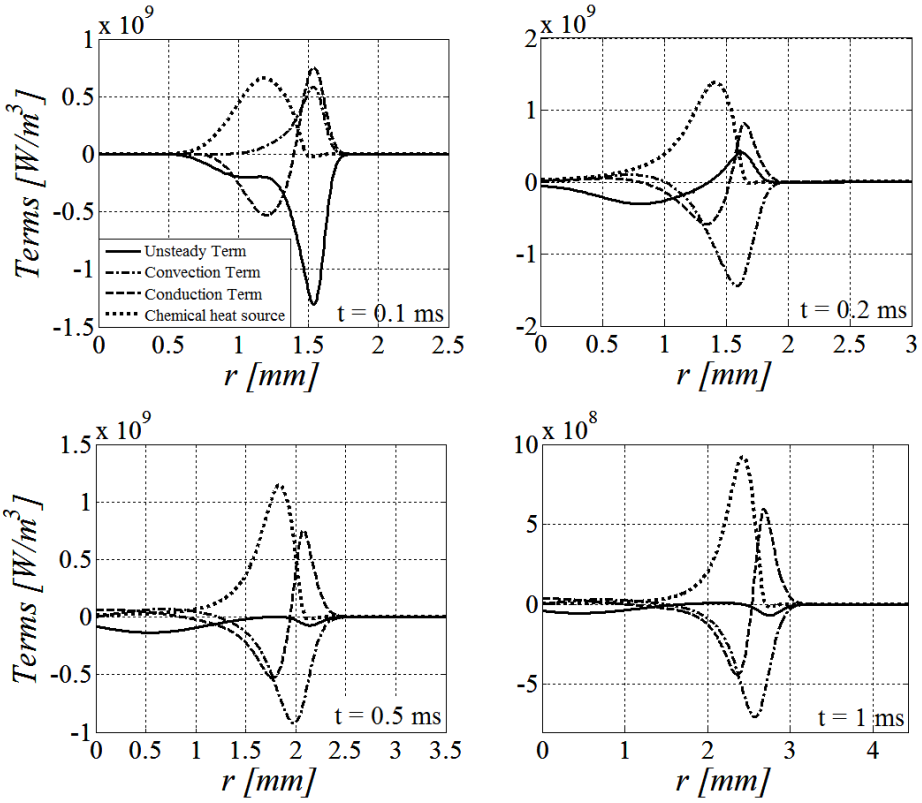


**Figure A-7. Magnitude of the terms in equation (A.4) plotted against radial position *r* at different time instants (*t* = 0.1, 0.2, 0.5 and 1ms shown in Figure A-8) after ignition (*t* = 0ms) for ECF with $R_i/\delta_{T0} = 0.75$**

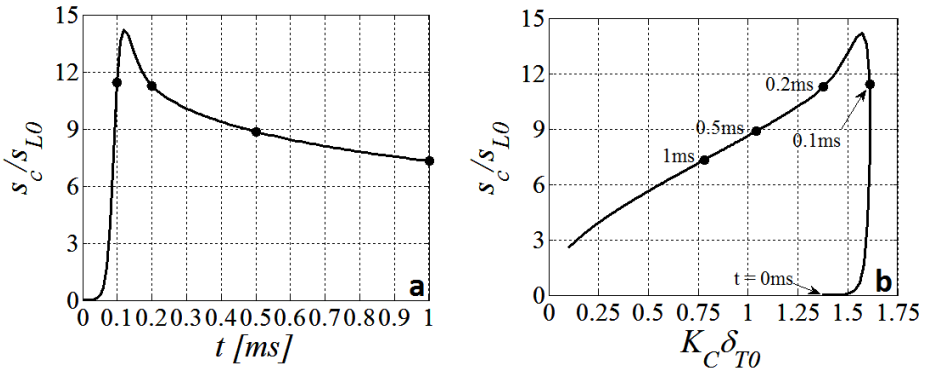


**Figure A-8. Consumption rate $s_c$ plotted against time $t$ (a) and curvature $K_C = 1/R_{ref}$ (b) for ECF with $R_i/\delta_{T0} = 0.75$. The dots represent the time instants at which the data in Figure A-7 are obtained.**

## A.3. Tubular flames with an inner wall and spherical flames

This section presents results for two other one-dimensional flame geometries related to those presented in Chapter 3 and shown in Figure A-9: tubular flames with an inner wall of radius $R_I$ and expanding spherical flames (ESF) ignited from a pocket of burnt gases. These geometries were not included in Chapter 3 because they do not add much information to the results already presented in Section 3.3: the separate effects of curvature, strain and ignition transients can be discussed satisfactorily just utilizing planar counterflow flames (PCF), tubular flames with no inner wall (TCF) and expanding cylindrical flames (ECF). Nonetheless, these results are reported in this Section for completeness. As in Chapter 3, all the numerical simulations considered in this Appendix utilize the transport coefficients, thermodynamics properties and chemical kinetics of the $H_2/O_2$ system of GRI 2.11 mechanism [146] and a mixture averaged formulation [113] to model molecular diffusion. Furthermore, we consider only an $H_2$/Air flame at an equivalence ratio of $\phi = 0.31$ and with initial reactants temperature $T^u = 298K$ and at pressure $p = 1atm$.

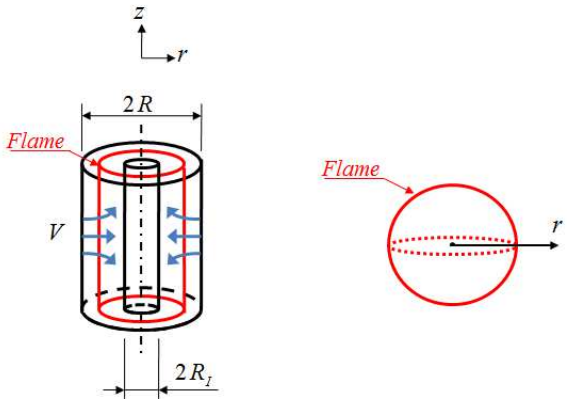


**Figure A-9. Premixed flame geometrical configurations described in this Appendix: tubular counterflow flame with an inner wall of radius $R_I$ (left), expanding spherical flame (right).**

The tubular flame with an inner wall represents an intermediate situation between a PCF ( $R > R_I \to \infty$ ) and a TCF ( $R > R_I = 0$ ). The size of the internal radius $R_I$ adds a degree of freedom to the flame response since different flames subjected to equal stretch rates $\kappa = du_z/dz$ can have different radius of curvature depending on the size of $R_I$. In fact, this geometrical configuration is useful to study the different effects of strain and curvature on the flame response, as pointed out for example in Ref. [203]. To illustrate, Figure A-10 shows the consumption speed $s_c$ (as defined in Chapter 3) dependence on stretch rate $\kappa$ for flames with different $R_I$: for all the simulations the external radius was maintained at the same distance from the internal radius, $R = R_I + 1cm$. As it can be observed, at smaller $R_I$ consumption speed are larger for the same value of stretch rate, with the differences increasing as the stretch rate increases.

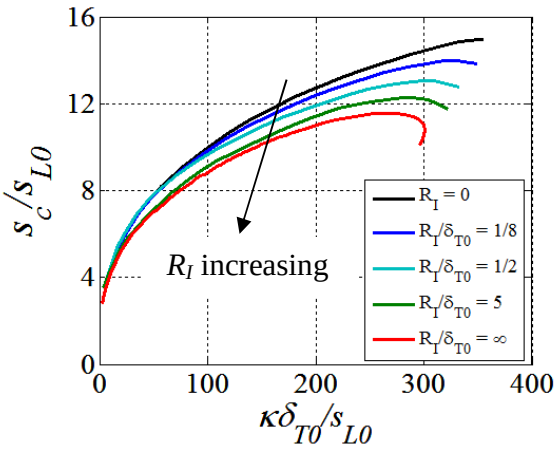


**Figure A-10. Consumption rate $s_c$ dependence on stretch rate $\kappa$ for tubular counterflow flame computations with inner walls of different radii $R_I$ and $R = R_I + 1cm$. The $R_I/\delta_{T0} = \infty$ curve refers to solutions obtained from a PCF computation.**

The characteristics of expanding spherical flames are similar to those of expanding cylindrical flames. However, for the same flame radius $R_{ref}$ the mean curvature of spherical flames ($K_C = 2/R_{ref}$) is two times larger than that of cylindrical flames ($K_C = 1/R_{ref}$): this causes ignition transients and nonlinear effects to differ between the two configurations. Figure A-11 shows the consumption rate $s_c$ and flame thicknesses $\delta_T$ and $\delta_{H2}$ for TCF ($R_I = 0$), ECF and ESF both ignited by a pocket of burnt gases with initial radius $R_i/\delta_{T0} = 0.25$. As it can be observed from Figure A-11a, the consumption speed $s_c$ of the spherical flame is bounded between the ECF and TCF solutions except at high $K_C$, which are inaccessible to ECF and TCF. Figure A-11b and c, instead, shows that for low $K_C$ spherical flames tend to be thicker than cylindrical flames.

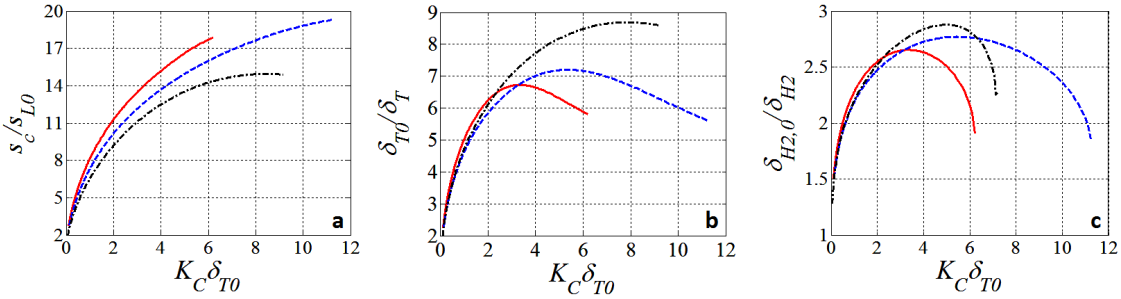


**Figure A-11. Consumption rate $s_c$ (a), inverse of flame thickness $\delta_T$ (b) and $\delta_{H2}$ (c) plotted against mean curvature $K_C$ for an expanding cylindrical flame with $R_i/\delta_{T0}=0.25$ (solid red line), an expanding spherical flame with $R_i/\delta_{T0}=0.25$ (dashed blue line) and a tubular flame with no inner wall (dashed-dotted black line).**

# APPENDIX B

## B.1. Sensitivity to the choice of $T_{ref}$

In this Section we investigate the sensitivity of the results presented in Chapter 3 to the particular choice of temperature isosurface $T_{ref}$ used to represent the flame surface position.

Figure B-1 shows the fuel consumption weighted joint PDFs of local mean curvature $K_C$ with consumption speed $s_c$ (1st row), inverse of flame thickness $\delta_T$ (2nd row), $\delta_{H2}$ (3rd row) and strain rate $K_S$ (4th row) for the cylindrical and spherical flamelets of case C31; different isothermal surfaces $T_{ref}$ are used to define the flame surface: $T_{ref} = 990K$ (left column), $T_{ref} = 1088K$ (central column) and $T_{ref} = 1190K$ (right column). From these figures it is clear that the peak probability of the joint PDFs falls on top of the model laminar flame computations regardless of the particular $T_{ref}$ choice: with increasing $T_{ref}$ curvatures values $K_C$ tend to be higher while strain rate $K_S$ values tend to be lower, in agreement with the model laminar flame computations. Besides, the overall shape of the joint PDFs does not appear to be affected by the particular choice of $T_{ref}$, except for the $s_c - K_C$ joint PDF. The definition of $s_c$ implicitly depends on $K_C$ through the term $A_{ref}$ (see Section 3.2) and the decrease in $H_2$ consumption at higher curvatures due to flame thickening is counteracted by the decrease in $A_{ref}$. For this reason the consumption speed of the most highly curved flamelets agrees better with the model laminar flame

calculations for $T_{ref} = 1190K$. Similar considerations are valid for the other cases (A31, B31 and D31), which are not shown here.

Figure B-2 shows the fuel consumption weighted join PDFs of strain rate $K_S$ with consumption speed $s_c$ (1st row) and flame thickness $\delta_T$ (2nd row), $\delta_{H2}$ (3rd row) for flame elements characterized by $\left|K_C \delta_{T0}\right| < 0.1$ for case C31; different isothermal surfaces $T_{ref}$ are used to define the flame surface: $T_{ref} = 990K$ (left column), $T_{ref} = 1088K$ (central column) and $T_{ref} = 1190K$ (right column). As it can be observed, the overall shape of the joint PDFs is not substantially modified by the particular $T_{ref}$ choice. However, the scatter in the joint PDFs decreases with decreasing $T_{ref}$. This is presumably due to the fact that $s_c$, $\delta_T$, $\delta_{H2}$ and $K_S$ are less sensitive to curvature effects for $T_{ref} = 990K$, as shown in Figure B-1.

Finally, Figure B-3 and Figure B-4 show mean and standard deviations of data collected at leading edge of the turbulent flame brush (see Section 3.5) for $s_c$ (1st row), $\delta_T$ (2nd row), $\delta_{H2}$ (3rd row) and $K_S$ (4th row) plotted against leading edge mean $K_C$; different isothermal surfaces $T_{ref}$ are used to define the flame surface: $T_{ref} = 990K$ (left column), $T_{ref} = 1088K$ (central column) and $T_{ref} = 1190K$ (right column). These figures show that the 1D laminar simulations computed at the average value of mean curvature reasonably follow the enhancement in consumption speed with increasing turbulent intensity regardless of the $T_{ref}$ chosen.

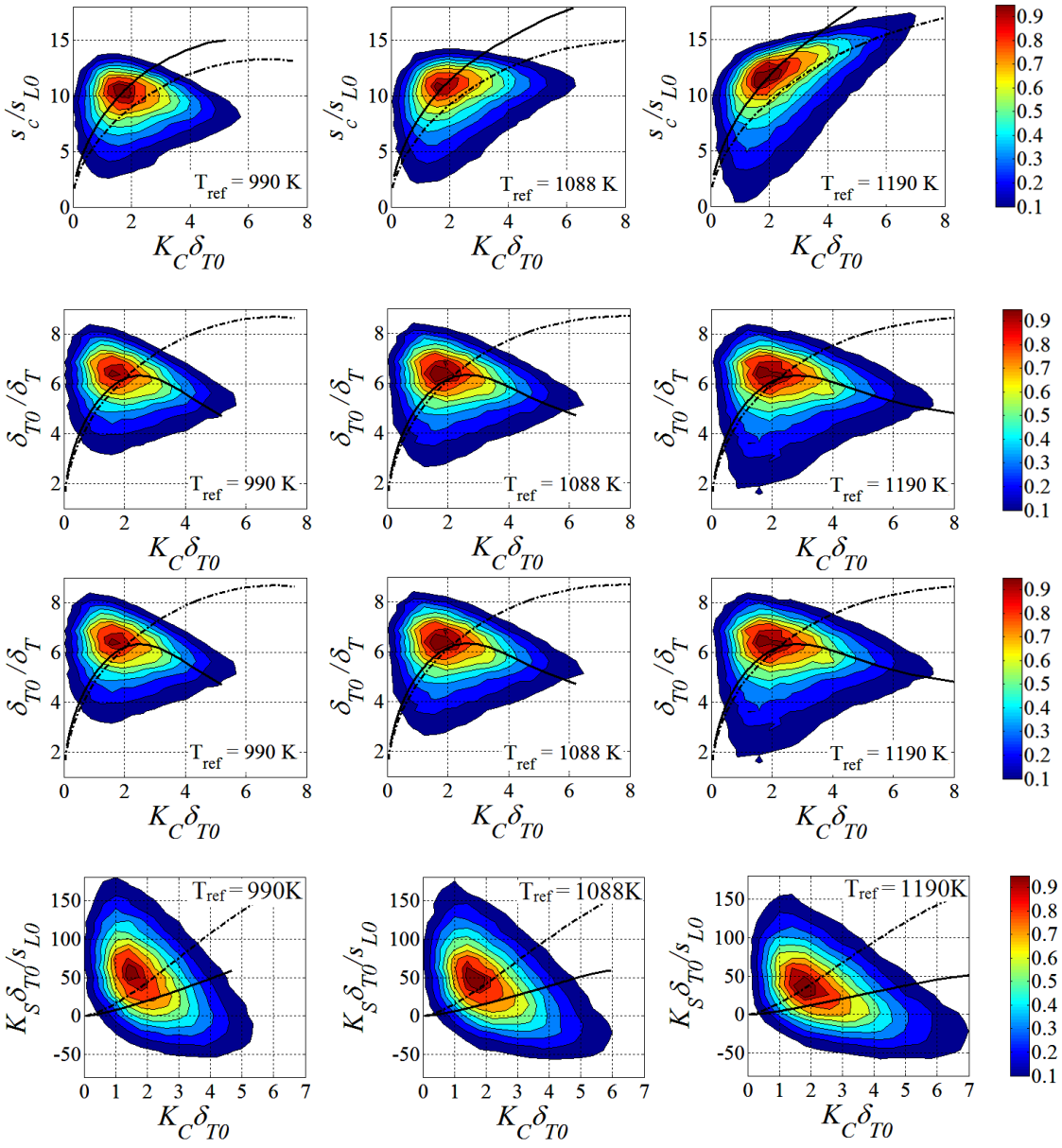


**Figure B-1. Case C31: fuel consumption-weighted joint PDFs of mean curvature $K_C$ and burning speed $s_c$ (1st row), flame thickness $\delta_T$ (2nd row), $\delta_{H2}$ (3rd row) and strain rate $K_S$ (4th row) for cylindrical and spherical flame elements ($k_1 > k_2 > 0$). The PDFs are normalized to the peak values. Lines superimposed to the contours refer to results obtained from one-dimensional laminar flame computations: dot-dashed lines refer to TCF computations while solid lines refer to ECF computations with $R_i/\delta_{T0} = 0.25$. Different isothermal surfaces $T_{ref}$ are used to define the flame surface: $T_{ref} = 990K$ (left column), $T_{ref} = 1088K$ (central column) and $T_{ref} = 1190K$ (right column).**

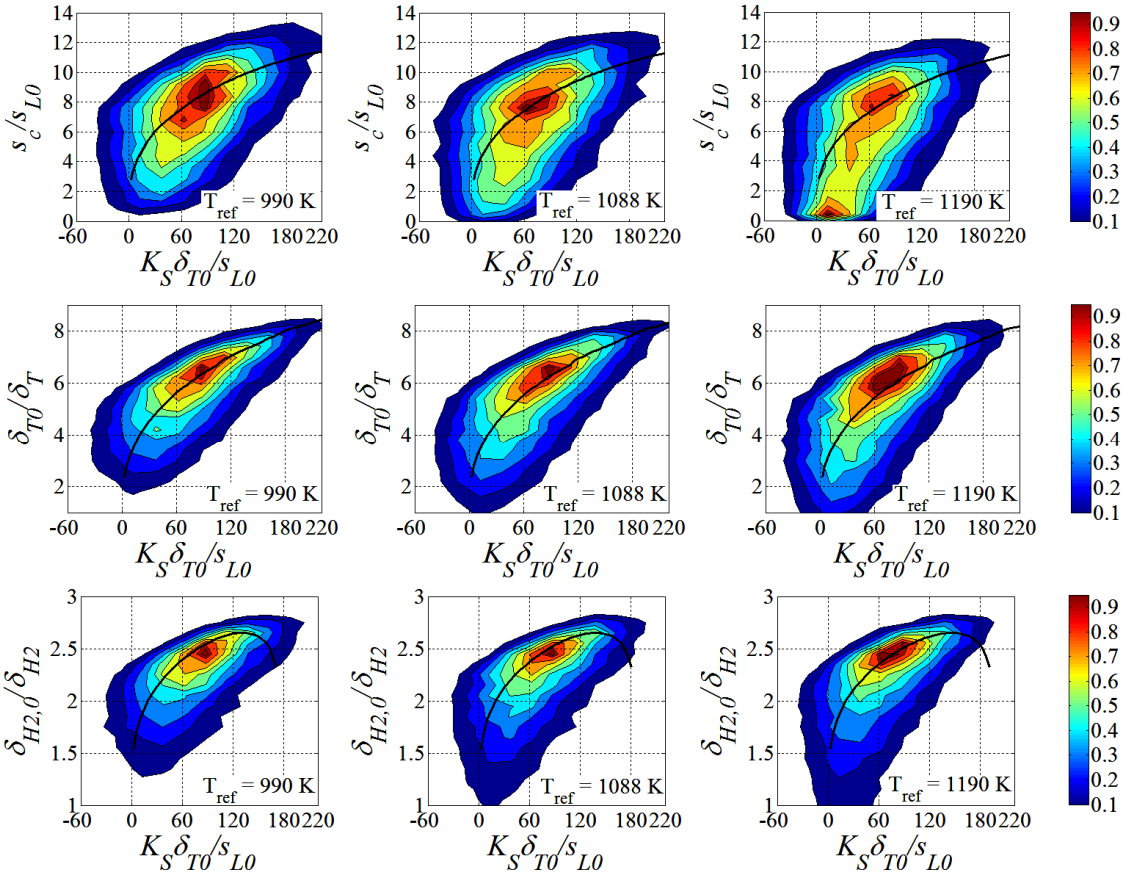


**Figure B-2. Case C31: fuel consumption-weighted joint PDFs of strain rate $K_S$ and burning speed $s_c$ (1st row), flame thickness $\delta_T$ (2nd row) and $\delta_{H2}$ (3rd row) for flame elements whose mean curvature is less than one tenth of the unstretched thermal flame thickness (i.e. $|K_C\delta_{T0}| < 0.1$). The PDFs are normalized to the peak values. Solid lines refer to PCF computations. Different isothermal surfaces $T_{ref}$ are used to define the flame surface: $T_{ref} = 990K$ (left column), $T_{ref} = 1088K$ (central column) and $T_{ref} = 1190K$ (right column).**

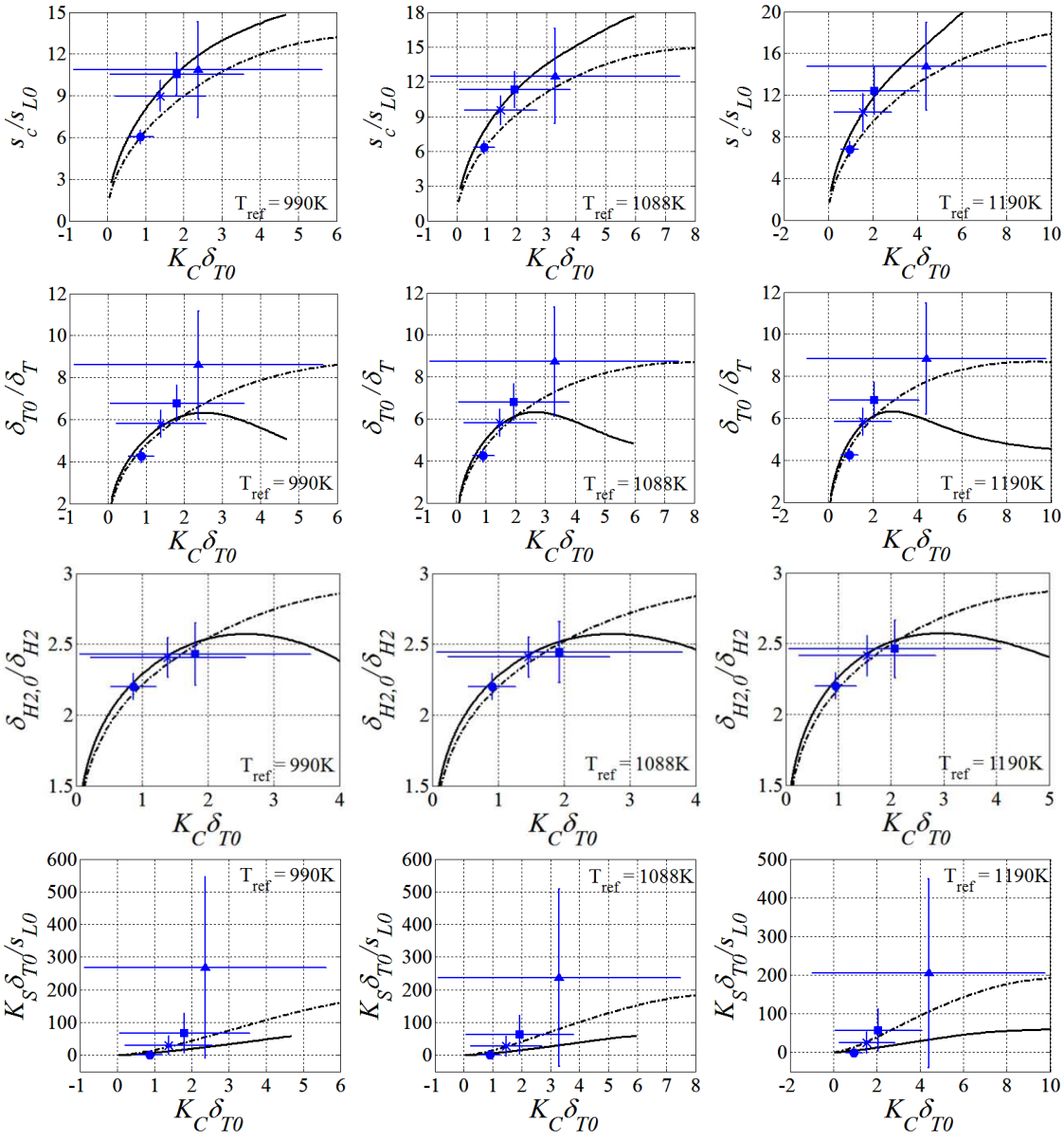


**Figure B-3. Leading edge mean consumption rate $s_c$ (1st row), mean flame thickness $\delta_T$ (2nd row), $\delta_{H2}$ (3rd row) and mean strain rate $K_S$ (4th row) plotted against leading edge average mean curvature $K_C$. Symbols refers to different DNS cases (A31 "●", B31 "x", C31 "■" and D31 "▲"). The total length of the error bars is equal to $\sigma$ on each side. Thicker solid lines refer to ECF computations with $R_i = \delta_{T0}/4$ while thicker dot-dashed lines refer to TCF computations. Different isothermal surfaces $T_{ref}$ are used to define the flame surface: $T_{ref} = 990K$ (left column), $T_{ref} = 1088K$ (central column) and $T_{ref} = 1190K$ (right column).**

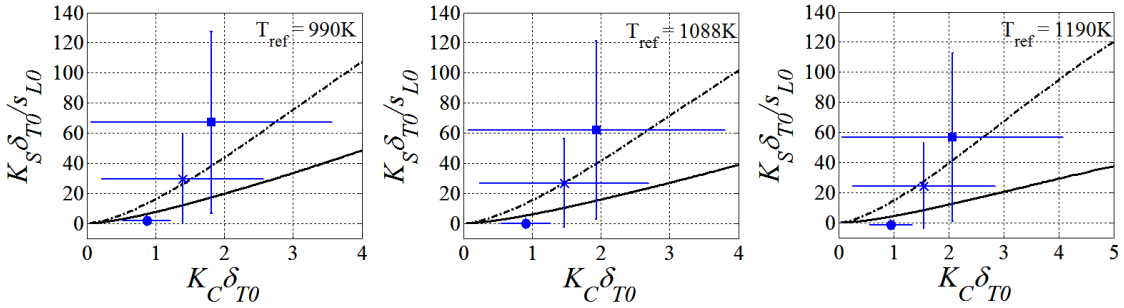


**Figure B-4. Magnified view of Figure B-3 (4th row) centered on case A31, B31 and C31.**

## B.2. Sensitivity to the definition of leading edge

In this Section we investigate the sensitivity of the results presented in Section 3.5 to the definition used to identify the leading edge of the turbulent flame brush. In Section 3.2 a progress variable $\overline{c}$ at each time instant was defined based on the instantaneous consumption rate of $H_2$ and then the leading edge was defined as the region $0 \le \overline{c} \le 0.05$. Figure B-5 and Figure B-7 display mean and standard deviations of data collected at leading edge of the turbulent flame brush (see Section 3.5) for $s_c$ (1st row), $\delta_T$ (2nd row), $\delta_{H2}$ (3rd row) and $K_S$ (4th row) plotted against leading edge mean $K_C$; different progress variable $\overline{c}$ intervals are used to identify the leading edge : $0 \le \overline{c} \le 0.025$ (left column), $0 \le \overline{c} \le 0.05$ (central column) and $0 \le \overline{c} \le 0.1$ (right column). Clearly, there is little difference between the three sets of samples, indicating a satisfactory level of statistical-convergence. As expected, average values of $s_c$, $K_C$, $K_S$, $1/\delta_T$ and $1/\delta_{H2}$ tend to increase slightly and standard devaitions tend to decrease slightly as the sample size is reduced and moved closer to the leading edge (i.e. for $0 \le \overline{c} \le 0.025$).

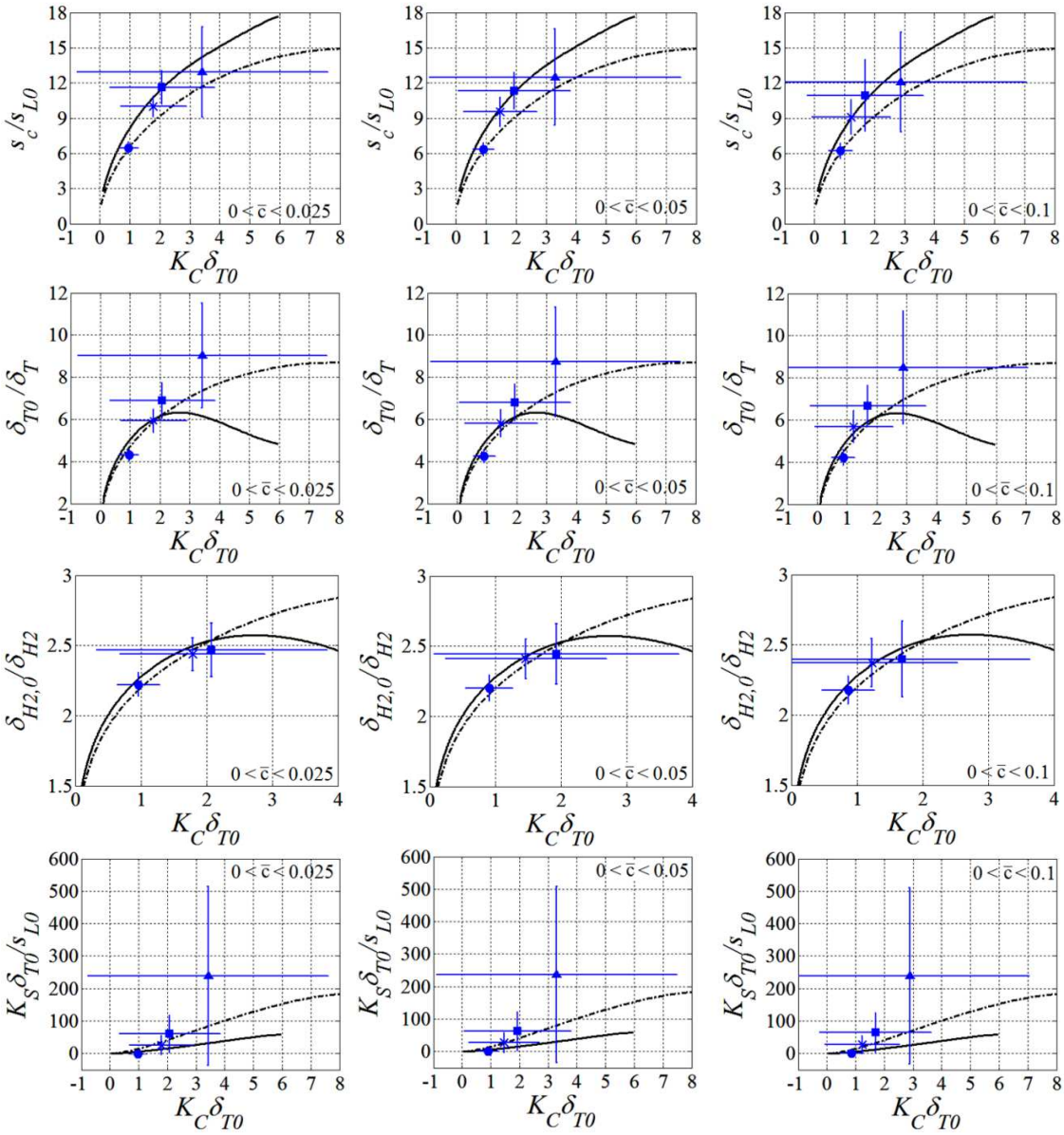


**Figure B-5. Leading edge mean consumption rate $s_c$ (1st row), mean flame thickness $\delta_T$ (2nd row), $\delta_{H2}$ (3rd row) and mean strain rate $K_S$ (4th row) plotted against leading edge average mean curvature $K_C$. Symbols refers to different DNS cases (A31 "●", B31 "x", C31 "■" and D31 "▲"). The total length of the error bars is equal to $\sigma$ on each side. Thicker solid lines refer to ECF computations with $R_i = \delta_{T0}/4$ while thicker dot-dashed lines refer to TCF computations. Different averaged progress variable intervals are used to define the leading edge of the turbulent flame brush: $0 \le \overline{c} \le 0.025$ (left column), $0 \le \overline{c} \le 0.05$ (central column) and $0 \le \overline{c} \le 0.1$ (right column).**

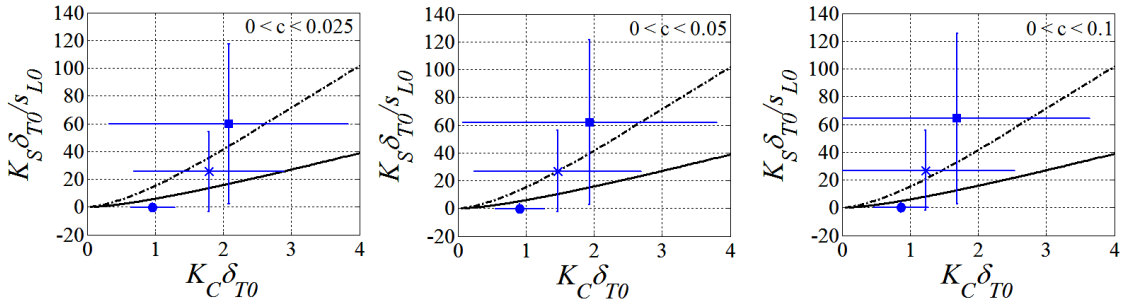


**Figure B-6. Magnified view of Figure B-5 (4th row) centered on case A31, B31 and C31.**

## B.3. Joint PDFs at the leading edge

To extend the investigation of statistics collected at the leading edge of the flame brush presented in Section 3.5, Figure B-7 shows area weighted joint PDFs of local mean curvature $K_C$ with consumption speed $s_c$ (1st row), inverse of flame thickness $\delta_T$ (2nd row), $\delta_{H2}$ (3rd row) and strain rate $K_S$ (4th row) for case A31 (1st column), B31 (2nd column), C31 (3rd column) and D31 (4th column). The symbols superimposed to the contours of these joint PDFs refer to leading edge area-weighted means of $s_c$, $\delta_T$ , $\delta_{H2}$ and $K_S$ plotted against leading edge area-weighted mean $K_C$ while the total length of the error bars is equal to $\sigma$ on each side. These figures show that mean and standard deviations are sufficient to capture the increasing trend of $s_c$, $K_C$ and $K_S$ and decrease of $\delta_T$ and $\delta_{H2}$ with increasing turbulence. The peak of these joint PDFs are close to the mean values, indicating that the joint PDFs are not too asymmetric, except for the $K_C - K_S$ joint PDF of case D31 for which the joint pdf is highly asymmetric. Sign and strength of the correlations between $K_C$ and $s_c$, $\delta_T$ , $\delta_{H2}$ and $K_S$ is consistent with the discussions presented in Chapter 3 for fuel consumption weighted joint PDFs. Similar

considerations are applicable when only cylindrical and spherical elements are considered, as shown in Figure B-8.

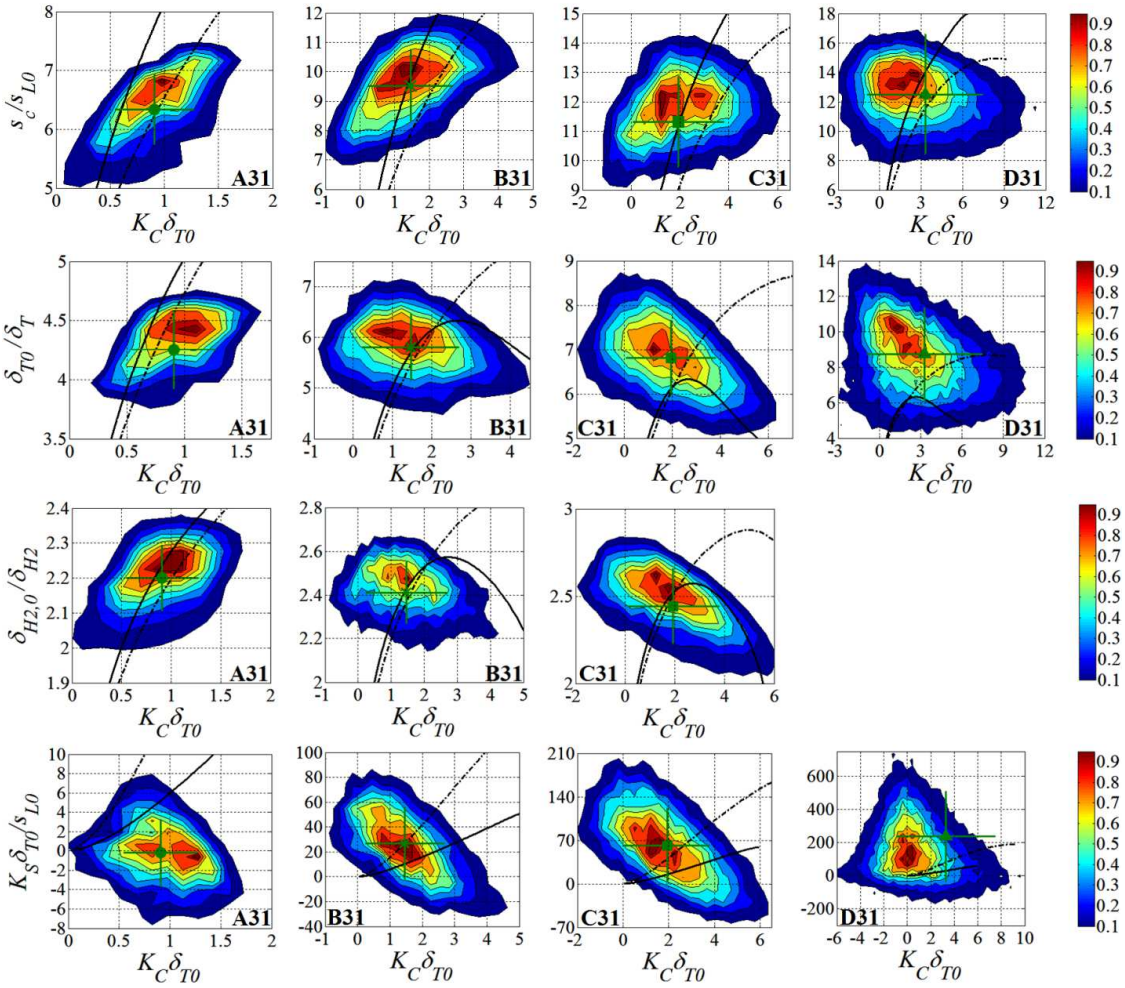


**Figure B-7. Area weighted joint PDFs of mean curvature $K_C$ and burning speed $s_c$ (1st row), flame thickness $\delta_T$ (2nd row), $\delta_{H2}$ (3rd row) and strain rate $K_S$ (4th row) at the leading edge for case A31 (1st column), B31 (2nd column), C31 (3rd column) and D31 (4th column). Symbols refer to leading edge area-weighted means of $s_c$, $\delta_T$ , $\delta_{H2}$ and $K_S$ plotted against leading edge area-weighted mean $K_C$. The total length of the error bars is equal to $\sigma$ on each side. Thicker black solid lines refer to ECF computations with $R_i = \delta_{T0}/4$ while thicker black dot-dashed lines refer to TCF computations.**

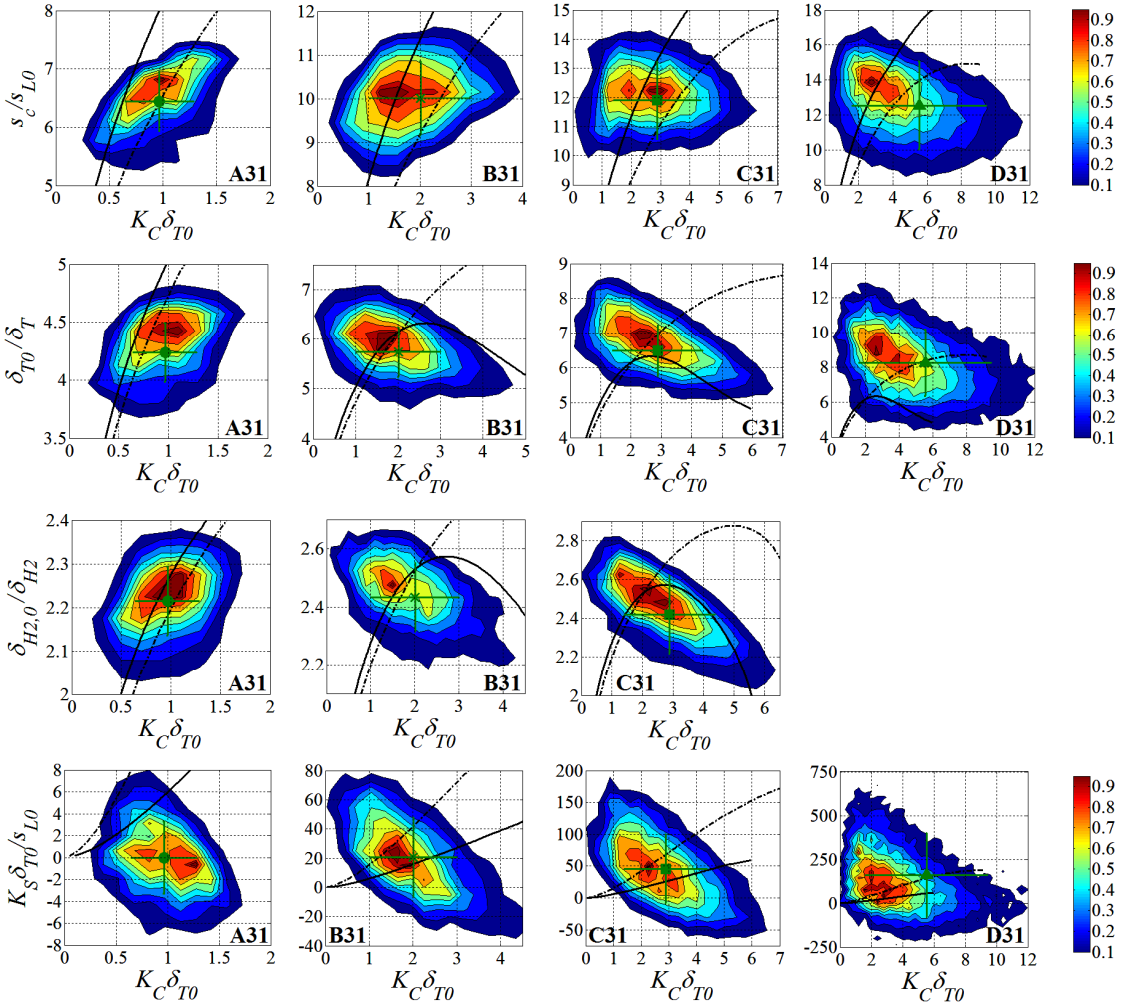


**Figure B-8. Same as in Figure B-7, but only considering cylindrical and spherical flame elements ($k_1 > k_2 > 0$) at the leading edge.**

# APPENDIX C

This Appendix describes the analytical solution of the model problem of Section 4.3 [160]. This solution is obtained through an averaging procedure (homogenization) for the G-equation applicable when the velocity flow field in which the flame is moving is composed by spatially and temporally separated scales. Let us assume that $\vec{u}$ in Eq. (4.3) is an incompressible velocity field with two separated spatial scales $\vec{u} = \vec{\vec{v}}(\vec{x}) + \vec{v}(\vec{x}/\varepsilon)$, where $\varepsilon$ is a small parameter representing the ratio of the two length scales of the velocity field: in this context it is natural to seek a solution $G$ in the form of an asymptotic multiscale expansion

$$G = G^0(\vec{x}, t) + \varepsilon G^1(\vec{x}, \vec{x}/\varepsilon, t) + \ldots \tag{C.1}$$

Substituting Eq. (C.1) into Eq. (4.3) at the leading order we obtain

$$\frac{\partial G^0}{\partial t} + \left(\vec{\vec{v}}(\vec{x}) + \vec{v}(\vec{y})\right) \cdot \left(\nabla_{\vec{x}} G^0 + \nabla_{\vec{y}} G^1\right) - s_L \left\| \nabla_{\vec{x}} G^0 + \nabla_{\vec{y}} G^1 \right\| = 0 \tag{C.2}$$

where $\vec{y} = \vec{x}/\varepsilon$. The objective of the homogenization procedure is to describe the motion of the larger scale $G^0$ in terms of the smaller scale $G^1$, namely, to obtain the effective propagation speed $s_T(\vec{P}, \vec{x})$ of the large scale for a given position $\vec{x}$ and direction of propagation $\vec{P} = -\nabla_{\vec{x}} G^0$

$$\frac{\partial G^0}{\partial t} = s_T\left(\vec{P},\vec{x}\right) \tag{C.3}$$

where

$$s_T\left(\vec{P},\vec{x}\right) = -\left(\vec{\bar{v}}\left(\vec{x}\right)+\vec{v}\left(\vec{y}\right)\right)\cdot\left(-\vec{P}+\nabla_{\vec{y}}G^1\right)+s_L\left\|-\vec{P}+\nabla_{\vec{y}}G^1\right\| \tag{C.4}$$

Eq. (C.4) is a nonlinear eigenvalue problem, referred to as the flame "cell problem" [204]. If the larger scale is a constant $\vec{\bar{v}}\left(\vec{x}\right)=const$ (i.e., its period is infinite) the ansatz (C.1) is an exact solution and $s_T$ obtained by homogenization procedure is the same as that obtained by simply averaging the Hamiltonian as in equation (4.6). In this case the discussion on the multiscale expansion has only a motivational purpose.

In our model problem, we considered a two scale flow with $\vec{\bar{v}}\left(\vec{x}\right)=\left(V,0\right)=const$ and $\vec{v}\left(\vec{x}/\varepsilon\right)=\left(0,f(x)\right)$, where $f(x)$ is periodic of period $L$ and zero mean; our choice of $G=y-\xi\left(x,t\right)$ in Eq. (4.4) is equivalent to imposing $G^0=y$ and $G^1=-\xi\left(x,t\right)$ with the mean direction of propagation now being $\vec{P}=(0,-1)$. With these choices Eq. (C.4) reduces to:

$$s_T = s_L\sqrt{1+g^2}+Vg-f\left(x\right) \tag{C.5}$$

The eigenfunction $g$ of this nonlinear eigenvalue problem has to satisfy a periodicity condition

$$\frac{1}{L}\int_0^L g\,dx = \bar{g} = 0 \tag{C.6}$$

This average slope $\bar{g}$ can also be interpreted as a conserved quantity for the conservation equation (4.5), since its dynamics does not modify $\bar{g}$. For Hamiltonians of the mechanical type, $H(x,t,g) = g^2/2 + f(x,t)$, this quantity represents an average momentum of the system [169]. Equations (C.5)-(C.6) can be solved using the procedure presented in Table 3. This is a simplified version of the procedure in Ref. [160] which includes a general dependence on mean direction of propagation $\vec{P} = (\sin\theta, \cos\theta)$ and the constant large scale velocity $\vec{\bar{v}}(\vec{x}) = V(\cos\bar{\theta}, \sin\bar{\theta}) = const$. This simplified problem was also originally solved by Phillips [205] who utilizes the term "leading points", which correspond to our "Aubry-Mather leading points" in Chapter 4.

Once $s_T$ has been calculated, the flame shape can be calculated solving Eq.(C.5) for $g$:

$$g_{\pm} = \frac{V\left(s_T + f(x)\right) \pm s_L\sqrt{V^2 - s_L^2 + \left(s_T + f(x)\right)^2}}{V^2 - s_L^2} \tag{C.7}$$

Eq. (C.7) has two branches. For case 1 and case 2b in Table 3 the only physical solution is $g_-$, since it is the only one that satisfies the periodicity condition (C.6). For case 2a in Table 3, the physical solution $g$ jumps between the two branches. These jumps are at points where $f(x)$ reaches an absolute maximum ("transition points") and at points where $g$ is discontinuous ("shocks"). The only rules that regulate these jumps are the

entropy condition $g\left(x_0^+\right) \le g\left(x_0^-\right)$ across a shock at $x_0$ and the respect of the periodicity condition (C.6). For the same value of $s_T$ there can be more than one entropy solution $g$.

**Table 3. Procedure used to calculate the front displacement speed, $s_T$, for the model problem considered in Section 4.3.**

Define $s_T^* = \sqrt{s_L^2 - V^2} + \max\left(-f\left(x\right)\right)$ and the function

$$F^{-1}\left(z\right) = \frac{Vz - s_L\sqrt{z^2 + \left(V^2 - s_L^2\right)}}{V^2 - s_L^2}$$

1. If $V > s_L$ then $s_T$ solves the nonlinear algebraic equation

$$\int_0^L F^{-1}\left(s_T + f\left(x\right)\right)dx = 0$$

2. If $V < s_L$

   a. if $\int_0^L F^{-1}\left(s_T^* + f\left(x\right)\right)dx < 0$ then $s_T = s_T^*$;

   b. else $s_T$ solves the same nonlinear algebraic equation as in case 1.

3. If $V = s_L$ the solution yields points where $g = \infty$ (i.e., a points where the flame is parallel to the *y*-axis) and is not well described by equation (2). The solution of this case can be obtained as a limit from above of case 1 or from below of case 2

Finally, as an example we show how the large time front speed $s_T$ for a flame propagating in a unidirectional periodic velocity field $u_y\left(x\right) = f\left(x\right)$, $u_x = 0$ can be obtained through a simple geometric reasoning, as mentioned in Section 2.4.2. For the flow field under consideration Eq. (C.5) becomes:

$$s_T = s_L\sqrt{1+g^2} - f(x) \tag{C.8}$$

When the flame front has reached a steady state, at points where $f(x)$ has an absolute minimum the flame slope $g$ is zero, by geometric necessity.

Then, Eq. (C.8) can be readily solved, obtaining

$$s_T = s_L + \max\left(-f(x)\right) \tag{C.9}$$

This result is independent of the particular details of the shear flow profile $f(x)$ and is a particular solution of case 2a in Table 3.

# REFERENCES


1. *International Energy Agency (IEA), World Energy Outlook 2013*, 2013.

2. Peters, N., *Multiscale combustion and turbulence.* Proceedings of the Combustion Institute, 2009. **32**(1): p. 1-25.

3. Lipatnikov, A.N., *Fundamentals of Premixed Turbulent Combustion*. 2012: CRC Press.

4. Lipatnikov, A.N. and J. Chomiak, *Molecular transport effects on turbulent flame propagation and structure.* Progress in Energy and Combustion Science, 2005. **31**(1): p. 1-73.

5. Lieuwen, T., V. Yang, and R. Yetter, *Synthesis gas combustion: fundamentals and applications*. 2009: CRC Press.

6. Lipatnikov, A.N. and J. Chomiak, *Turbulent flame speed and thickness: phenomenology, evaluation, and application in multi-dimensional simulations.* Progress in Energy and Combustion Science, 2002. **28**(1): p. 1-74.

7. Driscoll, J.F., *Turbulent premixed combustion: Flamelet structure and its effect on turbulent burning velocities.* Progress in Energy and Combustion Science, 2008. **34**(1): p. 91-134.

8. Wohl, K. and L. Shore, *Experiments with butane-air and methane-air flames.* Industrial & Engineering Chemistry, 1955. **47**(4): p. 828-834.

9. Venkateswaran, P., A. Marshall, J. Seitzman, and T. Lieuwen, *Pressure and fuel effects on turbulent consumption speeds of $H_2$/CO blends.* Proceedings of the Combustion Institute, 2013. **34**: p. 1527-1535.

10. Venkateswaran, P., A. Marshall, J. Seitzman, and T. Lieuwen, *Turbulent consumption speeds of high hydrogen content fuels from 1-20 atm.* Journal of Engineering for Gas Turbines and Power, 2014. **136**: p. 011504-1.

11. Venkateswaran, P., A. Marshall, D.H. Shin, D. Noble, J. Seitzman, and T. Lieuwen, *Measurements and analysis of turbulent consumption speeds of $H_2$/CO mixtures.* Combustion and Flame, 2011. **158**(8): p. 1602-1614.

12. Kido, H. and M. Nakahara, *A model of turbulent burning velocity taking the preferential diffusion effect into consideration.* JSME international journal. Ser. B, Fluids and thermal engineering, 1998. **41**(3): p. 666-673.

13. Kido, H., M. Nakahara, K. Nakashima, and J. Hashimoto, *Influence of local flame displacement velocity on turbulent burning velocity.* Proceedings of the Combustion Institute, 2002. **29**(2): p. 1855-1861.

14. Kido, H., K. Tanoue, M. Nakahara, and T. Inoue, *Experimental study of the turbulent combustion mechanism of non-stoichiometric mixtures.* JSAE Review, 1996. **17**(4): p. 361-367.

15. Nakahara, M. and H. Kido, *Study on the Turbulent Burning Velocity of Hydrogen Mixtures Including Hydrocarbon.* AIAA journal, 2008. **46**(7): p. 1569-1575.

16. Bell, J.B., R.K. Cheng, M.S. Day, and I.G. Shepherd, *Numerical simulation of Lewis number effects on lean premixed turbulent flames.* Proceedings of the Combustion Institute, 2007. **31**(1): p. 1309-1317.

17. Bédat, B. and R.K. Cheng, *Experimental study of premixed flames in intense isotropic turbulence.* Combustion and Flame, 1995. **100**(3): p. 485-494.

18. Chen, Y.C. and R.W. Bilger, *Experimental investigation of three-dimensional flame-front structure in premixed turbulent combustion: II. Lean hydrogen/air Bunsen flames.* Combustion and Flame, 2004. **138**(1–2): p. 155-174.

19. Williams, F.A., *Progress in knowledge of flamelet structure and extinction.* Progress in Energy and Combustion Science, 2000. **26**(4): p. 657-682.

20. Clavin, P., *Dynamic behavior of premixed flame fronts in laminar and turbulent flows.* Progress in Energy and Combustion Science, 1985. **11**(1): p. 1-59.

21. Law, C.K. and C.J. Sung, *Structure, aerodynamics, and geometry of premixed flamelets.* Progress in Energy and Combustion Science, 2000. **26**(4): p. 459-505.

22. de Goey, L., J. van Oijen, V. Kornilov, and J. ten Thije Boonkkamp, *Propagation, dynamics and control of laminar premixed flames.* Proceedings of the Combustion Institute, 2011. **33**(1): p. 863-886.

23. Yeung, P.K., S.S. Girimaji, and S.B. Pope, *Straining and scalar dissipation on material surfaces in turbulence: implications for flamelets.* Combustion and flame, 1990. **79**(3): p. 340-365.

24. Candel, S. and T. Poinsot, *Flame stretch and the balance equation for the flame area.* Combustion Science and Technology, 1990. **70**(1-3): p. 1-15.

25. Pope, S.B., *The evolution of surfaces in turbulence.* International journal of engineering science, 1988. **26**(5): p. 445-469.

26. Lieuwen, T.C., *Unsteady Combustor Physics*. 2012: Cambridge University Press.

27. Poinsot, T., D. Veynante, and S. Candel, *Quenching processes and premixed turbulent combustion diagrams.* Journal of Fluid Mechanics, 1991. **228**(561-606): p. 230.

28. Day, M.S., J.B. Bell, P.T. Bremer, V. Pascucci, V. Beckner, and M. Lijewski, *Turbulence effects on cellular burning structures in lean premixed hydrogen flames.* Combustion and Flame, 2009. **156**(5): p. 1035-1045.

29. Poinsot, T., T. Echekki, and M.G. Mungal, *A study of the laminar flame tip and implications for premixed turbulent combustion.* Combustion Science and Technology, 1992. **81**(1-3): p. 45-73.

30. Trouvé, A. and T. Poinsot, *The evolution equation for the flame surface density in turbulent premixed combustion.* Journal of Fluid Mechanics, 1994. **278**(-1): p. 1-31.

31. Echekki, T. and J.H. Chen, *Analysis of the contribution of curvature to premixed flame propagation.* Combustion and Flame, 1999. **118**(1–2): p. 308-311.

32. Sinibaldi, J.O., J.F. Driscoll, C.J. Mueller, J.M. Donbar, and C.D. Carter, *Propagation speeds and stretch rates measured along wrinkled flames to assess the theory of flame stretch.* Combustion and flame, 2003. **133**(3): p. 323-334.

33. Sinibaldi, J.O., C.J. Mueller, and J.F. Driscoll. *Local flame propagation speeds along wrinkled, unsteady, stretched premixed flames*. in *Symposium (International) on Combustion*. 1998. Elsevier.

34. Renou, B., A. Boukhalfa, D. Puechberty, and M. Trinité, *Local scalar flame properties of freely propagating premixed turbulent flames at various Lewis numbers.* Combustion and Flame, 2000. **123**(4): p. 507-521.

35. Renou, B., A. Boukhalfa, D. Puechberty, and M. Trinité, *Effects of stretch on the local structure of preely propagating premixed low-turbulent flames with various lewis numbers.* Symposium (International) on Combustion, 1998. **27**(1): p. 841-847.

36. Gran, I.R., T. Echekki, and J.H. Chen, *Negative flame speed in an unsteady 2-D premixed flame: A computational study.* Symposium (International) on Combustion, 1996. **26**(1): p. 323-329.

37. Groot, G.R.A. and L.P.H. De Goey, *A computational study on propagating spherical and cylindrical premixed flames.* Proceedings of the Combustion Institute, 2002. **29**(2): p. 1445-1451.

38. Sohrab, S.H., Z.Y. Ye, and C.K. Law, *An experimental investigation on flame interaction and the existence of negative flame speeds.* Symposium (International) on Combustion, 1985. **20**(1): p. 1957-1965.

39. Bechtold, J. and M. Matalon, *The dependence of the Markstein length on stoichiometry.* Combustion and flame, 2001. **127**(1): p. 1906-1913.

40. Mosbacher, D.M., J.A. Wehrmeyer, R.W. Pitz, C.J. Sung, and J.L. Byrd, *Experimental and numerical investigation of premixed tubular flames.* Proceedings of the Combustion Institute, 2002. **29**(2): p. 1479-1486.

41. Chen, Z., M.P. Burke, and Y. Ju, *Effects of Lewis number and ignition energy on the determination of laminar flame speed using propagating spherical flames.* Proceedings of the Combustion Institute, 2009. **32**(1): p. 1253-1260.

42. Lipatnikov, A.N. and J. Chomiak, *Lewis number effects in premixed turbulent combustion and highly perturbed laminar flames.* Combustion Science and Technology, 1998. **137**(1-6): p. 277-298.

43. Sun, C.J. and C.K. Law, *On the nonlinear response of stretched premixed flames.* Combustion and Flame, 2000. **121**(1–2): p. 236-248.

44. Mishra, D., P. Paul, and H. Mukunda, *Stretch effects extracted from propagating spherical premixed flames with detailed chemistry.* Combustion and flame, 1994. **99**(2): p. 379-386.

45. Mishra, D., P. Paul, and H. Mukunda, *Stretch effects extracted from inwardly and outwardly propagating spherical premixed flames.* Combustion and flame, 1994. **97**(1): p. 35-47.

46. Sivashinsky, G., *Nonlinear analysis of hydrodynamic instability in laminar flames—I. Derivation of basic equations.* Acta Astronautica, 1977. **4**(11): p. 1177-1206.

47. Class, A.G., B. Matkowsky, and A. Klimenko, *A unified model of flames as gasdynamic discontinuities.* Journal of Fluid Mechanics, 2003. **491**(1): p. 11-49.

48. Chen, Z. and Y. Ju, *Theoretical analysis of the evolution from ignition kernel to flame ball and planar flame.* Combustion Theory and Modelling, 2007. **11**(3): p. 427-453.

49. Bradley, D., P. Gaskell, and X. Gu, *Burning velocities, Markstein lengths, and flame quenching for spherical methane-air flames: a computational study.* Combustion and Flame, 1996. **104**(1): p. 176-198.

50. Clavin, P. and J.C. Graña-Otero, *Curved and stretched flames: the two Markstein numbers.* Journal of Fluid Mechanics, 2011. **686**: p. 187.

51. Groot, G., J. Van Oijen, L. De Goey, K. Seshadri, and N. Peters, *The effects of strain and curvature on the mass burning rate of premixed laminar flames.* Combustion Theory and Modelling, 2002. **6**: p. 675-695.

52. Peiyong, W., H. Shengteng, W. Joseph, and P. Robert, *Stretch and Curvature Effects on Flames*, in *42nd AIAA Aerospace Sciences Meeting and Exhibit*. 2004, American Institute of Aeronautics and Astronautics.

53. Wang, P., J.A. Wehrmeyer, and R.W. Pitz, *Stretch rate of tubular premixed flames.* Combustion and Flame, 2006. **145**(1-2): p. 401-414.

54. Clavin, P. and G. Joulin, *High-frequency response of premixed flames to weak stretch and curvature: a variable-density analysis.* Combustion Theory and Modelling, 1997. **1**(4): p. 429-446.

55. Joulin, G., *On the response of premixed flames to time-dependent stretch and curvature.* Combustion Science and Technology, 1994. **97**(1-3): p. 219-229.

56. Im, H.G. and J.H. Chen, *Effects of flow transients on the burning velocity of laminar hydrogen/air premixed flames.* Proceedings of the Combustion Institute, 2000. **28**(2): p. 1833-1840.

57. Peters, N., *The turbulent burning velocity for large-scale and small-scale turbulence.* Journal of Fluid Mechanics, 1999. **384**(1): p. 107-132.

58. Hawkes, E.R. and J.H. Chen, *Evaluation of models for flame stretch due to curvature in the thin reaction zones regime.* Proceedings of the Combustion Institute, 2005. **30**(1): p. 647-655.

59. Rutland, C. and A. Trouvé, *Direct simulations of premixed turbulent flames with nonunity Lewis numbers.* Combustion and Flame, 1993. **94**(1-2): p. 41-57.

60. Poinsot, T., S. Candel, and A. Trouvé, *Applications of direct numerical simulation to premixed turbulent combustion.* Progress in Energy and Combustion Science, 1995. **21**(6): p. 531-576.

61. Kuznetsov, V.R. and V.A. Sabel'nikov, *Turbulence and combustion*. 1990, New York: Hemisphere Publishing.

62. Kadowaki, S. and T. Hasegawa, *Numerical simulation of dynamics of premixed flames: flame instability and vortex–flame interaction.* Progress in Energy and Combustion Science, 2005. **31**(3): p. 193-241.

63. Roberts, W.L., J.F. Driscoll, M.C. Drake, and L.P. Goss, *Images of the quenching of a flame by a vortex—To quantify regimes of turbulent combustion.* Combustion and Flame, 1993. **94**(1–2): p. 58-69.

64. Ishizuka, S., *Flame propagation along a vortex axis.* Progress in Energy and Combustion Science, 2002. **28**(6): p. 477-542.

65. Buckmaster, J., *The structure and stability of laminar flames.* Annual review of fluid mechanics, 1993. **25**(1): p. 21-53.

66. Law, C.K., *Combustion physics*. 2006: Cambridge Univ Pr.

67. Dixon-Lewis, G. *Structure of laminar flames*. in *Symposium (International) on Combustion*. 1991. Elsevier.

68. Borghi, R., *On the structure and morphology of turbulent premixed flames*, in *Recent advances in the Aerospace Sciences*. 1985, Springer. p. 117-138.

69. Turns, S.R., *An introduction to combustion*. 2nd ed. 2000, New York: Mc Graw Hill.

70. Dunn, M.J., A.R. Masri, R.W. Bilger, and R.S. Barlow, *Finite rate chemistry effects in highly sheared turbulent premixed flames.* Flow, turbulence and combustion, 2010. **85**(3-4): p. 621-648.

71. Aspden, A.J., M.S. Day, and J.B. Bell, *Turbulence–flame interactions in lean premixed hydrogen: transition to the distributed burning regime.* Journal of Fluid Mechanics, 2011. **1**(1): p. 1-34.

72. Poludnenko, A.Y. and E.S. Oran, *The interaction of high-speed turbulence with flames: Global properties and internal flame structure.* Combustion and Flame, 2010. **157**(5): p. 995-1011.

73. Peters, N. *Laminar flamelet concepts in turbulent combustion*. in *Symposium (International) on Combustion*. 1988. Elsevier.

74. Bilger, R.W., S.B. Pope, K.N.C. Bray, and J.F. Driscoll, *Paradigms in turbulent combustion research.* Proceedings of the Combustion Institute, 2005. **30**(1): p. 21-42.

75. Damköhler, G., *Der einfluß der turbulenz auf die flammengeschwindigkeit in gasgemischen.* Zeitschrift für Elektrochemie und angewandte physikalische Chemie, 1940. **46**(11): p. 601-626.

76. Brutscher, T., N. Zarzalis, and H. Bockhorn, *An experimentally based approach for the space-averaged laminar burning velocity used for modeling premixed turbulent combustion.* Proceedings of the Combustion Institute, 2002. **29**(2): p. 1825-1832.

77. Bradley, D., M. Lawes, K. Liu, and M.S. Mansour, *Measurements and correlations of turbulent burning velocities over wide ranges of fuels and elevated pressures.* Proceedings of the Combustion Institute, 2013. **34**(1): p. 1519-1526.

78. Daniele, S., J. Mantzaras, P. Jansohn, A. Denisov, and K. Boulouchos, *Flame front/turbulence interaction for syngas fuels in the thin reaction zones regime: turbulent and stretched laminar flame speeds at elevated pressures and temperatures.* Journal of Fluid Mechanics, 2013. **724**: p. 36-68.

79. Veynante, D. and L. Vervisch, *Turbulent combustion modeling.* Progress in Energy and Combustion Science, 2002. **28**(3): p. 193-266.

80. Kolla, H. and N. Swaminathan, *Strained flamelets for turbulent premixed flames, I: Formulation and planar flame results.* Combustion and Flame, 2010. **157**(5): p. 943-954.

81. Kolla, H. and N. Swaminathan, *Strained flamelets for turbulent premixed flames II: Laboratory flame results.* Combustion and Flame, 2010. **157**(7): p. 1274-1289.

82. Knudsen, E., H. Kolla, E.R. Hawkes, and H. Pitsch, *LES of a premixed jet flame DNS using a strained flamelet model.* Combustion and Flame, 2013. **160**(12): p. 2911-2927.

83. Subramanian, V., P. Domingo, and L. Vervisch, *Large eddy simulation of forced ignition of an annular bluff-body burner.* Combustion and Flame, 2010. **157**(3): p. 579-601.

84. Peters, N., *Turbulent combustion*. 2000: Cambridge university press.

85. Muppala, S.P.R., N.K. Aluri, F. Dinkelacker, and A. Leipertz, *Development of an algebraic reaction rate closure for the numerical calculation of turbulent premixed methane, ethylene, and propane/air flames for pressures up to 1.0 MPa.* Combustion and Flame, 2005. **140**(4): p. 257-266.

86. Bray, K.N.C. and R.S. Cant, *Some applications of Kolmogorov's turbulence research in the field of combustion.* Proceedings of the Royal Society of London. Series A: Mathematical and Physical Sciences, 1991. **434**(1890): p. 217-240.

87. Swaminathan, N. and K.N.C. Bray, *Turbulent premixed flames*. 2011: Cambridge University Press.

88. Swaminathan, N. and R.W. Bilger, *Analyses of conditional moment closure for turbulent premixed flames.* Combustion Theory and Modelling, 2001. **5**(2): p. 241-260.

89. Kemenov, K.A. and S.B. Pope, *Molecular diffusion effects in LES of a piloted methane–air flame.* Combustion and Flame, 2011. **158**(2): p. 240-254.

90. Poludnenko, A.Y. and E.S. Oran, *The interaction of high-speed turbulence with flames: Turbulent flame speed.* Combustion and Flame, 2011. **158**(2): p. 301-326.

91. Bell, J.B., M.S. Day, J.F. Grcar, M.J. Lijewski, J.F. Driscoll, and S.A. Filatyev, *Numerical simulation of a laboratory-scale turbulent slot flame.* Proceedings of the Combustion Institute, 2007. **31**(1): p. 1299-1307.

92. Day, M.S., S. Tachibana, J.B. Bell, M. Lijewski, V. Beckner, and R.K. Cheng, *A combined computational and experimental characterization of lean premixed*

*turbulent low swirl laboratory flames: I. Methane flames.* Combustion and Flame, 2011.

93. Chen, J.B. and H.G. Im, *Stretch effects on the burning velocity of turbulent premixed hydrogen/air flames.* Proceedings of the combustion institute, 2000. **28**(1): p. 211-218.

94. Peters, N., P. Terhoeven, J.H. Chen, and T. Echekki. *Statistics of flame displacement speeds from computations of 2-D unsteady methane-air flames*. in *Symposium (International) on Combustion*. 1998. Elsevier.

95. Day, M.S., I.G. Shepherd, J.B. Bell, J.F. Grcar, and M.J. Lijewski, *Displacement speeds in turbulent premixed flame simulations*, 2008.

96. Chakraborty, N. and R.S. Cant, *Effects of Lewis number on flame surface density transport in turbulent premixed combustion.* Combustion and Flame, 2011.

97. Baum, M., T. Poinsot, D.C. Haworth, and N. Darabiha, *Direct numerical simulation of $H_2/O_2/N_2$ flames with complex chemistry in two-dimensional turbulent flows.* Journal of Fluid Mechanics, 1994. **281**: p. 1-32.

98. Hawkes, E.R. and J.H. Chen, *Direct numerical simulation of hydrogen-enriched lean premixed methane–air flames.* Combustion and Flame, 2004. **138**(3): p. 242-258.

99. Hawkes, E.R. and J.H. Chen, *Comparison of direct numerical simulation of lean premixed methane–air flames with strained laminar flame calculations.* Combustion and Flame, 2006. **144**(1): p. 112-125.

100. Sankaran, R., E.R. Hawkes, J.H. Chen, T. Lu, and C.K. Law, *Structure of a spatially developing turbulent lean methane–air Bunsen flame.* Proceedings of the Combustion Institute, 2007. **31**(1): p. 1291-1298.

101. Bradley, D., P. Gaskell, A. Sedaghat, and X. Gu, *Generation of PDFS for flame curvature and for flame stretch rate in premixed turbulent combustion.* Combustion and flame, 2003. **135**(4): p. 503-523.

102. Haworth, D.C. and T. Poinsot, *Numerical simulations of Lewis number effects in turbulent premixed flames.* Journal of Fluid Mechanics, 1992. **244**(1): p. 405-436.

103. Chakraborty, N. and R.S. Cant, *Effects of strain rate and curvature on surface density function transport in turbulent premixed flames in the thin reaction zones regime.* Physics of Fluids, 2005. **17**: p. 065108.

104. Chakraborty, N. and R.S. Cant, *Unsteady effects of strain rate and curvature on turbulent premixed flames in an inflow–outflow configuration.* Combustion and Flame, 2004. **137**(1–2): p. 129-147.

105. Chakraborty, N. and R.S. Cant, *Influence of Lewis number on curvature effects in turbulent premixed flame propagation in the thin reaction zones regime.* Physics of Fluids, 2005. **17**: p. 105105.

106. Chakraborty, N. and R.S. Cant, *Influence of Lewis number on strain rate effects in turbulent premixed flame propagation.* International Journal of Heat and Mass Transfer, 2006. **49**(13–14): p. 2158-2172.

107. Kim, S.H. and H. Pitsch, *Scalar gradient and small-scale structure in turbulent premixed combustion.* Physics of Fluids, 2007. **19**(11): p. 115104.

108. Chakraborty, N., M. Klein, and N. Swaminathan, *Effects of Lewis number on the reactive scalar gradient alignment with local strain rate in turbulent premixed flames.* Proceedings of the Combustion Institute, 2009. **32**(1): p. 1409-1417.

109. Cant, R.S., *Direct numerical simulation of premixed turbulent flames.* Philosophical Transactions of the Royal Society of London. Series A: Mathematical, Physical and Engineering Sciences, 1999. **357**(1764): p. 3583-3604.

110. Girimaji, S.S. and S.B. Pope, *Propagating surfaces in isotropic turbulence.* Journal of Fluid Mechanics, 1992. **234**: p. 247-277.

111. Ashurst, W.T., N. Peters, and M.D. Smooke, *Numerical simulation of turbulent flame structure with non-unity Lewis number.* Combustion science and technology, 1987. **53**(4-6): p. 339-375.

112. Swaminathan, N. and R.W. Bilger, *Scalar dissipation, diffusion and dilatation in turbulent H2-air premixed flames with complex chemistry.* Combustion Theory and Modelling, 2001. **5**(3): p. 429-446.

113. Kee, R.J., J. Warnatz, and J.A. Miller, *Fortran computer-code package for the evaluation of gas-phase viscosities, conductivities, and diffusion coefficients.* Sandia report SAND83-8209, 1983.

114. Echekki, T. and J.H. Chen, *Unsteady strain rate and curvature effects in turbulent premixed methane-air flames.* Combustion and Flame, 1996. **106**(1): p. 184-202.

115. Chen, J.H., T. Echekki, and W. Kollmann, *The mechanism of two-dimensional pocket formation in lean premixed methane-air flames with implications to turbulent combustion.* Combustion and Flame, 1999. **116**(1–2): p. 15-48.

116. Kollmann, W. and J.H. Chen, *Pocket formation and the flame surface density equation.* Symposium (International) on Combustion, 1998. **27**(1): p. 927-934.

117. Chen, J.H. and H.G. Im. *Correlation of flame speed with stretch in turbulent premixed methane/air flames*. in *Symposium (International) on Combustion*. 1998. Elsevier.

118. Im, H.G. and J.H. Chen, *Preferential diffusion effects on the burning rate of interacting turbulent premixed hydrogen-air flames.* Combustion and flame, 2002. **131**(3): p. 246-258.

119. Chakraborty, N., E.R. Hawkes, J.H. Chen, and R.S. Cant, *The effects of strain rate and curvature on surface density function transport in turbulent premixed methane–air and hydrogen–air flames: A comparative study.* Combustion and Flame, 2008. **154**(1): p. 259-280.

120. de Charentenay, J. and A. Ern, *Multicomponent transport impact on turbulent premixed H 2/O 2 flames.* Combustion Theory and Modelling, 2002. **6**(3): p. 439-462.

121. Tanahashi, M., M. Fujimura, and T. Miyauchi, *Coherent fine-scale eddies in turbulent premixed flames.* Proceedings of the Combustion Institute, 2000. **28**(1): p. 529-535.

122. Tanahashi, M., Y. Nada, Y. Ito, and T. Miauchi, *Local flame structure in the well-stirred reactor regime.* Proceedings of the Combustion Institute, 2002. **29**(2): p. 2041-2049.

123. Shim, Y.S., S. Tanaka, M. Tanahashi, and T. Miyauchi, *Local structure and fractal characteristics of H2–air turbulent premixed flame.* Proceedings of the Combustion Institute, 2011. **33**(1): p. 1455-1462.

124. Shim, Y.S., N. Fukushima, M. Shimura, Y. Nada, M. Tanahashi, and T. Miyauchi, *Radical fingering in turbulent premixed flame classified into thin reaction zones.* Proceedings of the Combustion Institute, 2013. **34**(1): p. 1383-1391.

125. Chakraborty, N. and R.S. Cant, *Physical insight and modelling for Lewis number effects on turbulent heat and mass transport in turbulent premixed flames.* Numerical Heat Transfer, Part A: Applications, 2009. **55**(8): p. 762-779.

126. Chakraborty, N. and R.S. Cant, *Effects of Lewis number on turbulent scalar transport and its modelling in turbulent premixed flames.* Combustion and Flame, 2009. **156**(7): p. 1427-1444.

127. Katragadda, M., S.P. Malkeson, and N. Chakraborty, *Modelling of the tangential strain rate term of the Flame Surface Density transport equation in the context of Reynolds Averaged Navier–Stokes simulation.* Proceedings of the Combustion Institute, 2011. **33**(1): p. 1429-1437.

128. Han, I. and K.Y. Huh, *Roles of displacement speed on evolution of flame surface density for different turbulent intensities and Lewis numbers in turbulent premixed combustion.* Combustion and Flame, 2008. **152**(1-2): p. 194-205.

129. Day, M.S., X. Gao, and J.B. Bell, *Properties of lean turbulent methane-air flames with significant hydrogen addition.* Proceedings of the Combustion Institute, 2011. **33**(1): p. 1601-1608.

130. Aspden, A.J., M.S. Day, and J.B. Bell, *Lewis number effects in distributed flames.* Proceedings of the Combustion Institute, 2011. **33**(1): p. 1473-1480.

131. Aspden, A.J., M.S. Day, and J.B. Bell, *Characterization of low Lewis number flames.* Proceedings of the Combustion Institute, 2011. **33**(1): p. 1463-1471.

132. Chatakonda, O., E.R. Hawkes, A.J. Aspden, A.R. Kerstein, H. Kolla, and J.H. Chen, *On the fractal characteristics of low Damköhler number flames.* Combustion and Flame, 2013. **160**(11): p. 2422-2433.

133. Hawkes, E.R., O. Chatakonda, H. Kolla, A.R. Kerstein, and J.H. Chen, *A petascale direct numerical simulation study of the modelling of flame wrinkling for large-eddy simulations in intense turbulence.* Combustion and Flame, 2012. **159**(8): p. 2690-2703.

134. Zeldovich, I., G.I. Barenblatt, V. Librovich, and G. Makhviladze, *Mathematical Theory of Combustion and Explosions*. 1985, New York: Consultants Bureau (Plenum Publishing Corporation).

135. Aluri, N.K., S.P.R. Muppala, and F. Dinkelacker, *Substantiating a fractal-based algebraic reaction closure of premixed turbulent combustion for high pressure and the Lewis number effects.* Combustion and Flame, 2006. **145**(4): p. 663-674.

136. Karpov, V.P., A.N. Lipatnikov, and V.L. Zimont, *Flame curvature as a deteminant of preferential diffusion effects in premixed turbulent combustion*, in *Advances in combustion science: in honor of YA. B. Zel'dovich*, W.A. Sirignano, A.G. Merzhanov, and L. De Luca, Editors. 1997, AIAA.

137. Karpov, V.P., A.N. Lipatnikov, and V.L. Zimont, *A test of an engineering model of premixed turbulent combustion.* Symposium (International) on Combustion, 1996. **26**(1): p. 249-257.

138. Muppala, S.P.R., M. Nakahara, N.K. Aluri, H. Kido, J.X. Wen, and M.V. Papalexandris, *Experimental and analytical investigation of the turbulent burning velocity of two-component fuel mixtures of hydrogen, methane and propane.* International Journal of Hydrogen Energy, 2009. **34**(22): p. 9258-9265.

139. Dinkelacker, F., B. Manickam, and S.P.R. Muppala, *Modelling and simulation of lean premixed turbulent methane/hydrogen/air flames with an effective Lewis number approach.* Combustion and Flame, 2011. **158**(9): p. 1742-1749.

140. Yuen, F.T. and Ö.L. Gülder, *Turbulent premixed flame front dynamics and implications for limits of flamelet hypothesis.* Proceedings of the Combustion Institute, 2012. **34**: p. 1393–1400.

141. Ebert, U. and W. van Saarloos, *Front propagation into unstable states: universal algebraic convergence towards uniformly translating pulled fronts.* Physica D: Nonlinear Phenomena, 2000. **146**(1): p. 1-99.

142. Duclos, J.M., D. Veynante, and T. Poinsot, *A comparison of flamelet models for premixed turbulent combustion.* Combustion and Flame, 1993. **95**(1-2): p. 101-117.

143. Marshall, A., P. Venkateswaran, J. Seitzman, and T. Lieuwen, *Measurements of leading point conditioned statistics of high hydrogen content fuels*, in *8th U. S. National Combustion Meeting*2013: Park City, UT.

144. Hemchandra, S. and T. Lieuwen, *Local consumption speed of turbulent premixed flames–An analysis of "memory effects"*. Combustion and Flame, 2010. **157**(5): p. 955-965.

145. Dunstan, T.D., N. Swaminathan, and K.N.C. Bray, *Influence of flame geometry on turbulent premixed flame propagation: a DNS investigation.* Journal of Fluid Mechanics, 2012. **709**: p. 191-222.

146. Bowman, C.T., R.K. Hanson, D.F. Davidson, W.C.J. Gardiner, V. Lissianski, G.P. Smith, D.M. Golden, M. Frenklach, and M. Goldenberg. *GRI-Mech 2.11*. Available from: http://www.me.berkeley.edu/gri_mech/.

147. *CHEMKIN*. Available from: http://www.reactiondesign.com.

148. *COMSOL*. Available from: http://www.comsol.com/.

149. Amato, A., M.S. Day, J.B. Bell, R.K. Cheng, and T. Lieuwen. *Leading Edge Statistics of Turbulent, Lean, $H_2$/Air Flames*. in *35th International Symposium on Combustion*. 2014. San Francisco, CA.

150. Pope, S.B., *Turbulent flows*. 2000: Cambridge university press.

151. Aldredge, R.C., *The propagation of wrinkled premixed flames in spatially periodic shear flow.* Combustion and Flame, 1992. **90**(2): p. 121-133.

152. Yu, K.M., C.J. Sung, and C.K. Law, *Some aspects of the freely propagating premixed flame in a spatially periodic flow field.* Combustion and Flame, 1994. **97**(3-4): p. 375-383.

153. Sung, C.J., C.J. Sun, and C.K. Law, *Analytic description of the evolution of two-dimensional flame surfaces.* Combustion and Flame, 1996. **107**(1-2): p. 114-124.

154. Ashurst, W.T., G.I. Sivashinsky, and V. Yakhot, *Flame front propagation in nonsteady hydrodynamic fields.* Combustion Science and Technology, 1988. **62**(4): p. 273-284.

155. Ashurst, W.T. and G.I. Sivashinsky, *SHORT COMMUNICATION On Flame Propagation Through Periodic Flow Fields.* Combustion Science and Technology, 1991. **80**(1): p. 159-164.

156. Ashurst, W.T., *Flow-frequency effect upon Huygens front propagation.* Combustion Theory and Modelling, 2000. **4**(2): p. 99-105.

157. Kortsarts, Y., L. Kagan, and G. Sivashinsky, *Flame extinction by spatially periodic shear flows.* Combustion Theory and Modelling, 2002. **6**(2): p. 189-195.

158. Bourlioux, A., *Semi-analytical validation of a dynamic large-eddy simulation procedure for turbulent premixed flames via the G-equation.* Combustion Theory and Modelling, 2000. **4**(4): p. 363-389.

159. Khouider, B., A. Bourlioux, and A.J. Majda, *Parametrizing the burning speed enhancement by small-scale periodic flows: I. Unsteady shears, flame residence time and bending.* Combustion Theory and Modelling, 2001. **5**(3): p. 295-318.

160. Embid, P.F., A.J. Majda, and P.E. Souganidis, *Comparison of turbulent flame speeds from complete averaging and the G-equation.* Physics of Fluids, 1995. **7**(8): p. 2052-2060.

161. Williams, F.A., *Turbulent combustion*, in *The Mathematics of Combustion*, J.D. Buckmaster, Editor. 1985, SIAM: Philadelphia. p. 97-131.

162. Fleifil, M., A.M. Annaswamy, Z.A. Ghoneim, and A.F. Ghoniem, *Response of a laminar premixed flame to flow oscillations: A kinematic model and thermoacoustic instability results.* Combustion and Flame, 1996. **106**(4): p. 487-510.

163. Aldredge, R.C., *The speed of isothermal-front propagation in isotropic, weakly turbulent flows.* Combustion Science and Technology, 2006. **178**(7): p. 1201-1215.

164. Huang, Y. and V. Yang, *Dynamics and stability of lean-premixed swirl-stabilized combustion.* Progress in Energy and Combustion Science, 2009. **35**(4): p. 293-364.

165. Pitsch, H. and L. Duchamp de Lageneste, *Large-eddy simulation of premixed turbulent combustion using a level-set approach.* Proceedings of the Combustion Institute, 2002. **29**(2): p. 2001-2008.

166. Evans, L.C., *Partial differential equations*. 1998: American Mathematical Society.

167. Wiggins, S., *Introduction to applied nonlinear dynamical systems and chaos*. 2nd ed. 2003: Springer.

168. Fleming, W.H. and H.M. Soner, *Controlled Markov processes and viscosity solutions*. Vol. 25. 2006: Springer New York.

169. E, W., *Aubry–Mather theory and periodic solutions of the forced Burgers equation.* Comm. Pure Appl. Math, 1999. **52**(7): p. 811-828.

170. Fathi, A. and A. Siconolfi, *PDE aspects of Aubry-Mather theory for quasiconvex Hamiltonians.* Calculus of Variations and Partial Differential Equations, 2005. **22**(2): p. 185-228.

171. Davini, A. and A. Siconolfi, *A Generalized Dynamical Approach to the Large Time Behavior of Solutions of Hamilton--Jacobi Equations.* SIAM journal on mathematical analysis, 2006. **38**(2): p. 478-502.

172. Evans, L.C. and D. Gomes, *Effective Hamiltonians and averaging for Hamiltonian dynamics I.* Archive for rational mechanics and analysis, 2001. **157**(1): p. 1-33.

173. Jauslin, H.R., H.O. Kreiss, and J. Moser. *On the forced Burgers equation with periodic boundary conditions*. in *Proceedings of symposia in pure Mathematics*. 1999. American Mathematical Society.

174. Liu, Y.Y., J. Xin, and Y. Yu, *Periodic homogenization of G-equations and viscosity effects.* Nonlinearity, 2010. **23**(10): p. 2351.

175. Xin, J. and Y. Yu, *Analysis and Comparison of Large Time Front Speeds in Turbulent Combustion Models.* arXiv preprint, arXiv:1105.5607 [math.AP], 2011.

176. Pocheau, A. and F. Harambat, *Front propagation in a laminar cellular flow: Shapes, velocities, and least time criterion.* Physical Review E, 2008. **77**(3): p. 036304.

177. Xin, J. and Y. Yu, *Sharp asymptotic growth laws of turbulent flame speeds in cellular flows by inviscid Hamilton–Jacobi models.* Annales de l'Institut Henri Poincare (C) Non Linear Analysis, 2013.

178. Bec, J. and K. Khanin, *Burgers turbulence.* Physics Reports, 2007. **447**(1): p. 1-66.

179. Fedotov, S., *G-equation, stochastic control theory and relativistic mechanics of a particle moving in a random field.* Combustion Theory and Modelling, 1997. **1**(1): p. 1-6.

180. Mayo, J.R. and A.R. Kerstein, *Scaling of Huygens-front speedup in weakly random media*. Physics Letters A, 2007. **372**(1): p. 5-11.

181. Embid, P.F., A.J. Majda, and P.E. Souganidis, *Effective geometric front dynamics for premixed turbulent combustion with separated velocity scales.* Combustion Science and Technology, 1994. **103**(1): p. 85-115.

182. Strogatz, S., *Nonlinear dynamics and chaos: with applications to physics, biology, chemistry and engineering*. 2001: Westview Press (Perseus Books Publishing).

183. Nishida, T. and K. Soga, *Difference approximation to Aubry-Mather sets of the forced Burgers equation.* Nonlinearity, 2012. **25**(9): p. 2401-2422.

184. Kerstein, A.R., W.T. Ashurst, and F.A. Williams, *Field equation for interface propagation in an unsteady homogeneous flow field.* Physical Review A, 1988. **37**(7): p. 2728.

185. Kerstein, A.R. and W.T. Ashurst, *Passage rates of propagating interfaces in randomly advected media and heterogeneous media.* Physical Review E, 1994. **50**(2): p. 1100.

186. Fleming, W.H., *The Cauchy problem for a nonlinear first order partial differential equation.* J. Differential Equations, 1969. **5**: p. 515-530.

187. Bessi, U., *Aubry-mather theory and Hamilton-Jacobi equations.* Communications in mathematical physics, 2003. **235**(3): p. 495-511.

188. Anantharaman, N., R. Iturriaga, P. Padilla, H. Sánchez-Morgado, J. Banasiak, M. Mokhtar-Kharroubi, N. Carlsson, G. Högnäs, J. Chazottes, and E. Ugalde, *Physical solutions of the Hamilton-Jacobi equation.* Discrete and Continuous Dynamical Systems-Series B, 2005. **5**(3).

189. Liu, Y.Y., J. Xin, and Y. Yu, *Asymptotics for turbulent flame speeds of the viscous G-equation enhanced by cellular and shear flows.* Archive for Rational Mechanics and Analysis, 2011. **202**(2): p. 461-492.

190. Jiang, G.S. and D. Peng, *Weighted ENO Schemes for Hamilton-Jacobi Equations.* SIAM Journal on Scientific computing, 2000. **21**(6): p. 2126-2143.

191. Gottlieb, S. and C.W. Shu, *Total variation diminishing Runge-Kutta schemes.* Math. Comput., 1998. **67**(221): p. 73-85.

192. Gilbarg, D. and N. Trudinger, *Elliptic PDE of second order*. 2nd ed. 1983: Springer-Verlag, New York.

193. Amato, A., *Leading Points Concepts in Turbulent Premixed Combustion Modeling*, 2014, Georgia Institute of Technology.

194. Cardaliaguet, P., J. Nolen, and P.E. Souganidis, *Homogenization and Enhancement for the G-Equation.* Archive for Rational Mechanics and Analysis, 2011. **199**(2): p. 527-561.

195. Xin, J. and Y. Yu, *Periodic homogenization of the inviscid G-equation for incompressible flows.* Communications in Mathematical Sciences, 2010. **8**(4): p. 1067-1078.

196. Cardaliaguet, P. and P.E. Souganidis, *Homogenization and enhancement of the G-equation in random environments.* arXiv preprint arXiv:1110.1760, 2011.

197. Lutz, A.E., R.J. Kee, J.F. Grcar, and F.M. Rupley, *OPPDIF: A Fortran program for computing opposed-flow diffusion flames.* Sandia National Laboratories Report SAND96-8243, 1997.

198. Hindmarsh, A.C., P.N. Brown, K.E. Grant, S.L. Lee, R. Serban, D.E. Shumaker, and C.S. Woodward, *SUNDIALS: Suite of nonlinear and differential/algebraic equation solvers.* ACM Transactions on Mathematical Software (TOMS), 2005. **31**(3): p. 363-396.

199. Davis, S.G., A.V. Joshi, H. Wang, and F. Egolfopoulos, *An optimized kinetic model of $H_2$/CO combustion.* Proceedings of the Combustion Institute, 2005. **30**(1): p. 1283-1292.

200. Kee, R.J., J.F. Grcar, M.D. Smooke, and J.A. Miller, *PREMIX: a Fortran program for modeling steady laminar one-dimensional premixed flames.* Sandia report SAND85-8240, 1985.

201. Amato, A., M.S. Day, R.K. Cheng, J.B. Bell, and T. Lieuwen, *Leading Point Statistics of a Turbulent, Lean, $H_2$-Air Flame,* in *Spring Technical Meeting of the Central States Section of the Combustion Institute*2012: Dayton, Ohio, USA.

202. Kee, R.J., M.E. Coltrin, and P. Glarborg, *Chemically reacting flow: theory and practice*. 2005: John Wiley & Sons.

203. Yokomori, T., Z. Chen, and Y. Ju. *Studies on the flame curvature effect on burning velocity*. in *44th AIAA Aerospace Sciences Meeting and Exhibit*. 2006.

204. Xin, J., *An Introduction to Fronts in Random Media*. Surveys and Tutorials in the Applied Mathematical Sciences (5). 2009: Springer.

205. Phillips, O.M., *The entrainment interface.* Journal of Fluid Mechanics, 1972. **51**(1): p. 97-118.